COPERNICUS SPACE COMPONENT SENTINEL OPTICAL IMAGING

MISSION PERFORMANCE CLUSTER SERVICE

Data Quality Report

Sentinel-3 OLCI

May 2022

OPT-MPC

Copernicus Sentinel

Optical Mission Performance Cluster

Ref.: OMPC.ACR.DQR.03.05-2022
Issue: 1.1
Date: 17/06/2022
Contract: 4000136252/21/I-BG

Customer:	ESA	Document Ref.:	OMPC.ACR.DQR.03.05-2022
Contract No.:	4000136252/21/I-BG	Date:	17/06/2022
		Issue:	1.1

Project:	COPERNICUS SPACE COMPONENT SENTINEL OPTICAL IMAGING MISSION PERFORMANCE CLUSTER SERVICE		
Title:	Data Quality Report - OLCI		
Author(s):	OLCI ESL team		
Approved by:	L. Bourg, OPT-MPC OLCI ESL Coordinator S. Clerc, OPT-MPC Optical ESL Coordinator	Authorized by	C. Hénocq, OPT-MPC S3 Technical Manager
Distribution:	ESA, EUMETSAT, published in Sentinel Online		
Accepted by ESA	S. Dransfeld, ESA TO		
Filename	OMPC.ACR.DQR.03.05-2022 - i1r1 - OLCI DQR May 2022.docx		

Changes Log

Version	Date	Changes
1.0	09/06/2022	First version
1.1	17/06/2022	Minor corrections spotted by ESA

List of Changes

Version	Section	Answers to RID	Changes

Table of content

List of Figures

List of Tables

1 Processing Baseline Version

1.1 Sentinel3-A

IPF	IPF / Processing Baseline version	Date of deployment
OL1	06.12 / OL__L1_.002.22.00	20/01/2022 11:08 UTC
OL2 LAND	06.16 / OL__L2L.002.10.00	26/01/2021 10:15 UTC
SY2	06.22 / SYN_L2_.002.15.00	27/01/2022 10:15 UTC
SY2_VGS	06.10 / SYN_L2V.002.07.00	27/01/2022 10:15 UTC
SY2_AOD	01.06 / AOD_NTC.002.06.00	27/01/2022 10:15 UTC

1.2 Sentinel3-B

IPF	IPF / Processing Baseline version	Date of deployment
OL1	06.12 / OL__L1_.002.22.00	20/01/2022 11:08 UTC
OL2 Land	06.16 / OL__L2L.002.10.00	26/01/2021 10:15 UTC
SY2	06.22 / SYN_L2_.002.15.00	27/01/2022 10:15 UTC
SY2_VGS	06.10 / SYN_L2V.002.07.00	27/01/2022 10:15 UTC
SY2_AOD	01.06 / AOD_NTC.002.06.00	27/01/2022 10:15 UTC

2 Instrument monitoring

2.1 CCD temperatures

2.1.1 OLCI-A

The long-term monitoring of the CCD temperatures is based on Radiometric Calibration Annotations (see Figure 1). Variations are very small (0.09 C peak-to-peak) and no trend can be identified. Data from current reporting period (rightmost data points) do not show any specificity.

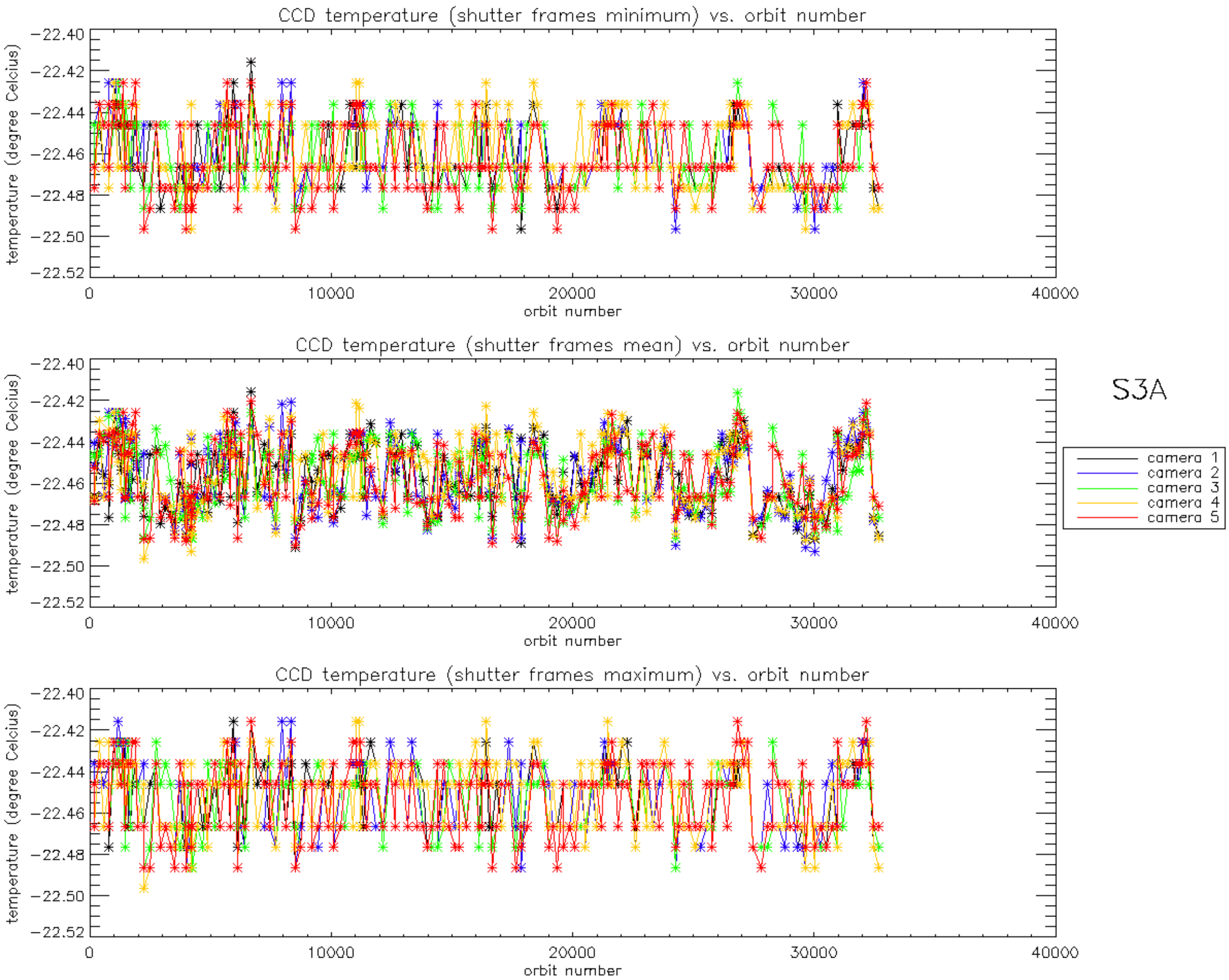

Figure 1: long term monitoring of OLCI-A CCD temperatures using minimum value (top), time averaged values (middle), and maximum value (bottom) provided in the annotations of the Radiometric Calibration Level 1 products, for the shutter frames, all radiometric calibrations so far except the first one (absolute orbit 183) for which the instrument was not yet thermally stable.

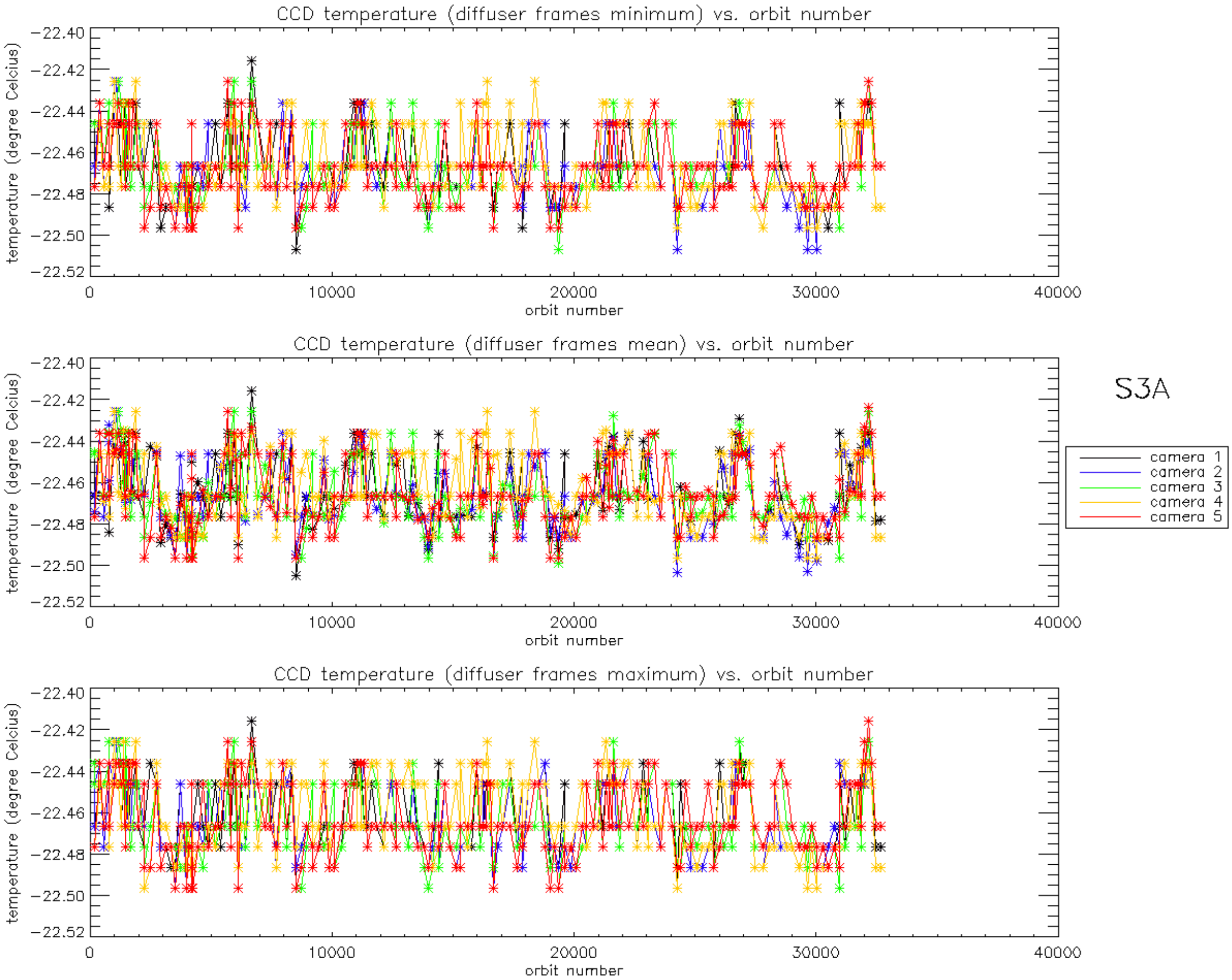

Figure 2: Same as Figure 1 for diffuser frames.

2.1.2 OLCI-B

As for OLCI-A, the variations of CCD temperature are very small (0.08 C peak-to-peak) and no trend can be identified. Data from current reporting period (rightmost data points) do not show any specificity.

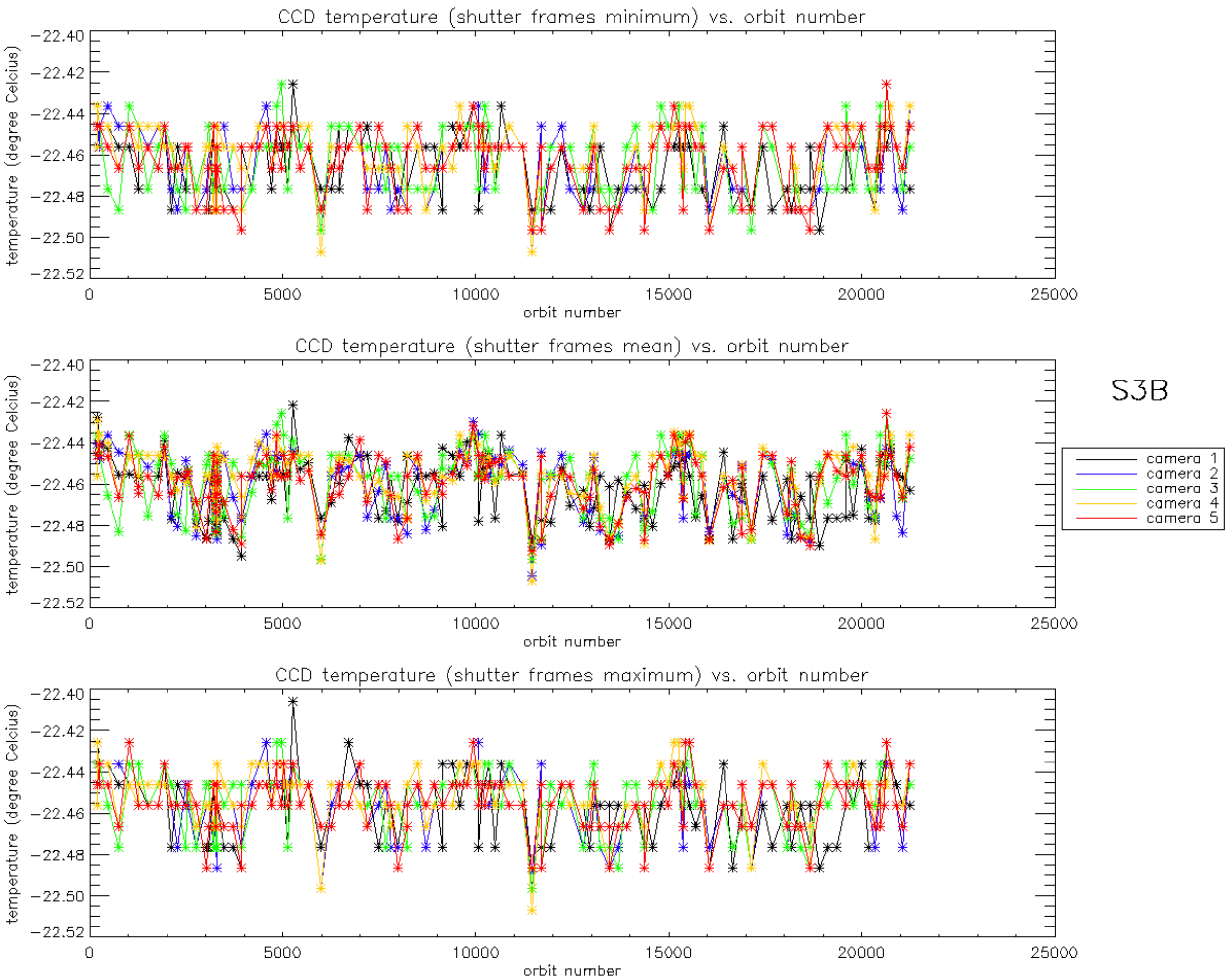

Figure 3: long term monitoring of OLCI-B CCD temperatures using minimum value (top), time averaged values (middle), and maximum value (bottom) provided in the annotations of the Radiometric Calibration Level 1 products, for the Shutter frames, all radiometric calibrations so far except the first one (absolute orbit 167) for which the instrument was not yet thermally stable.

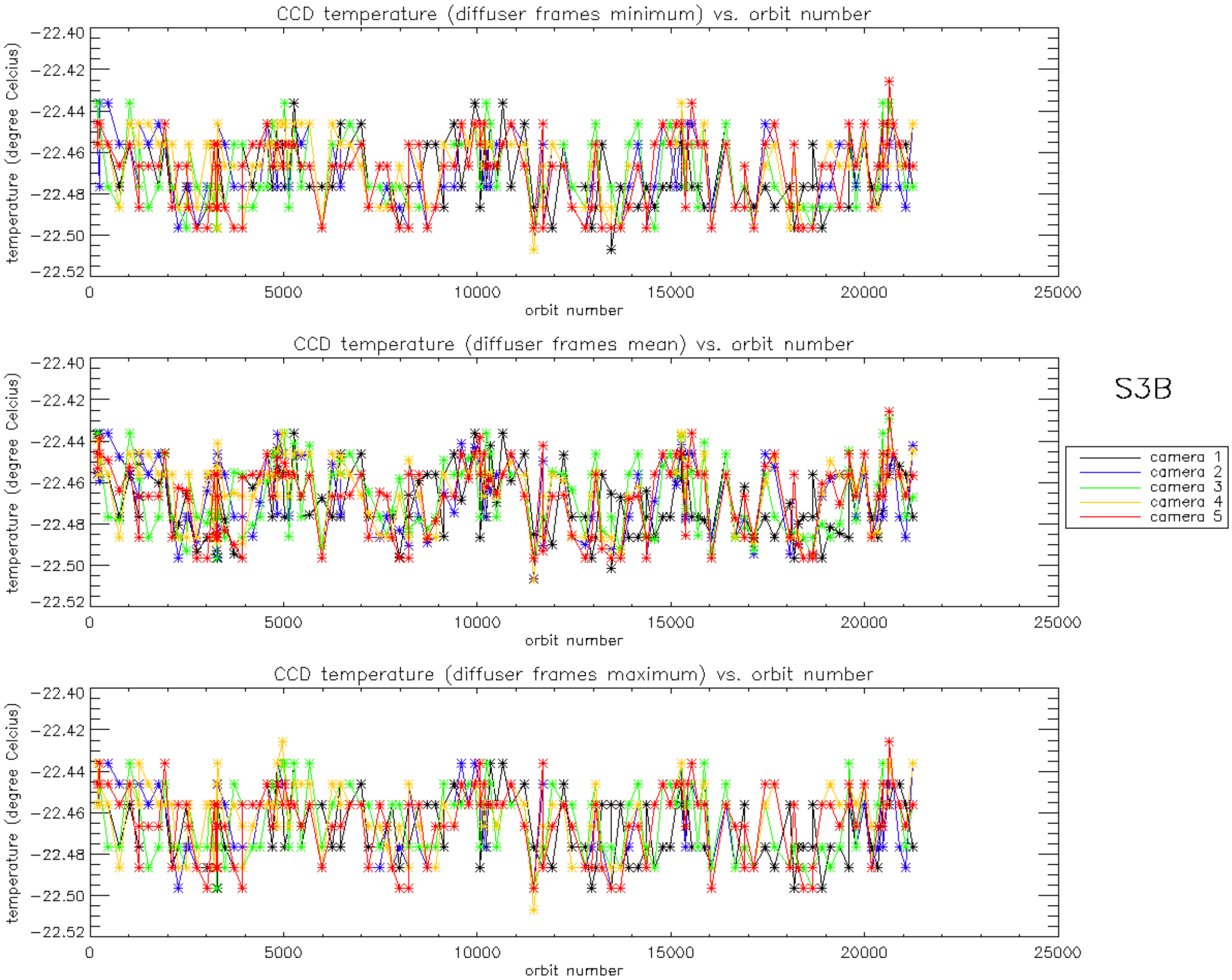

Figure 4: same as Figure 3 for diffuser frames.

2.2 Radiometric Calibration

For OLCI-A, two Radiometric Calibration sequences have been acquired during the reported period:

- S01 sequence (diffuser 1) on 11/05/2022 23:45 to 23:47 (absolute orbit 32457)
- S01 sequence (diffuser 1) on 27/05/2022 03:17 to 03:19 (absolute orbit 32673)

For OLCI-B, two Radiometric Calibration sequences have been acquired during the reported period:

- S01 sequence (diffuser 1) on 11/05/2022 04:35 to 04:37 (absolute orbit 21052)
- S01 sequence (diffuser 1) on 25/05/2022 06:52 to 06:54 (absolute orbit 21253)

The acquired Sun azimuth angles are presented on Figure 5 for OLCI-A and Figure 6 for OLCI-B, on top of the nominal values without Yaw Manoeuvre (i.e. with nominal Yaw Steering control of the satellite).

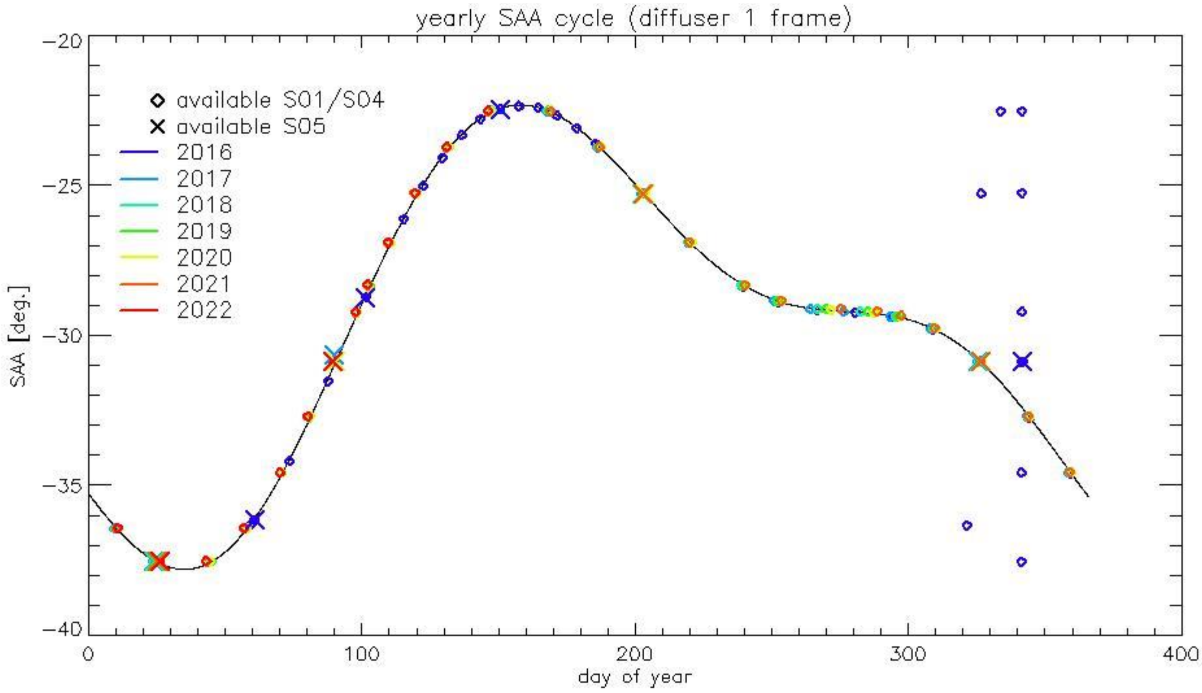

Figure 5: Sun azimuth angles during acquired OLCI-A Radiometric Calibrations (diffuser frame) on top of nominal yearly cycle (black curve). Diffuser 1 with diamonds, diffuser 2 with crosses. Different colours correspond to different years of acquisition (see the legend inside the figure).

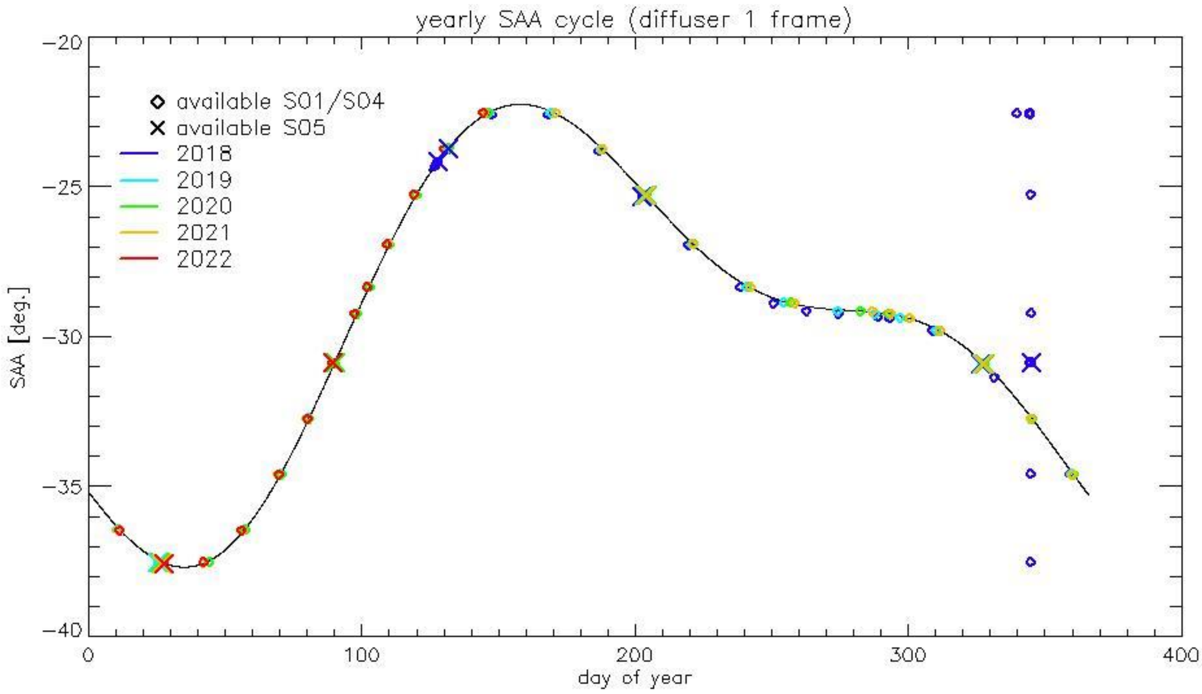

Figure 6: same as Figure 5 for OLCI-B.

Sun Zenith Angles as a function of Sun Azimuth Angles are presented in Figure 7 for OLCI-A and Figure 8 for OLCI-B.

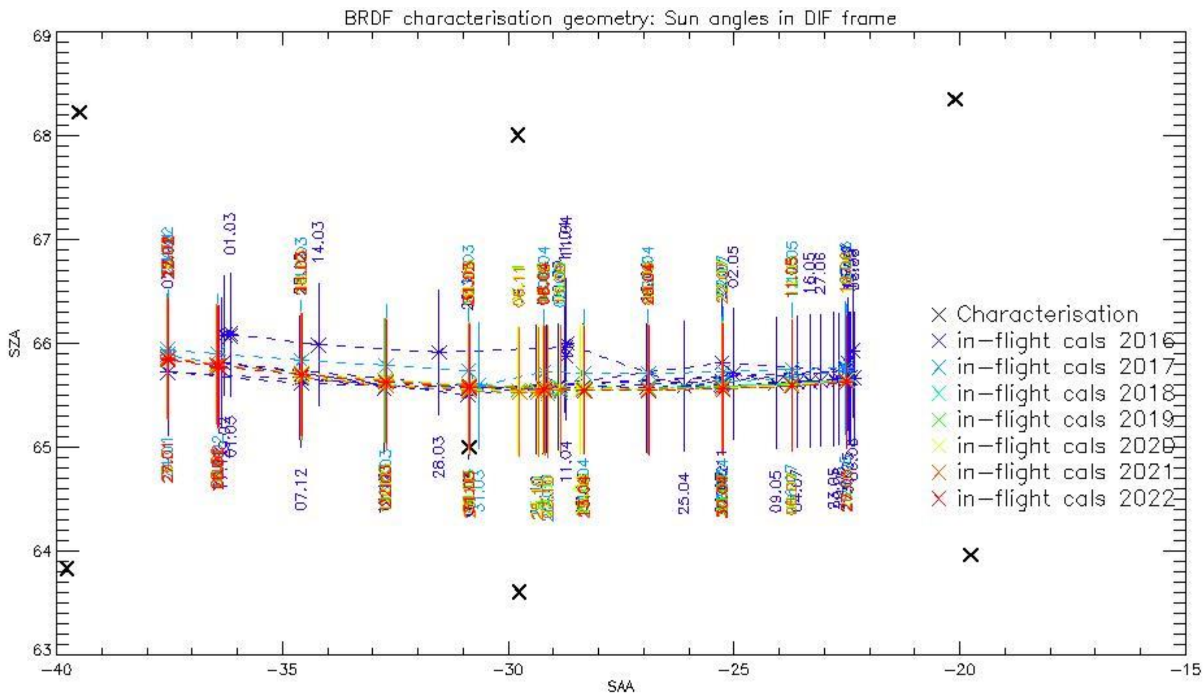

Figure 7: OLCI-A Sun geometry during radiometric Calibrations on top of characterization ones (diffuser frame)

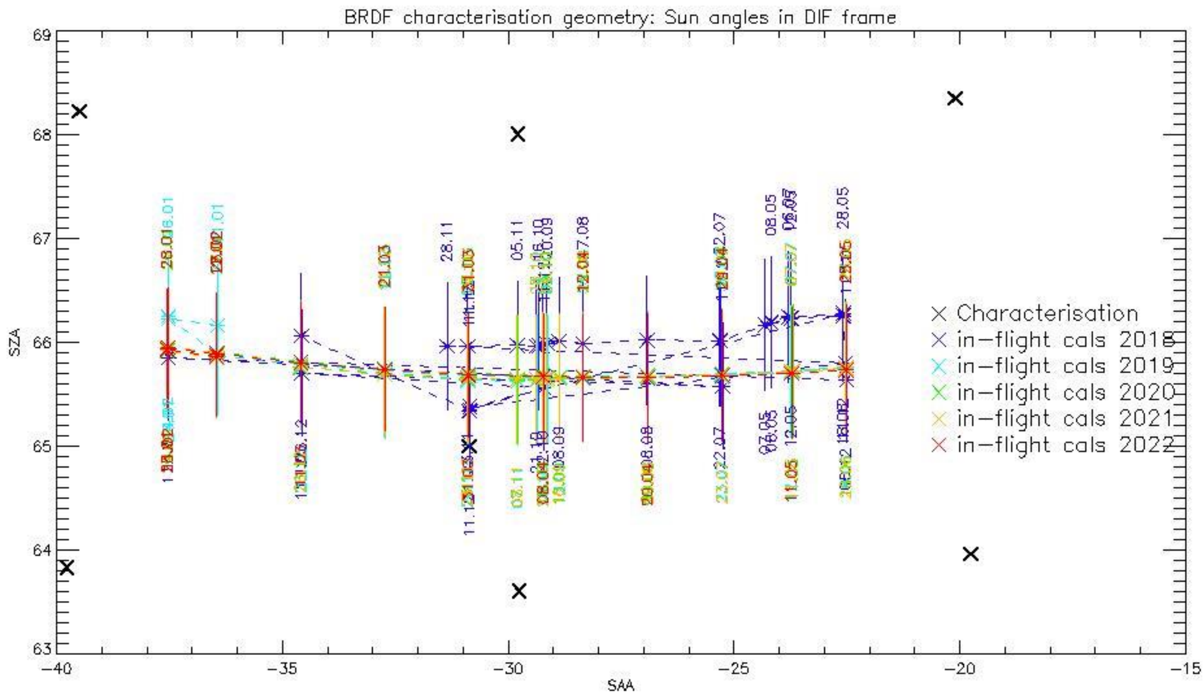

Figure 8: same as Figure 7 for OLCI-B

2.2.1 Dark Offsets [OLCI-L1B-CV-230]

Note about the High Energy Particles:

The filtering of High Energy Particle (HEP) events from radiometric calibration data has been implemented (for shutter frames only) in a post processor, allowing generating Dark Offset and Dark Current tables computed on filtered data. The post-processor starts from IPF intermediate data (corrected counts), applies the HEP detection and filtering and finally computes the Dark Offset and Dark Current tables the same way as IPF. An example of the impact of HEP filtering is given in Figure 9.

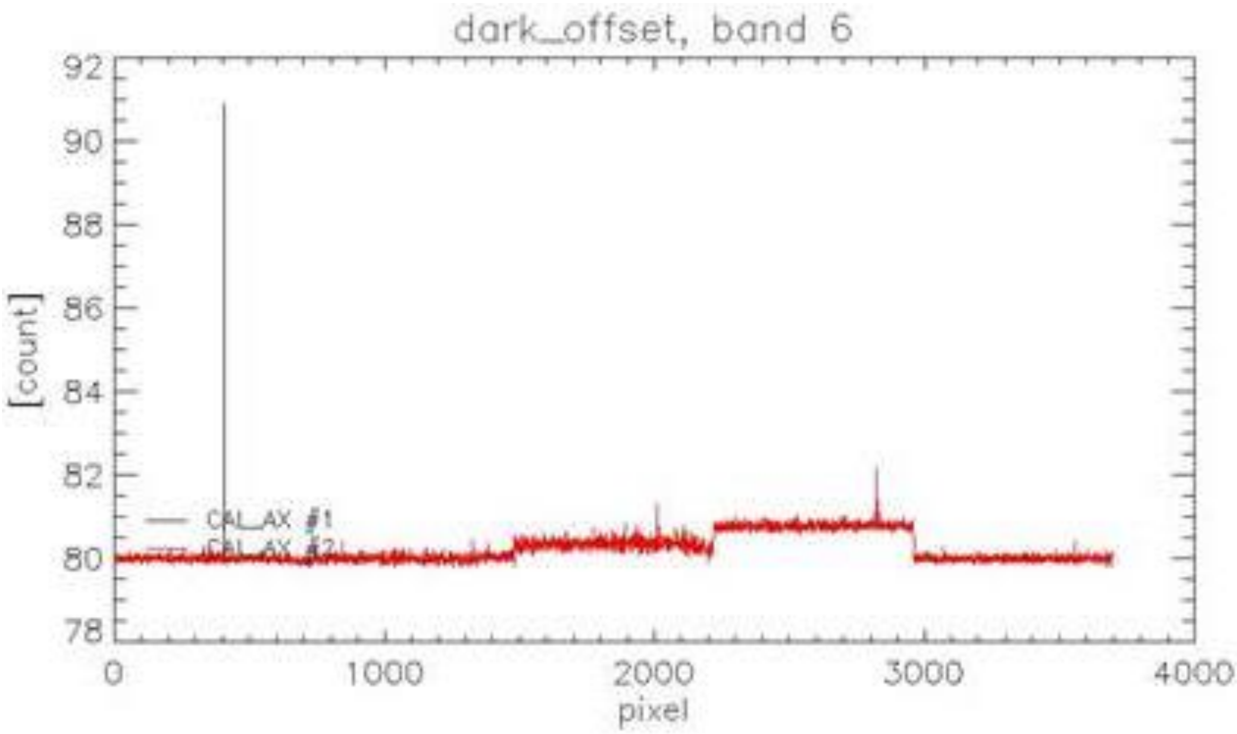

Figure 9: Dark Offset table for band Oa06 with (red) and without (black) HEP filtering (Radiometric Calibration of 22 July 2017). The strong HEP event near pixel 400 has been detected and removed by the HEP filtering.

All results presented below in this section have been obtained using the HEP filtered Dark Offset and Dark Current tables.

2.2.1.2 OLCI-A

Dark offsets

Dark offsets are continuously affected by the global offset induced by the Periodic Noise on the OCL (Offset Control Loop) convergence. Current reporting period calibrations are affected the same way as others. The amplitude of the shift varies with band and camera from virtually nothing (e.g. camera 2, band 0a1) to up to 5 counts (Oa21, camera 3). The Periodic Noise itself comes on top of the global shift with its known signature: high frequency oscillations with a rapid damp. This effect remains more or less stable with time in terms of amplitude, frequency and decay length, but its phase varies with time, introducing the global offset mentioned above.

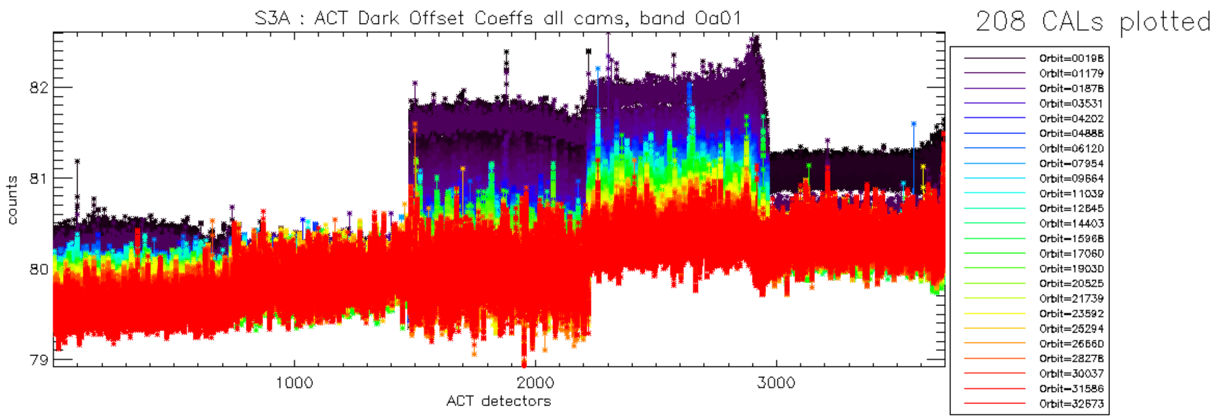

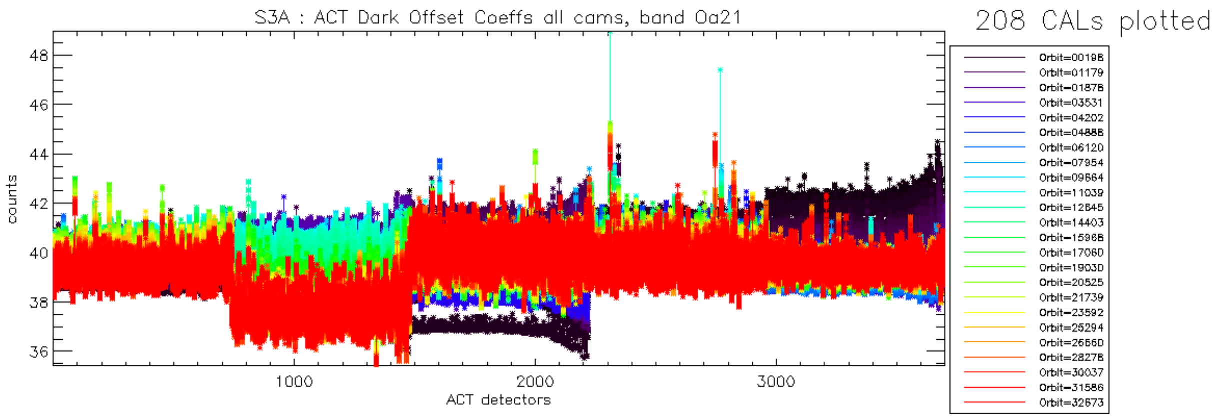

Figure 10: OLCI-A Dark Offset for band Oa1 (top) and Oa21 (bottom), all radiometric calibrations so far except the first one (orbit 183) for which the instrument was not thermally stable yet.

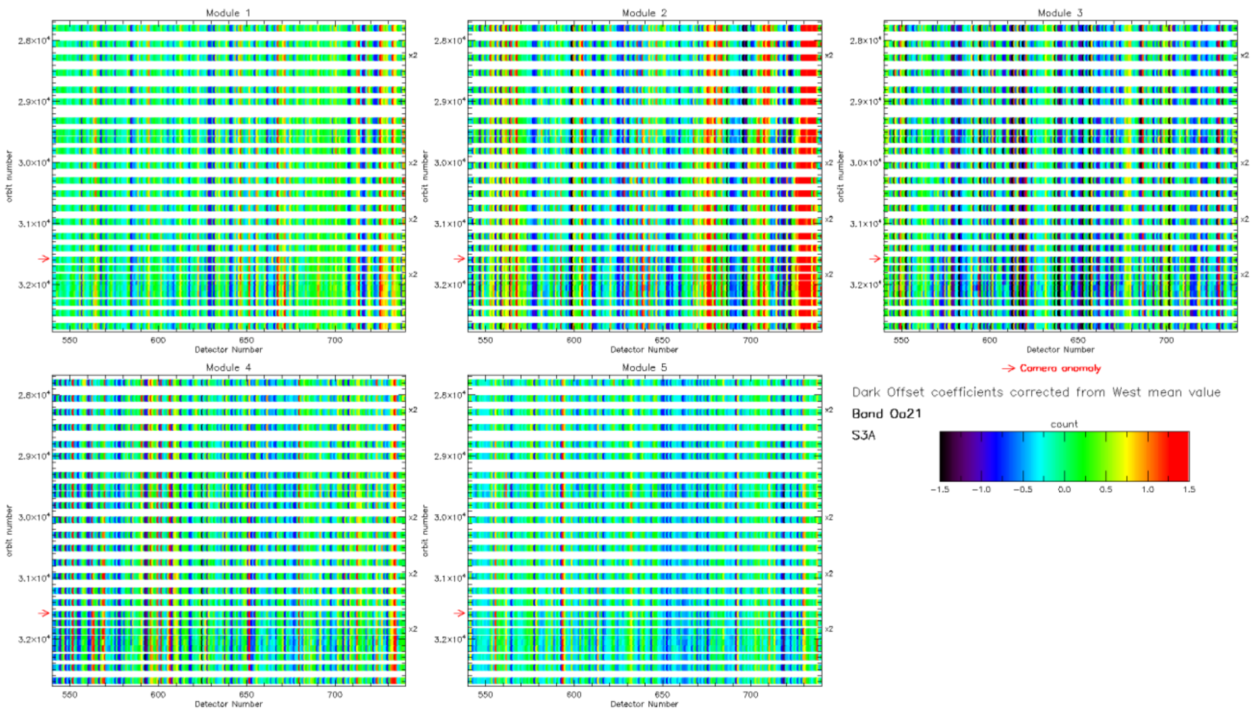

Figure 11: map of OLCI-A periodic noise for the 5 cameras, for band Oa21. X-axis is detector number (East part, from 540 to 740, where the periodic noise occurs), Y-axis is the orbit number. Y-axis range is focused on the most recent 5000 orbits. The counts have been corrected from the West detectors mean value (not affected by periodic noise) in order to remove mean level gaps and consequently to have a better visualisation of the long term evolution of the periodic noise structure. At the beginning of the mission the periodic noise for band Oa21 had strong amplitude in camera 2, 3 and 5 compared to camera 1 and 4. However PN evolved through the

mission and these discrepancies between cameras have been reduced. At the time of this Cyclic Report Camera 2 still shows a slightly higher PN than other cameras.

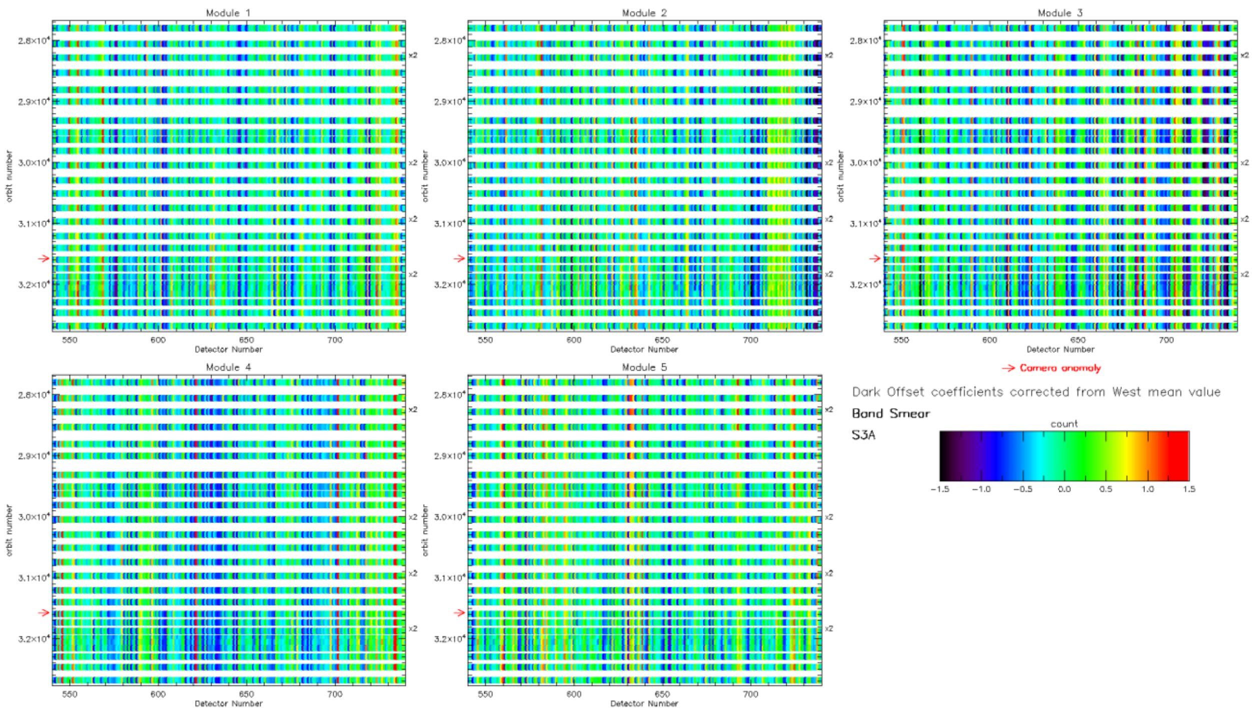

Figure 12: same as Figure 11 for smear band.

Figure 11 and Figure 12 show the so-called ‘map of periodic noise’ in the 5 cameras, for respectively band 21 and smear band. These maps have been computed from the dark offsets after removal of the mean level of the WEST detectors (not impacted by PN) in order to remove mean level gaps from one CAL to the other and consequently to highlight the shape of the PN. Maps are focused on the last 200 EAST detectors where PN occurs and on a time range covering only the last 5000 orbits in order to better visualize the CALs of the current reporting period.

Figure 11 and Figure 12 show that at this stage of the mission the PN is very stable in all cameras. There is no special behaviour noticed during the reporting period.

<u>Dark Currents</u>

Dark Currents (Figure 13) are not affected by the global offset of the Dark Offsets, thanks to the clamping to the average blind pixels value. However, the oscillations of Periodic Noise remain visible. There is no significant evolution of this parameter during the current reporting period except the small regular increase (almost linear), for all detectors, since the beginning of the mission (see Figure 14).

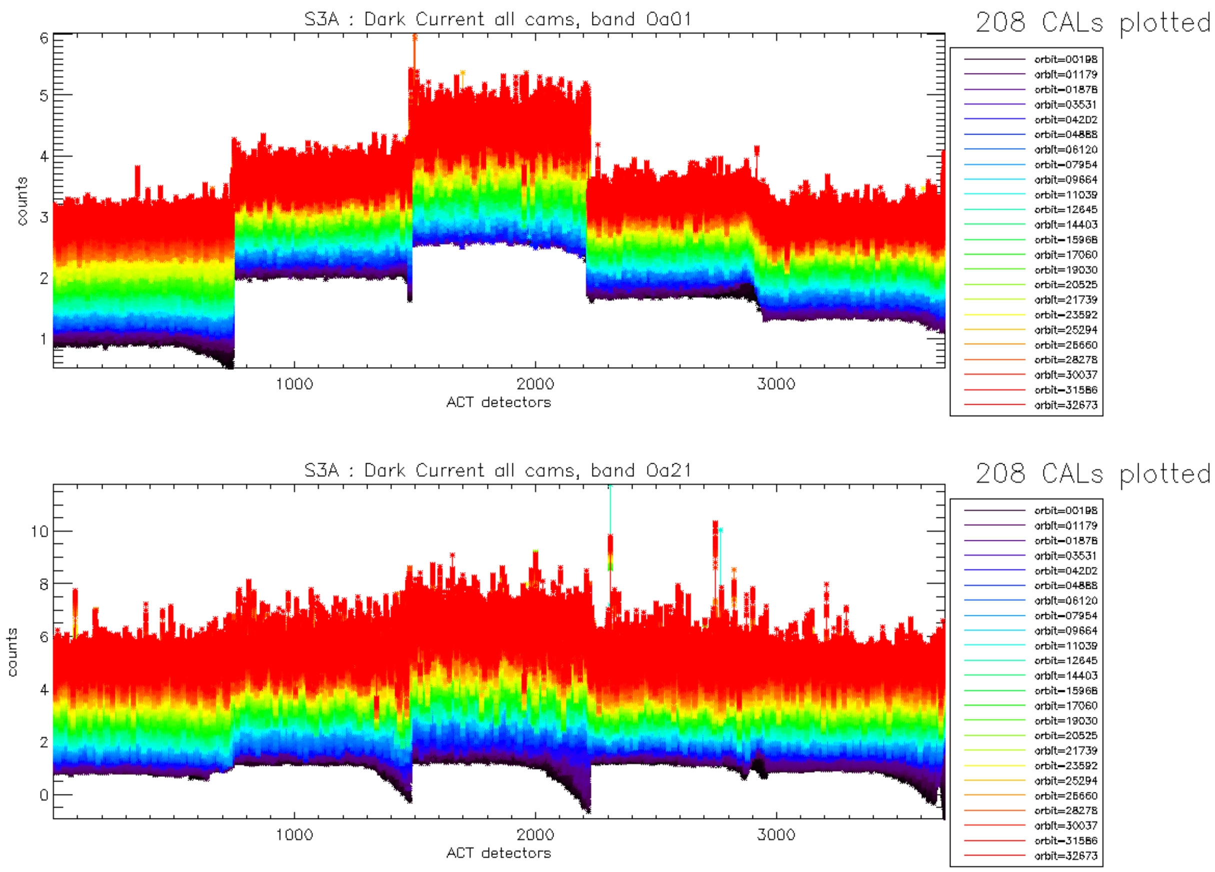

Figure 13: OLCI-A Dark Current for band Oa1 (top) and Oa21 (bottom), all radiometric calibrations so far except the first one (orbit 183) for which the instrument was not thermally stable yet.

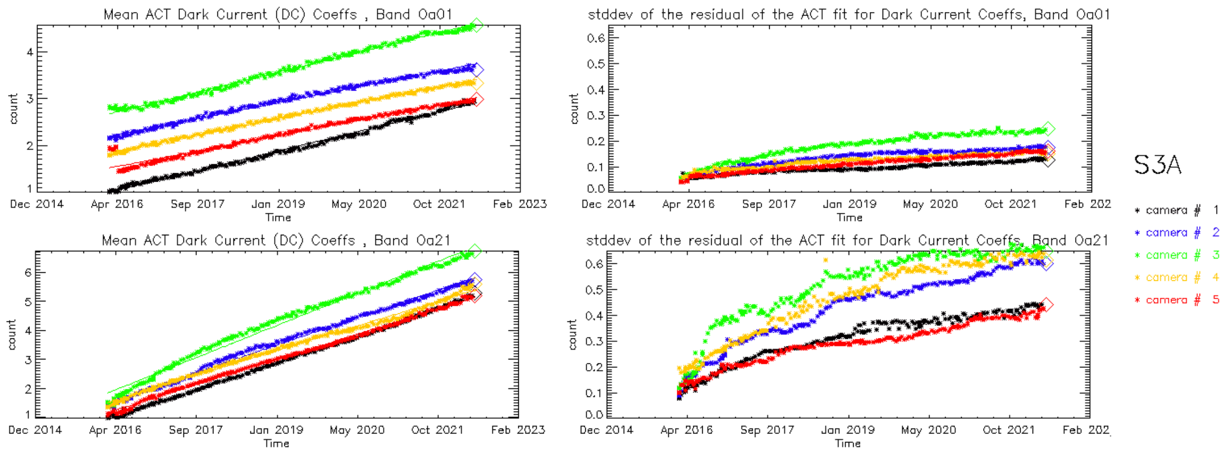

Figure 14: left column: ACT mean on 400 first detectors of OLCI-A Dark Current coefficients for spectral band Oa01 (top) and Oa21 (bottom). Right column: same as left column but for Standard deviation instead of mean. We see an increase of the DC level as a function of time especially for band Oa21.

A possible explanation of the regular increase of DC could be the increase of the number of hot pixels which is more important in Oa21 because this band is made of more CCD lines than band Oa01 and thus receives more cosmic rays impacts. It is known that cosmic rays degrade the structure of the CCD, generating more and more hot pixels at long term scales. Indeed, when computing the time slopes of the spatially averaged Dark Current as a function of band, i.e. the slopes of curves in left plots of Figure 14, one can see that Oa21 is by far the most affected, followed by the smear band (Figure 15, left); when plotting these slopes against total band width (in CCD rows, regardless of the number of micro-bands), the correlation between the slope values and the width becomes clear (Figure 15, right).

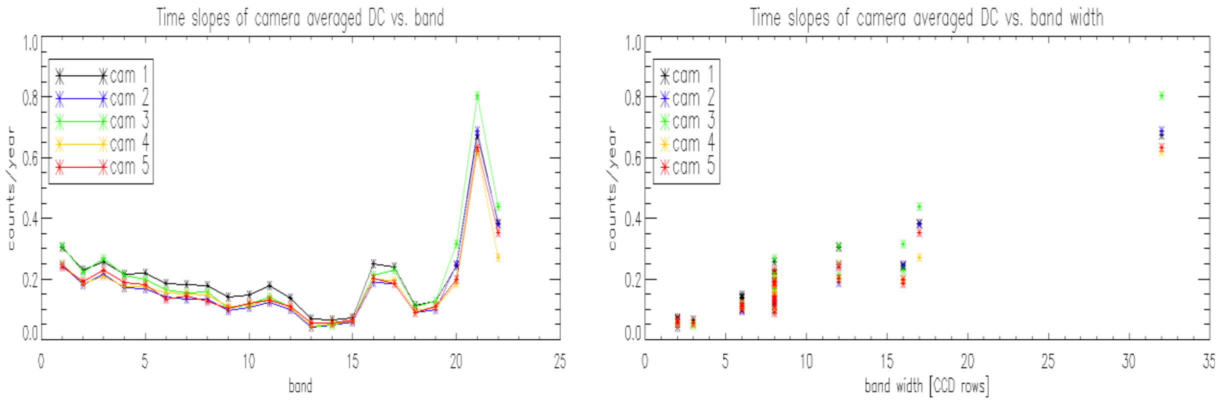

Figure 15: OLCI-A Dark current increase rates with time (in counts per year) vs. band (left) and vs. band width (right)

2.2.1.3 OLCI-B

Dark Offsets

Dark offsets for OLCI-B show a similar behaviour than for OLCI-A: mean level gaps between different orbits, induced by the presence of a pseudo periodic noise on the east edge of the cameras with a drifting phase.

Evolution of OLCI-B Dark Offset coefficients for band Oa01 and Oa21 are represented in Figure 16.

The periodic noise maps are shown for band Oa21 and smear band respectively in Figure 17 and Figure 18. As it happened for OLCI-A after a few thousands of orbits, the strong periodic noise phase and amplitude drift, present at the very beginning of the mission is now showing a clear stabilization.

Despite this overall stabilization, small evolutions are still noticeable in some bands/camera, like for example camera 1 in band Oa21 (upper left map in Figure 17) or in camera 1 band smear (upper left map in Figure 18).

Globally, OLCI-B PN is slightly less stabilized than OLCI-A PN.

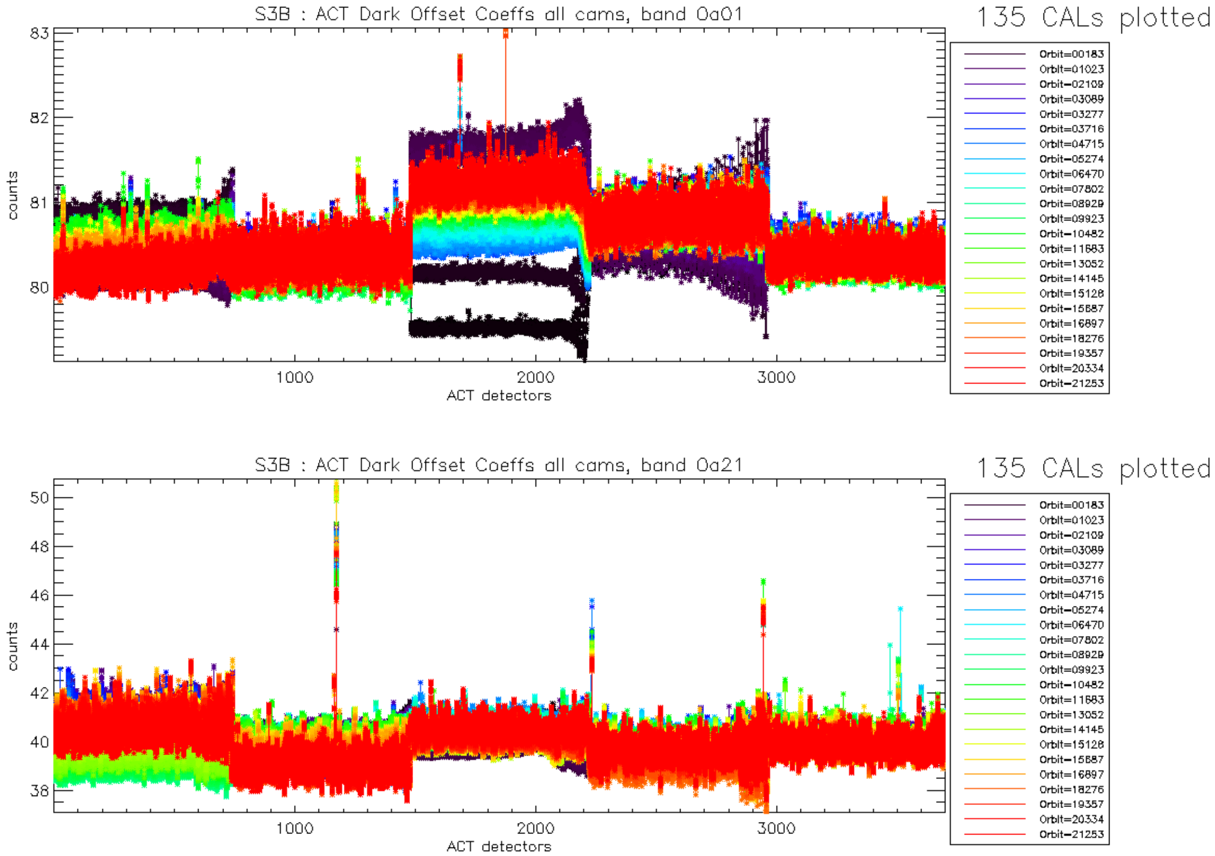

Figure 16: OLCI-B Dark Offset for band Oa1 (top) and Oa21 (bottom), all radiometric calibrations so far except the first one (orbit 167) for which the instrument was not thermally stable yet.

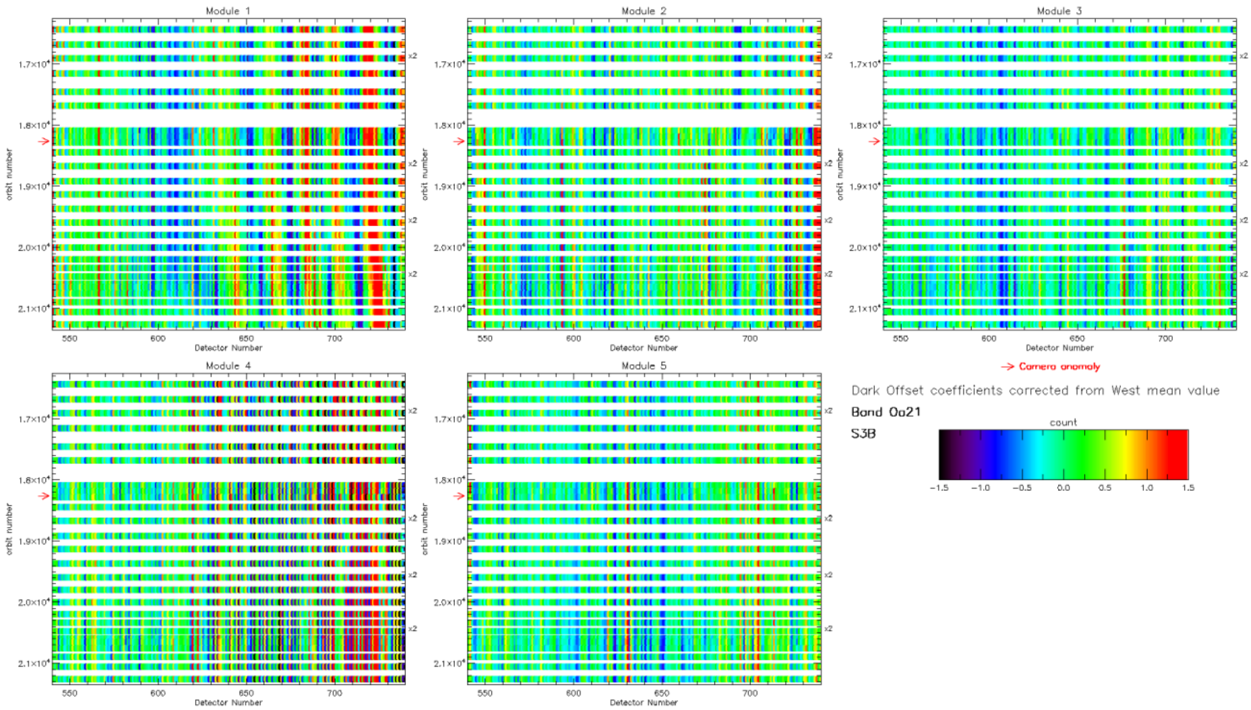

Figure 17: OLCI-B map of periodic noise for the 5 cameras, for band Oa21. X-axis is detector number (East part, from 540 to 740, where the periodic noise occurs), Y-axis is the orbit number. The counts have been corrected from the West detectors mean value (not affected by periodic noise) in order to remove mean level gaps and consequently to have a better visualisation of the long term evolution of the periodic noise structure.

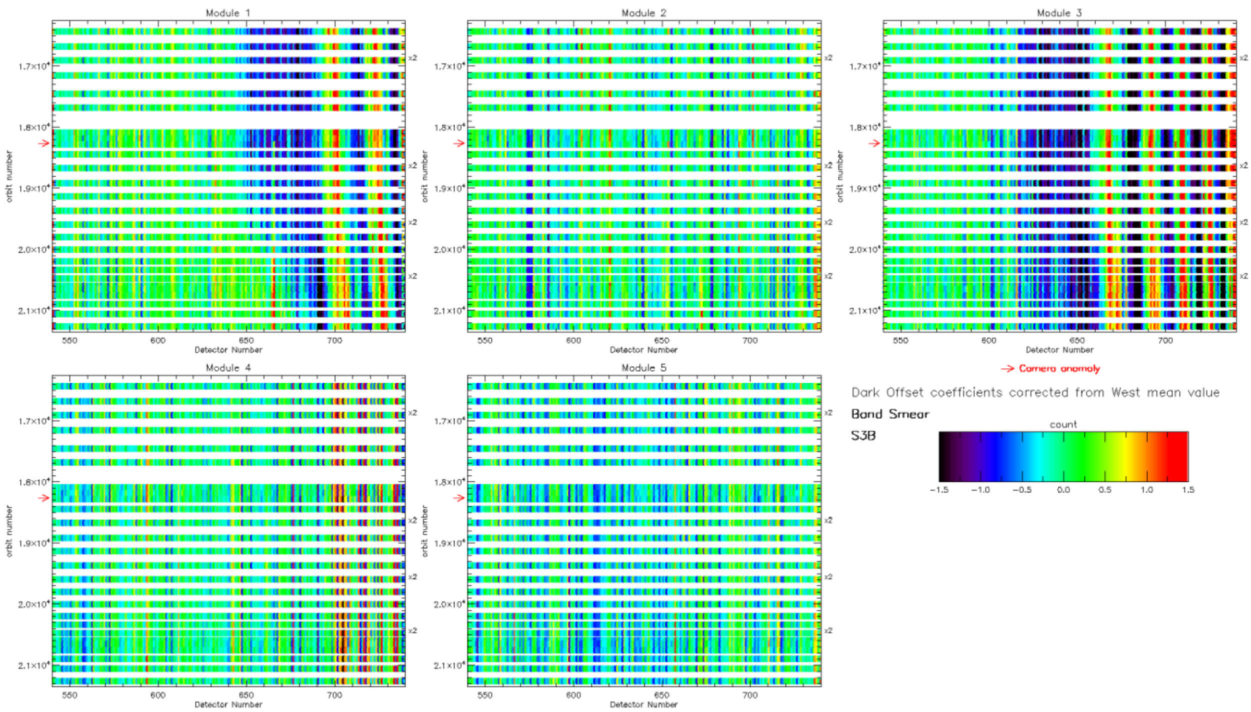

Figure 18: same as Figure 17 for smear band.

Dark Currents

As for OLCI-A there is no significant evolution of the Dark Current coefficients (Figure 19) during the current reporting period except the small regular increase (almost linear), for all detectors, since the beginning of the mission (see Figure 20) probably due to an increase of hot pixels (see Figure 21).

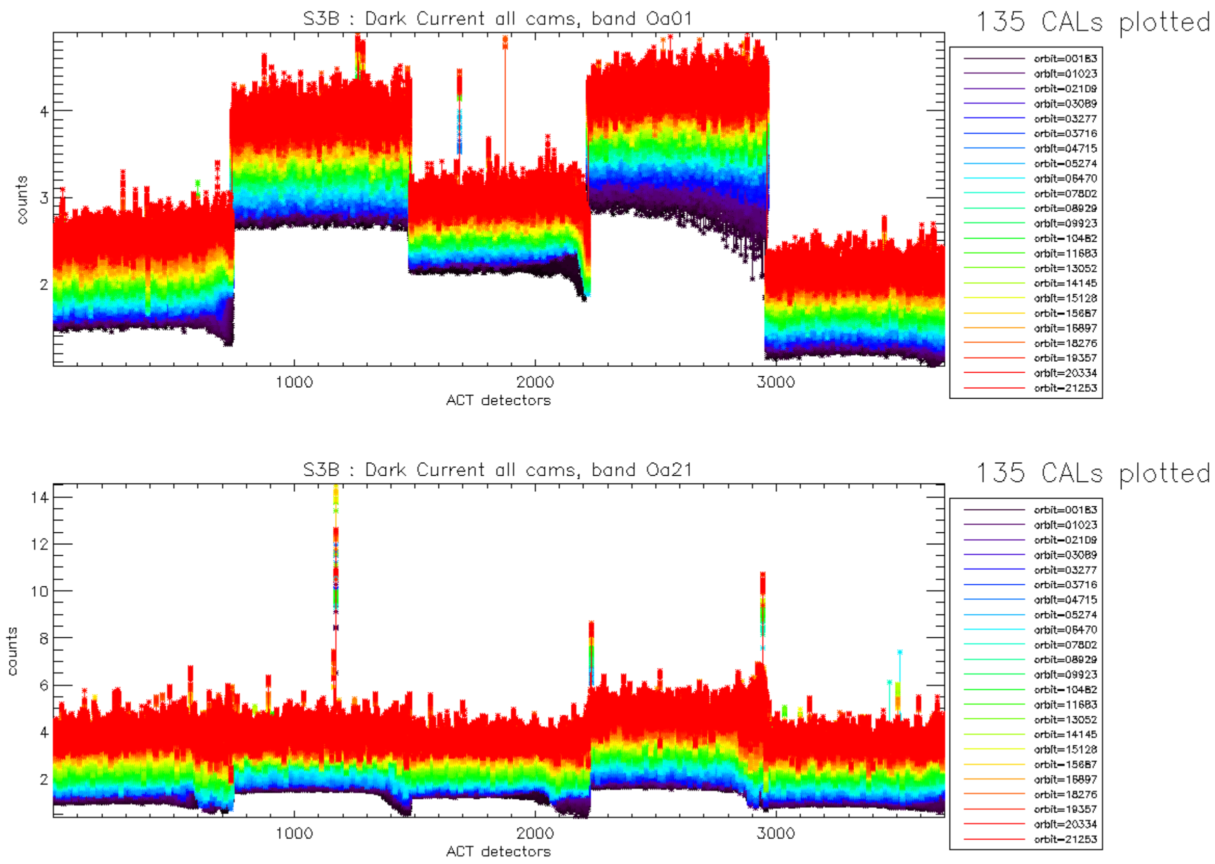

Figure 19: OLCI-B Dark Current for band Oa1 (top) and Oa21 (bottom), all radiometric calibrations so far except the first one (orbit 167) for which the instrument was not thermally stable yet.

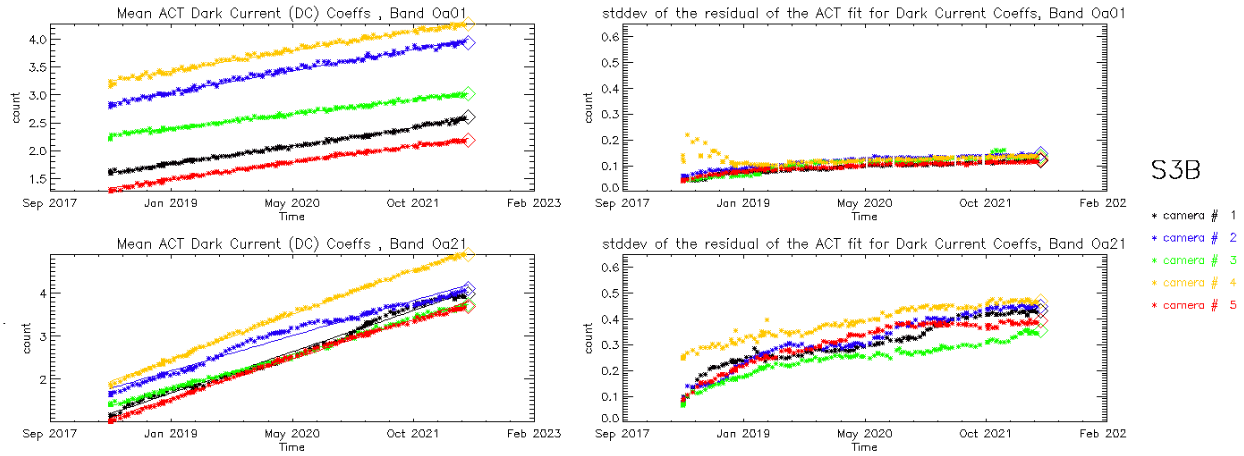

Figure 20: left column: ACT mean on 400 first detectors of OLCI-B Dark Current coefficients for spectral band Oa01 (top) and Oa21 (bottom). Right column: same as left column but for Standard deviation instead of mean. We see an increase of the DC level as a function of time especially for band Oa21.

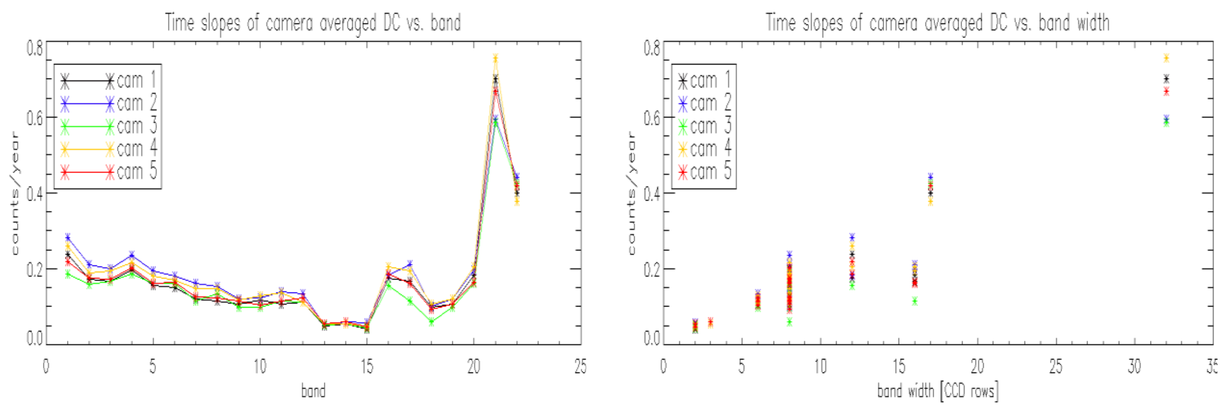

Figure 21: OLCI-B Dark Current increase rates with time (in counts per year) vs. band (left) and vs. band width (right)

2.2.2 Instrument response and degradation modelling [OLCI-L1B-CV-250]

2.2.2.1 Instrument response monitoring

2.2.2.1.1 OLCI-A

Figure 22 shows the gain coefficients of every pixel for two OLCI-A channels, Oa1 (400 nm) and Oa21 (1020 nm), highlighting the significant evolution of the instrument response since early mission.

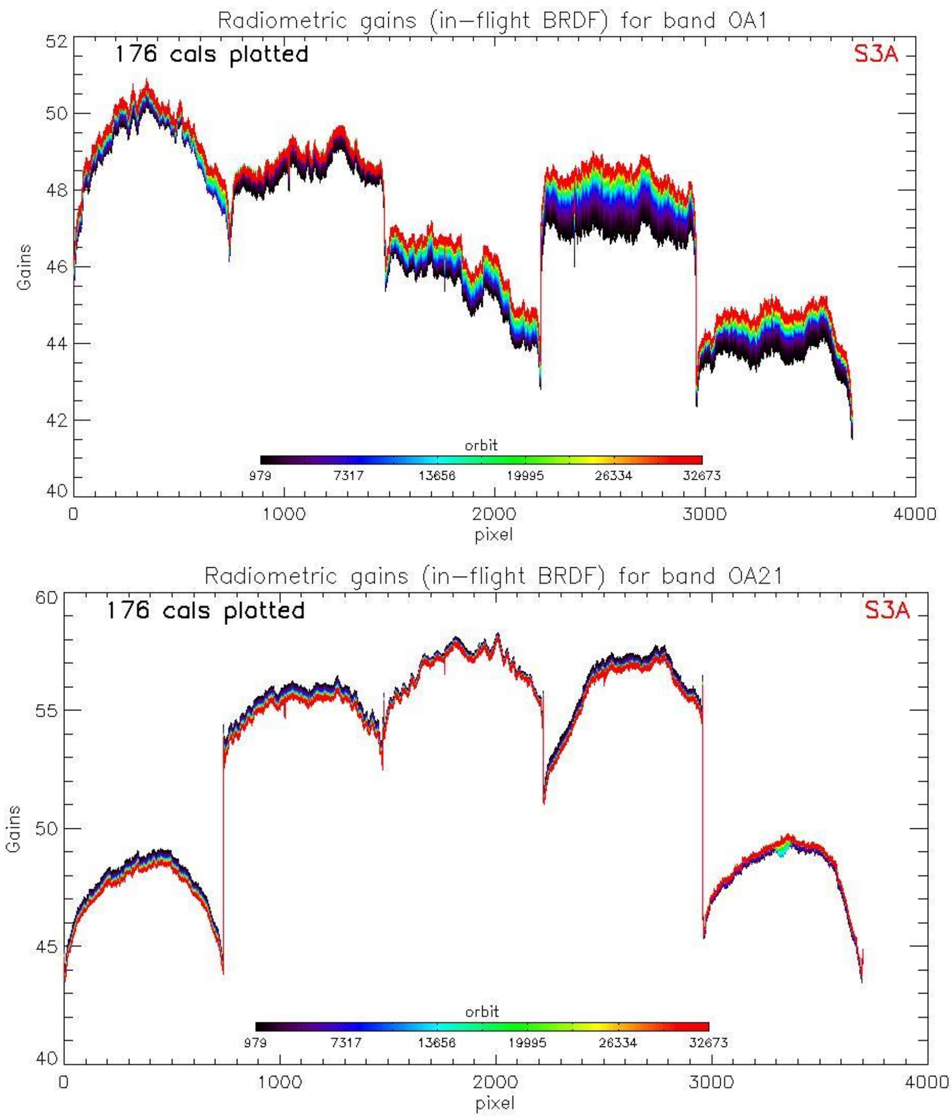

Figure 22: OLCI-A Gain Coefficients for band Oa1 (top) and Oa21 (bottom), derived using the in-flight BRDF model. The dataset is made of all diffuser 1 radiometric calibrations since orbit 979.

Figure 23 displays a summary of the time evolution of the cross-track average of the gains (in-flight BRDF, taking into account the diffuser ageing), for each module, relative to a given reference calibration (the 25/04/2016, change of OLCI channel settings). It shows that, if a significant evolution occurred during the early mission, the trends tend in general to stabilize, with some exceptions (e.g. band 1 of camera 1 and 4, bands 2 & 3 of camera 5).

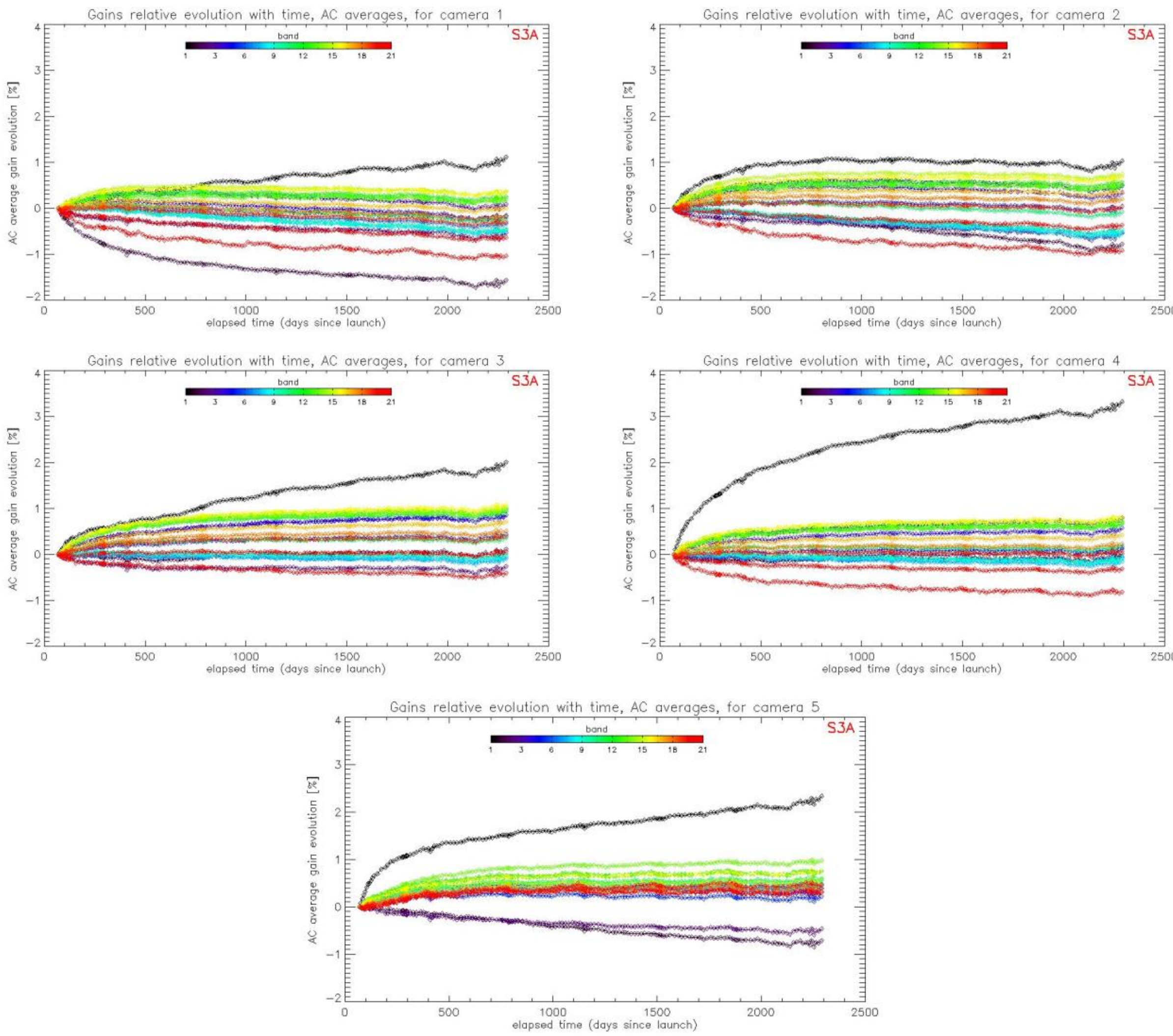

Figure 23: camera averaged gain relative evolution with respect to calibration of 25/04/2016 (change of OLCI channel settings), as a function of elapsed time since the beginning of the mission; one curve for each band (see colour code on plots), one plot for each module. The diffuser ageing is taken into account.

2.2.2.1.2 OLCI-B

Figure 24 shows the gain coefficients of every pixel for two OLCI-B channels, Oa1 (400 nm) and Oa21 (1020 nm), highlighting the significant evolution of the instrument response since early mission.

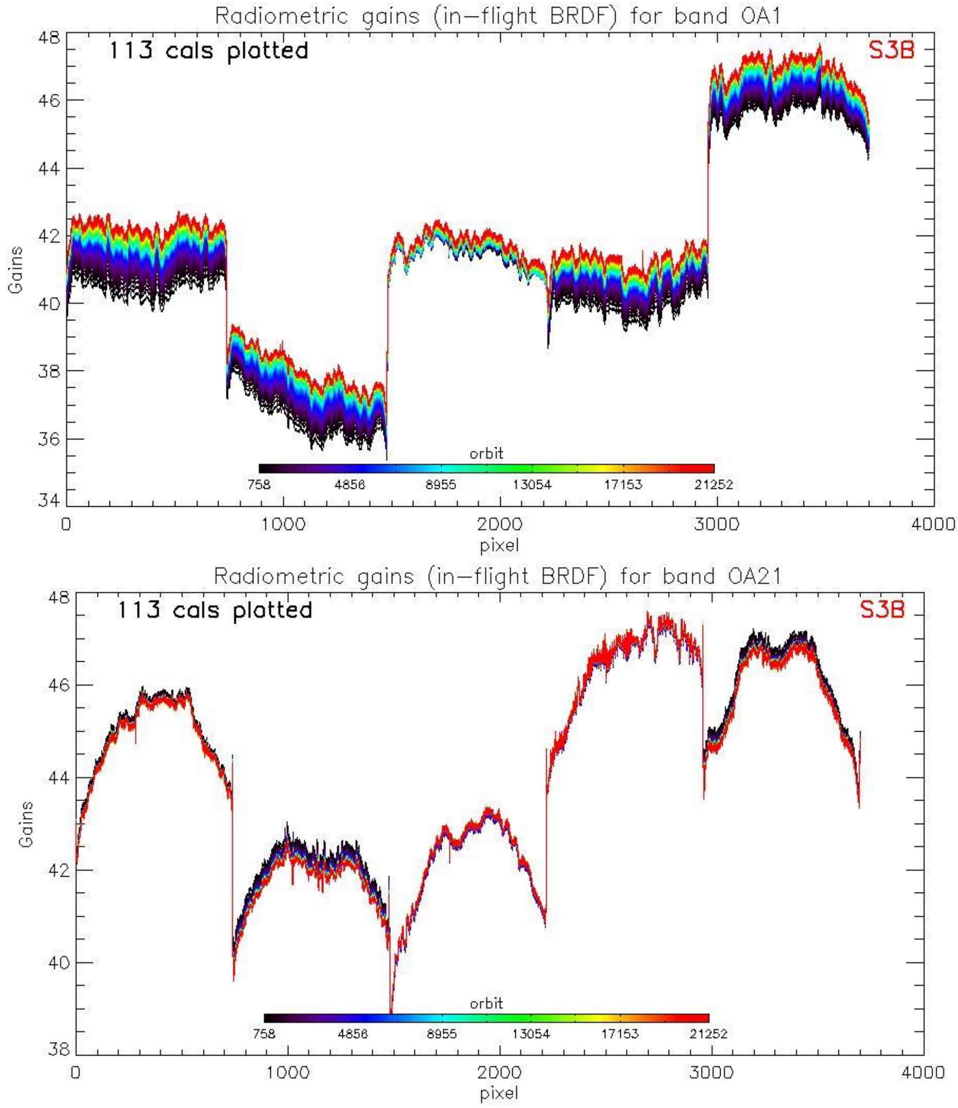

Figure 24: OLCI-B Gain Coefficients for band Oa1 (top) and Oa21 (bottom), derived using the in-flight BRDF model. The dataset is made of all diffuser 1 radiometric calibrations since orbit 758.

Figure 25 displays a summary of the time evolution of the cross-track average of the gains (in-flight BRDF, taking into account diffuser ageing), for each module, relative to a given reference calibration (first calibration after channel programming change: 18/06/2018). It shows that, if a significant evolution occurred during the early mission, the trends tend to stabilize. The large amount of points near elapsed time = 220 days is due to the yaw manoeuvre campaign. The slight discontinuity near "day 920 since launch" is due to the upgrade of the Ageing model.

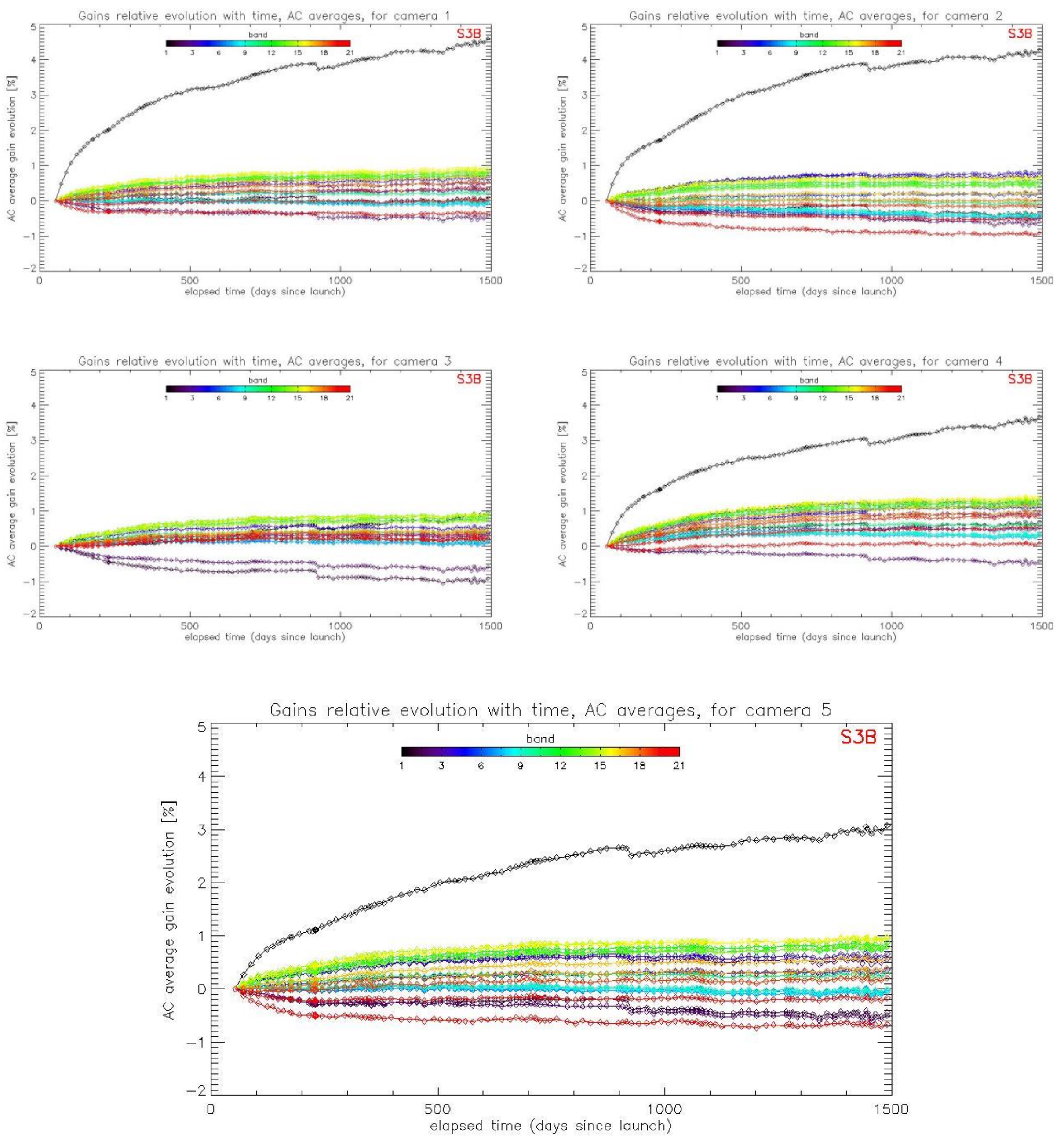

Figure 25: OLCI-B camera averaged gain relative evolution with respect to first calibration after channel programming change (18/06/2018), as a function of elapsed time since the beginning of the mission; one curve for each band (see colour code on plots), one plot for each module. The diffuser ageing is taken into account.

2.2.2.2 Instrument evolution modelling

2.2.2.2.1 OLCI-A

The current OLCI-A Radiometric Model has been put in operations at PDGS the 18/11/2021 (Processing Baseline 3.01). This model has been derived on the basis of a more recent (compared to the previous model) Radiometric Calibration dataset, going from 25/01/2018 to 03/10/2021. It includes the correction of the diffuser ageing for the six bluest bands (Oa1 to Oa6) for which it is clearly measurable. The model performance over the complete dataset (including the 19 calibrations in extrapolation over about 7 months) remains better than about 0.12% for all bands at the exception of the presence of an isolated peak in the recent data near orbit 30500 where performance degrades for all bands, up to about 0.13% for band Oa01. This peak is present in Gain measurements, thus reflects in model performance. The same behaviour is seen on OLCI-B (see Figure 33), suggesting that it is not linked to the instrument sensitivity. A small drift of the model with respect to the most recent data is now visible for all bands. The previous model, trained on a Radiometric Dataset limited to 08/08/2020, shows clearly a more pronounced drift of the model with respect to most recent data (Figure 27). Comparison of the two figures shows the improvement brought by the updated Model over almost all the mission. Performance shown on Figure 26 adopts, as for OLCI-B, the multiple model approach, i.e. different models (three for OLCI-A since PB, three for OLCI-B since PB 1.57) are used to cover the whole mission (red dashed line on Figure 26), each model being fitted on a partial dataset (green dashed line on Figure 26) whose coverage is optimised to provide best performance.

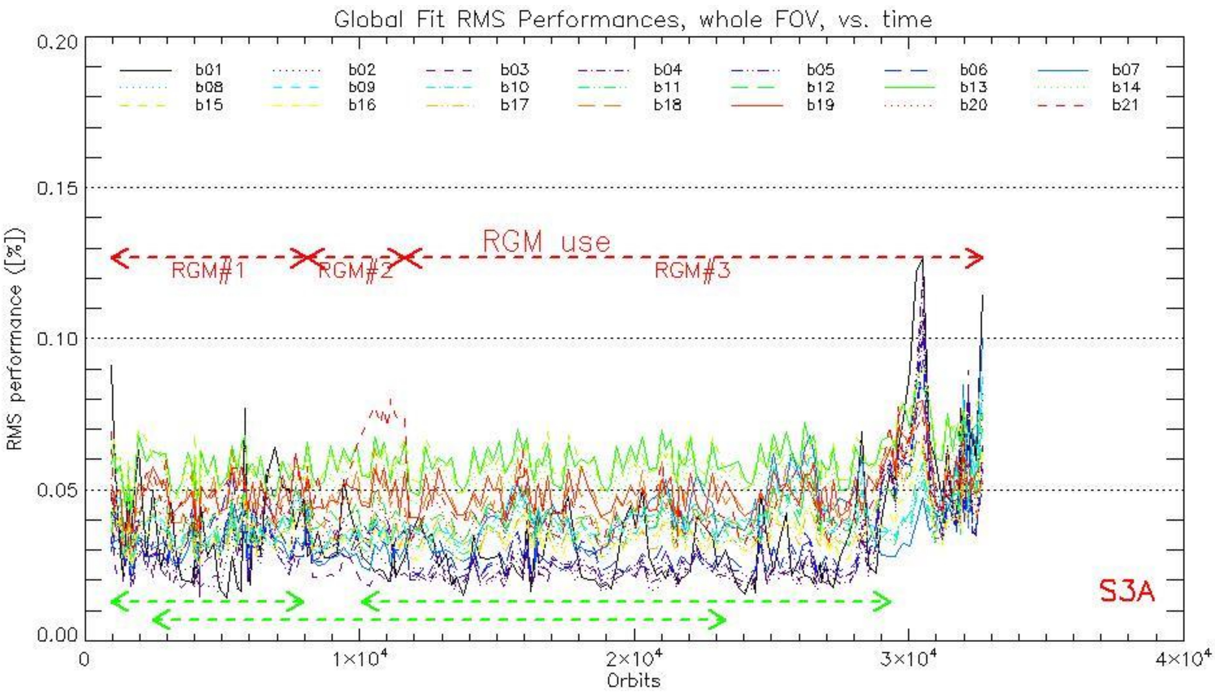

Figure 26: RMS performance of the OLCI-A Gain Model of the current processing baseline as a function of orbit.

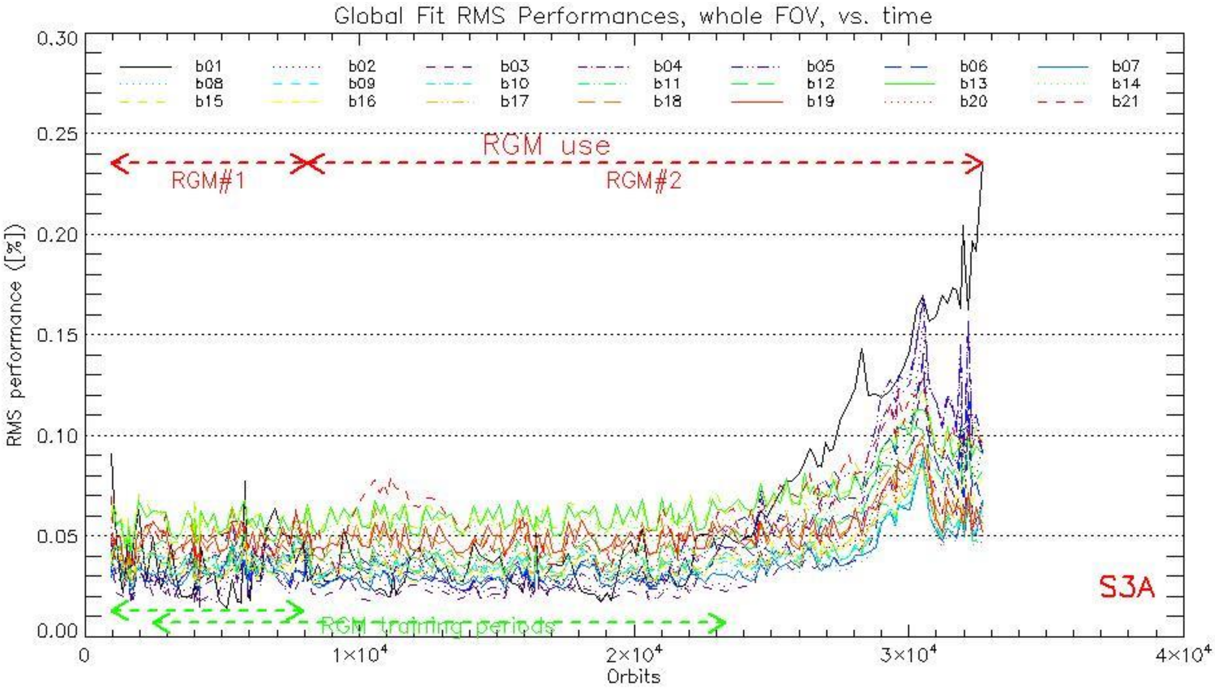

Figure 27: RMS performance of the OLCI-A Gain Model of the previous Processing Baseline as a function of orbit.

The overall instrument evolution since channel programming change (25/04/2016) is shown on Figure 28.

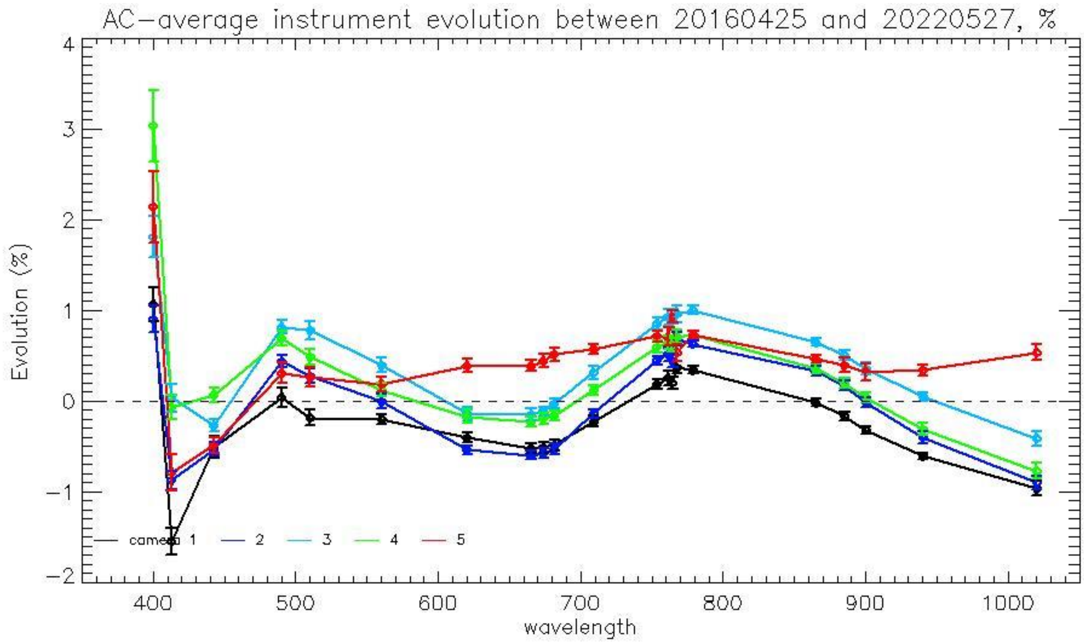

Figure 28: OLCI-A Camera-averaged instrument evolution since channel programming change (25/04/2016) and up to the most recent calibration (27/05/2022) versus wavelength.

The overall per camera performance, as a function of wavelength, and at each orbit is shown on Figure 29 as the average and standard deviation of the model over data ratio.

Finally, Figure 30 to Figure 32 show the detail of the model performance, with across-track plots of the model over data ratios at each orbit, one plot for each channel.

Comparisons of Figure 30 to Figure 32 with their counterparts in Report of Cycle 62 clearly demonstrate the improvement brought by the new model whatever the level of detail.

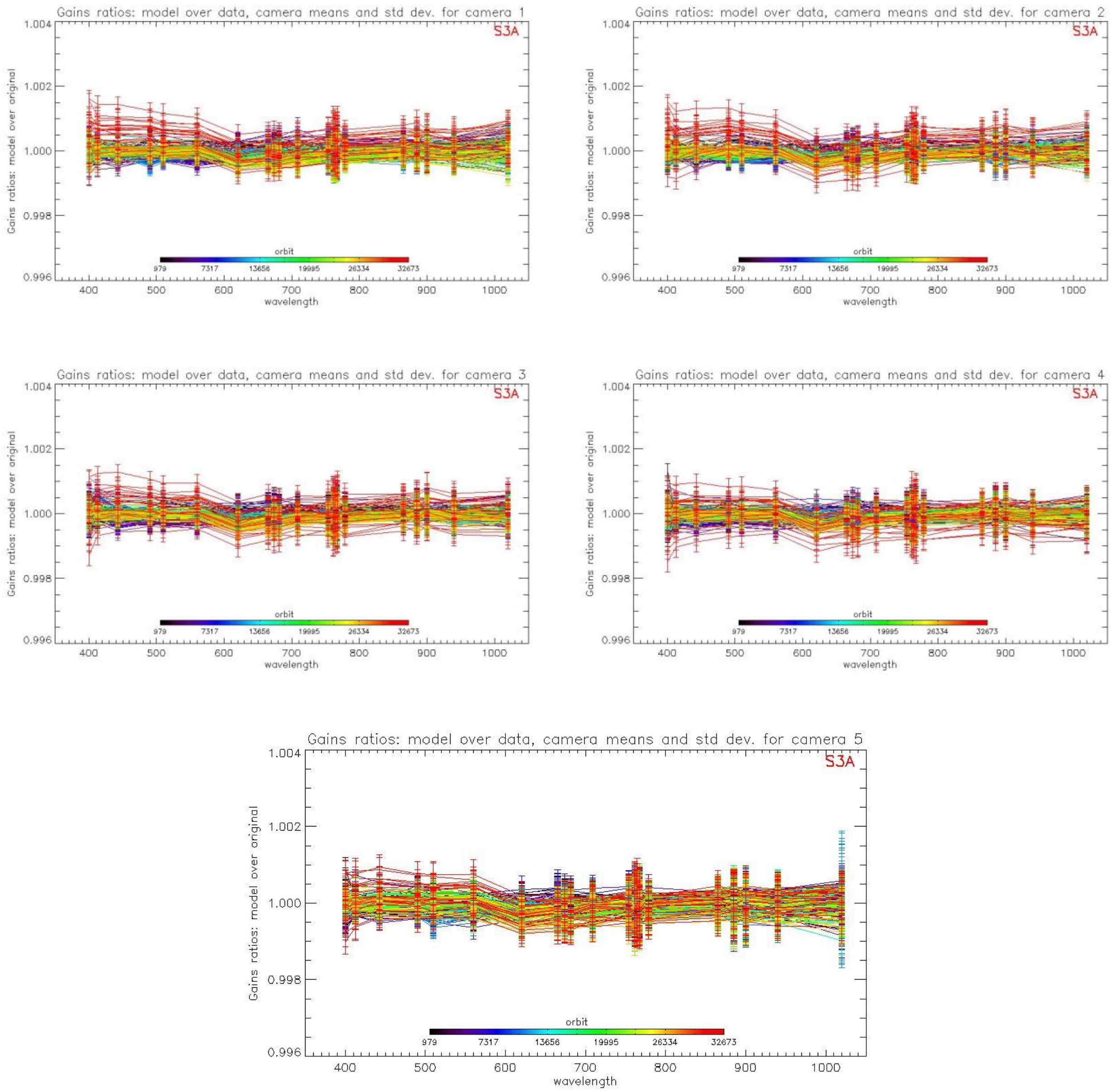

Figure 29: For the 5 cameras: OLCI-A Evolution model performance, as camera-average and standard deviation of ratio of Model over Data vs. wavelength, for each orbit of the test dataset, including 19 calibrations in extrapolation, with a colour code for each calibration from blue (oldest) to red (most recent).

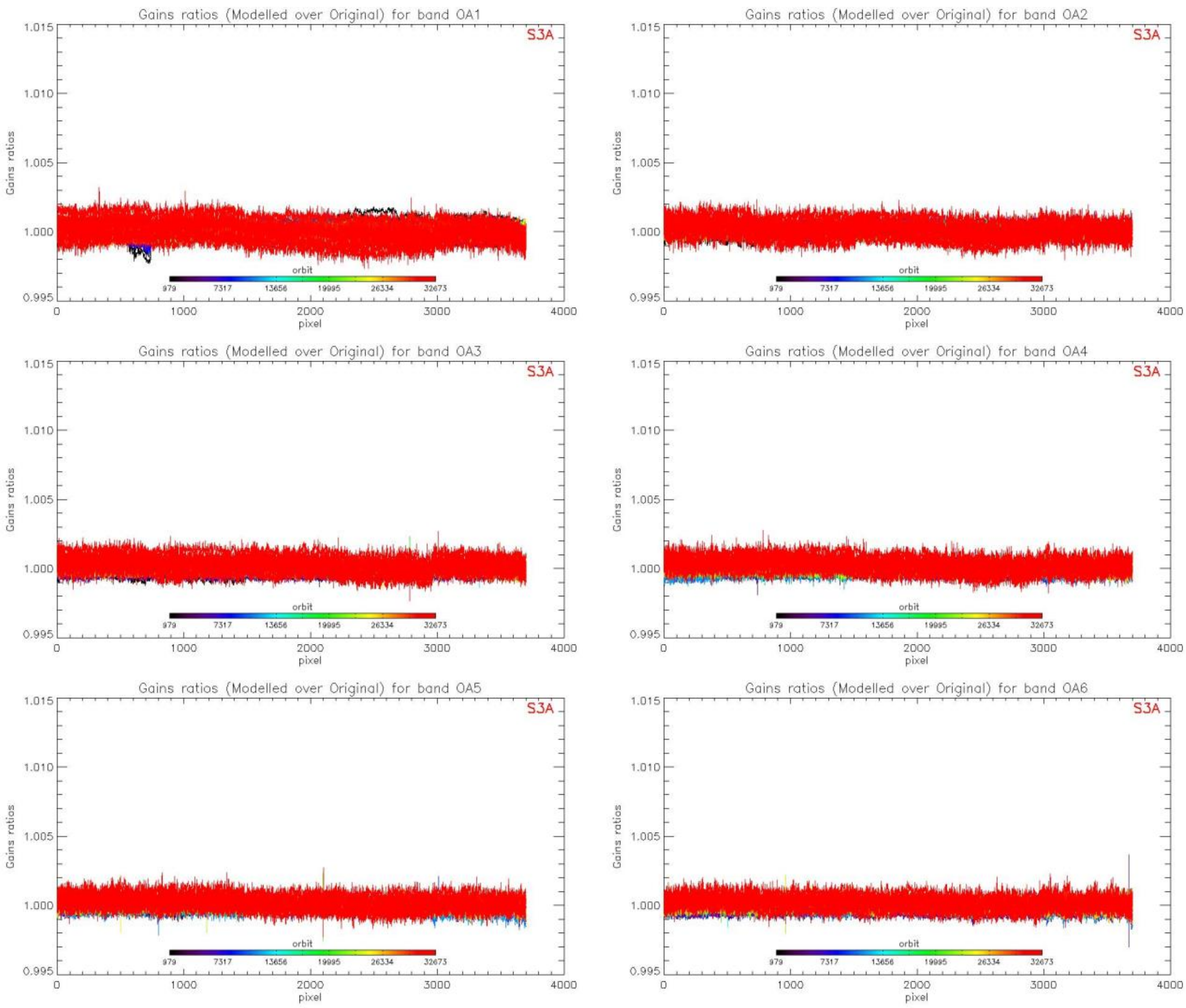

Figure 30: OLCI-A evolution model performance, as ratio of Model over Data vs. pixels, all cameras side by side, over the whole current calibration dataset (since instrument programing update), including 19 calibrations in extrapolation, channels Oa1 to Oa6.

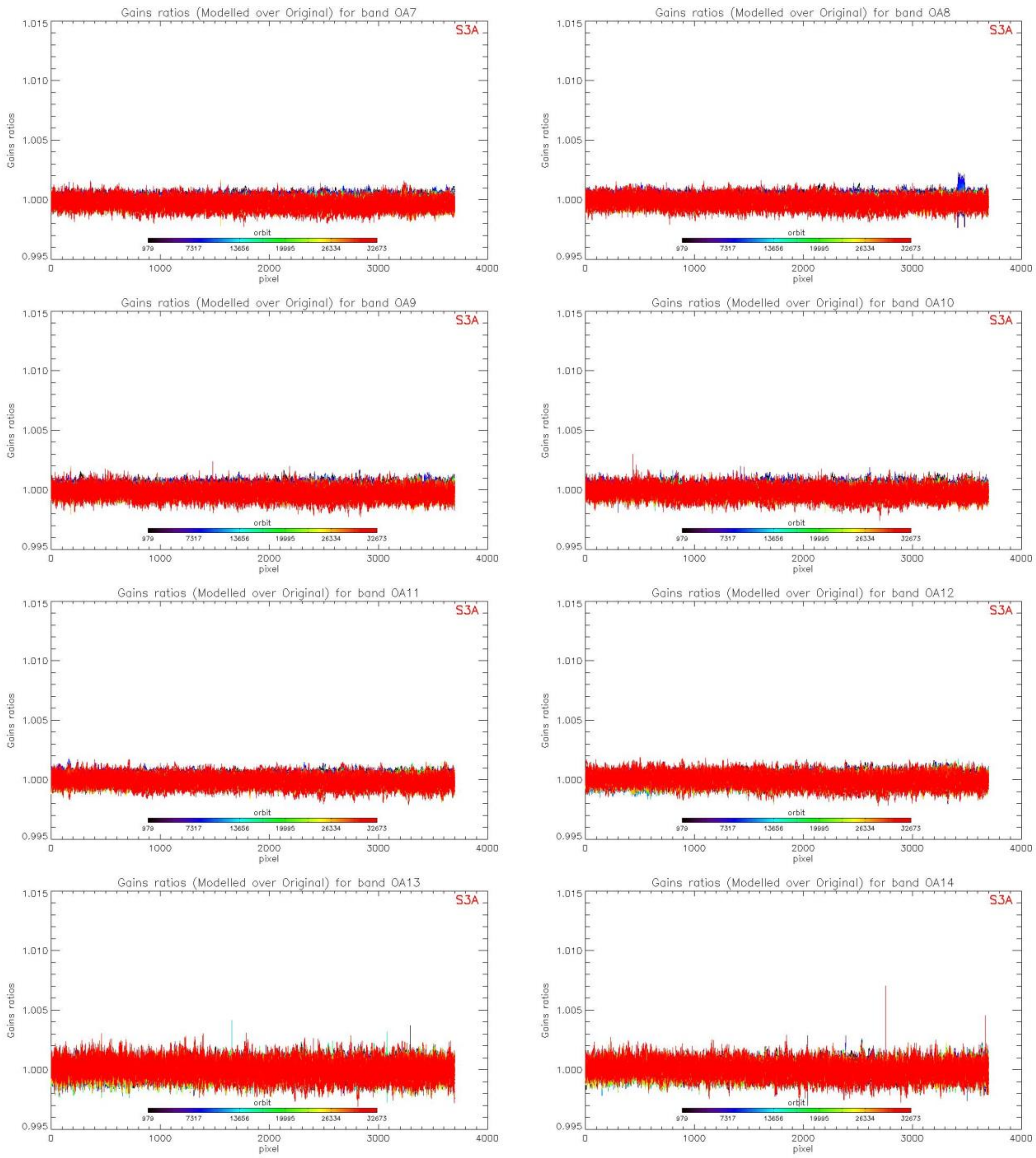

Figure 31: same as Figure 30 for channels Oa7 to Oa14.

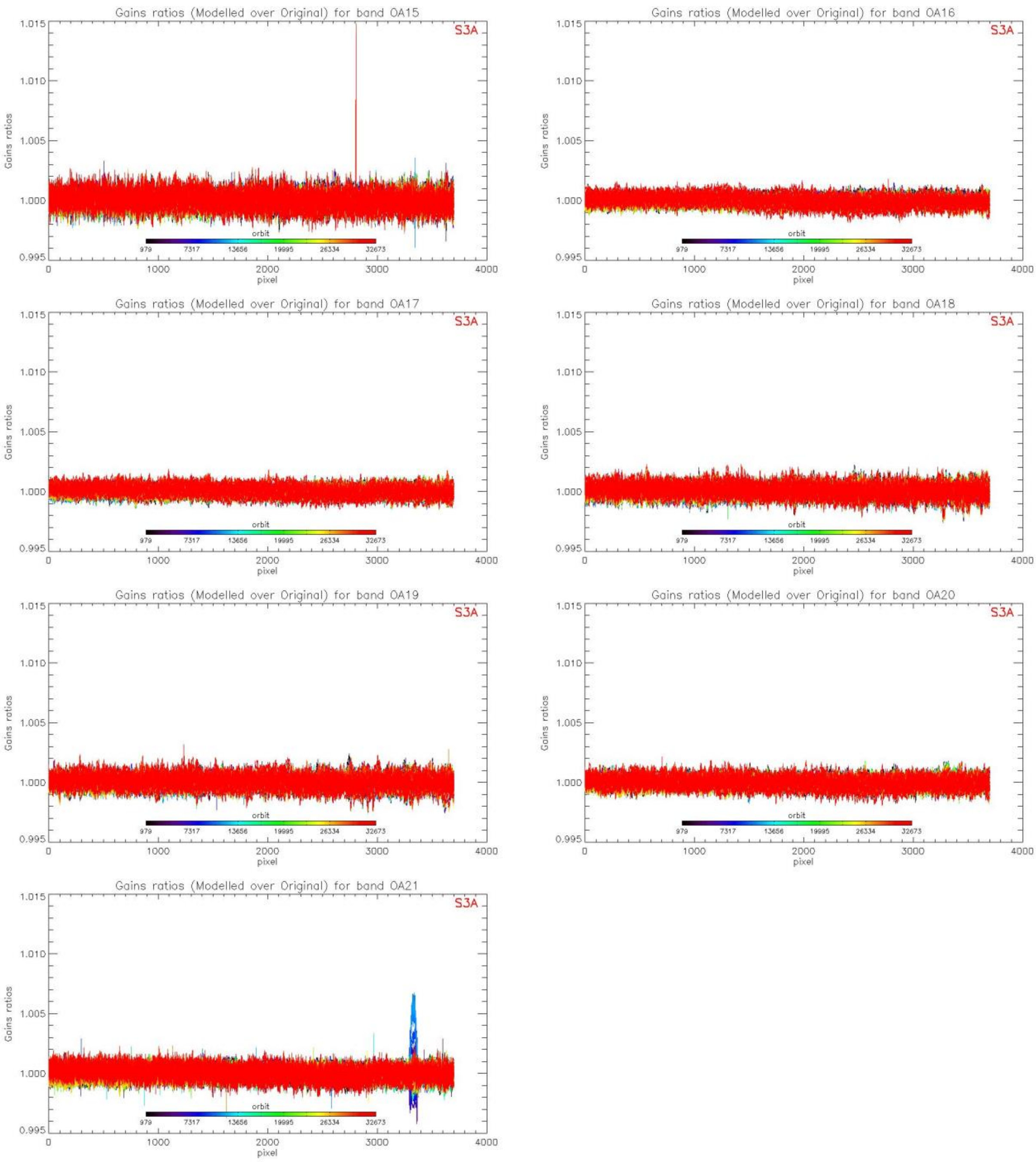

Figure 32: same as Figure 30 for channels Oa15 to Oa21.

2.2.2.2.2 OLCI-B

The current instrument response and degradation modelling for OLCI-B, including the use of the in-flight BRDF model (based on 11th December 2018 Yaw Manoeuvres), has been deployed at PDGS on 18/11/2021 (Processing Baseline 3.01). This model has been derived on the basis of an extended Radiometric Calibration dataset (from 18/06/2019 to 16/09/2021), and most of all a revised Ageing model. It includes the correction of the diffuser ageing for the five bluest bands (Oa1 to Oa5) for which it is clearly measurable. The model performance over the complete dataset (including 20 calibrations in extrapolation over about 8.5 months) is illustrated in Figure 33. It remains better than 0.11% when averaged over the whole field of view for all bands, at the exception of an isolated peak which is present in recent data near orbit 19000 where performance degrades for all bands, up to about 0.15 % for band Oa01. This peak is present in Gain measurements, thus reflects in model performance. The same behaviour is seen on OLCI-A (see Figure 26), suggesting that it is not linked to the instrument sensitivity. A small drift of the model with respect to the most recent data is now visible for all bands. The previous model, trained on a Radiometric Dataset limited to 09/08/2020, shows clearly a more pronounced drift of the model with respect to most recent data, especially for band Oa01 (Figure 34). Comparison of the two figures shows the improvement brought by the updated Model over all the mission.

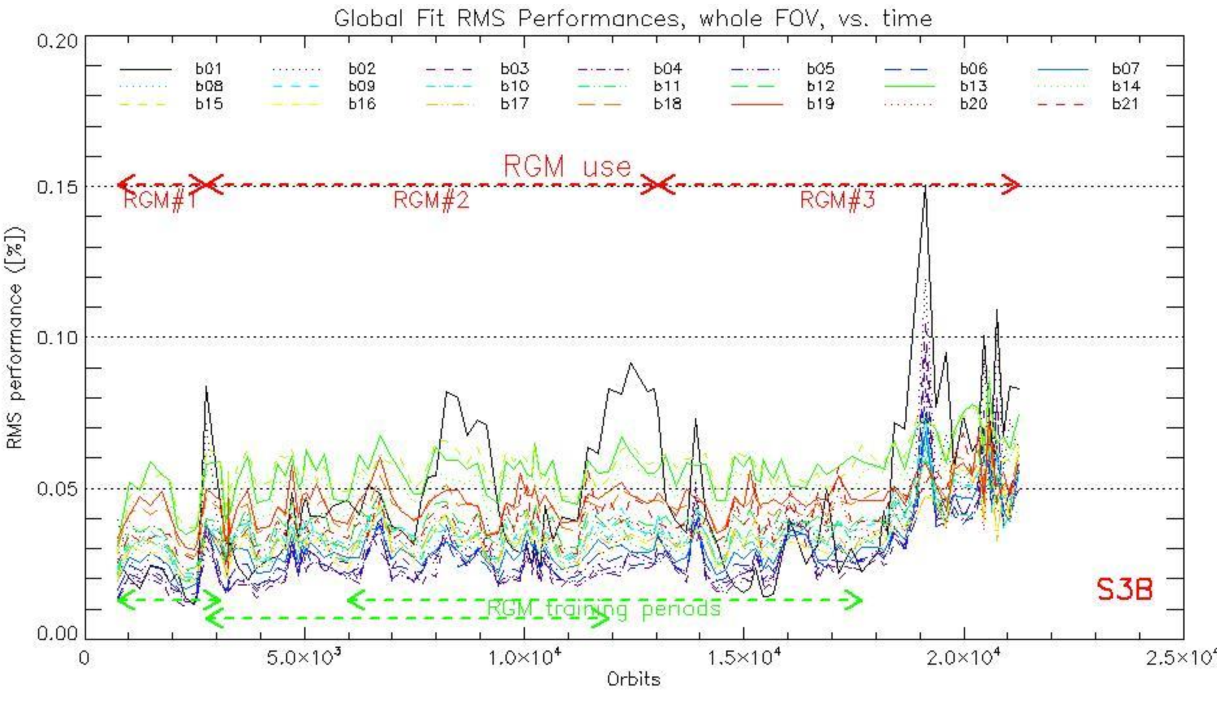

Figure 33: RMS performance of the OLCI-B Gain Model of the current processing baseline as a function of orbit.

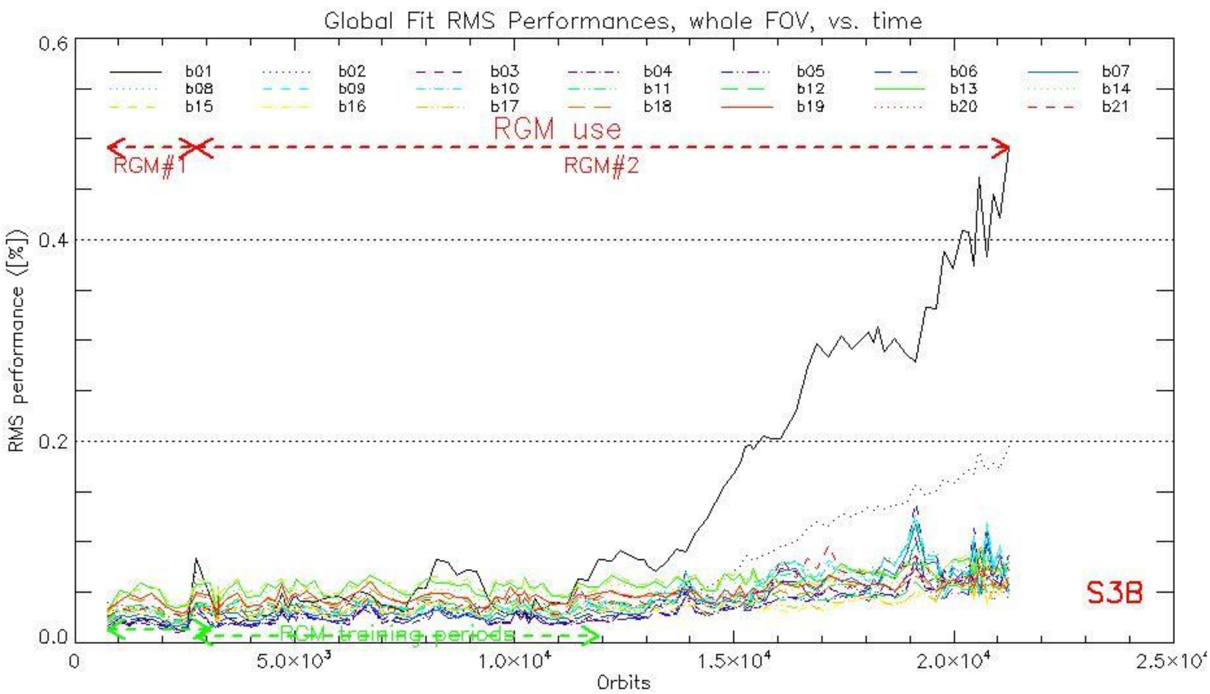

Figure 34: RMS performance of the OLCI-B Gain Model of the previous processing baseline as a function of orbit (please note the different vertical scale with respect to Figure 33).

The overall instrument evolution since channel programming change (18/06/2018) is shown on Figure 35.

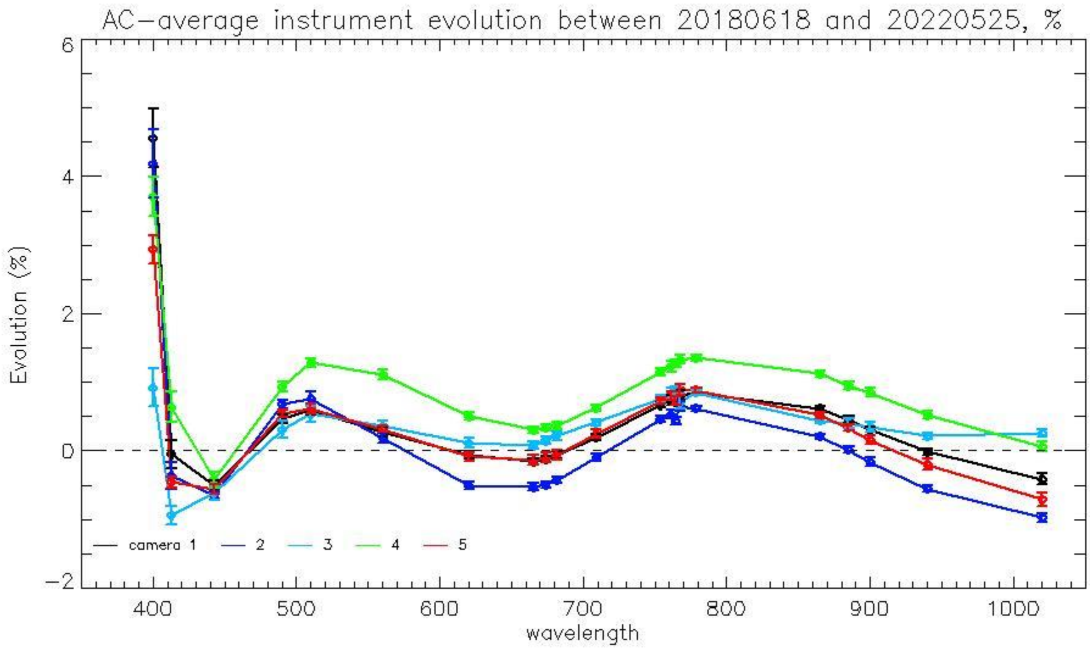

Figure 35: OLCI-B Camera-averaged instrument evolution since channel programming change (18/06/2018) and up to most recent calibration (25/05/2022) versus wavelength.

The overall per camera performance, as a function of wavelength, and at each orbit is shown on Figure 36 as the average and standard deviation of the model over data ratio.

Finally, Figure 37 to Figure 39 show the detail of the model performance, with across-track plots of the model over data ratios at each orbit, one plot for each channel.

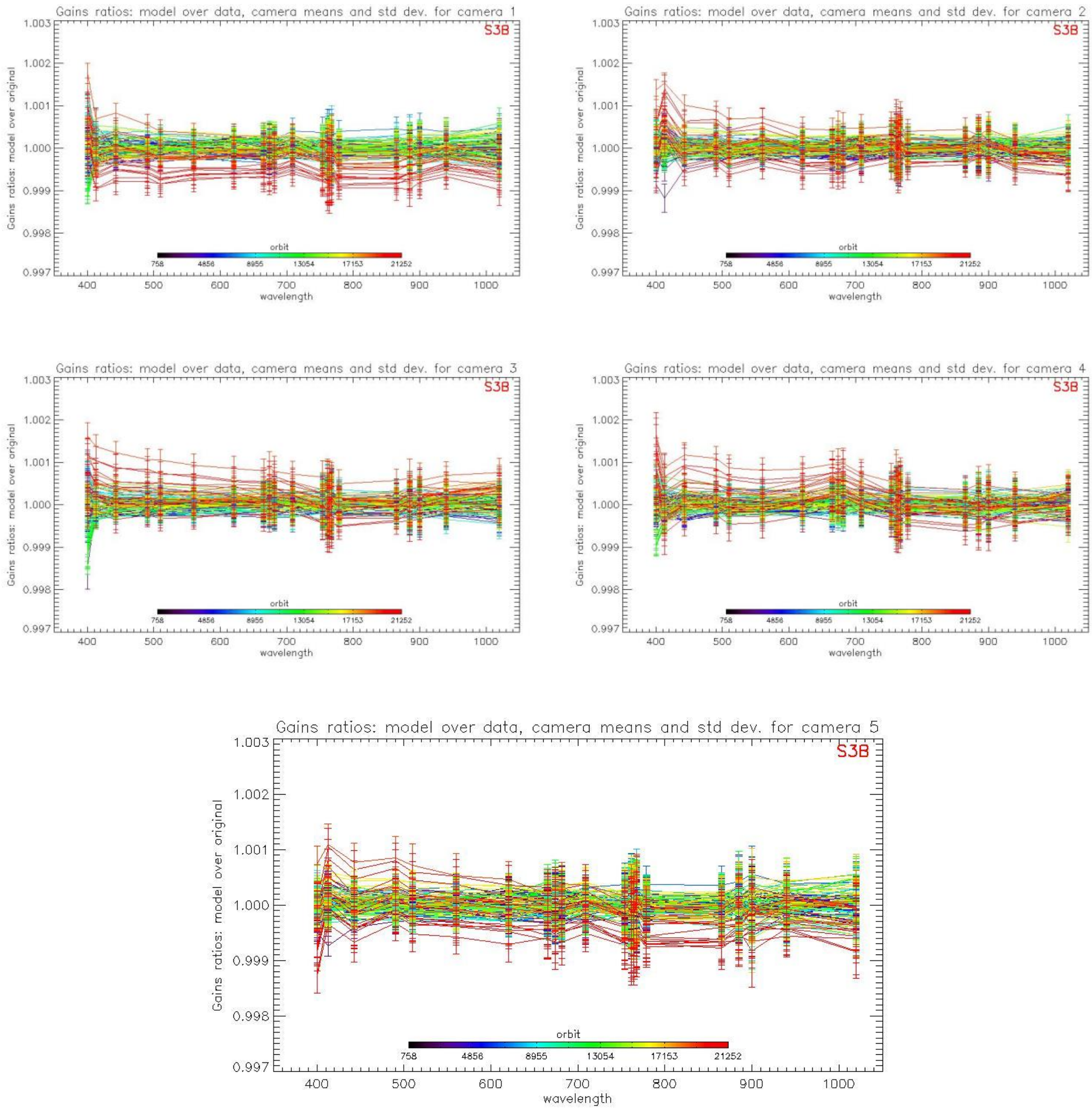

Figure 36: For the 5 cameras: OLCI-B Evolution model performance, as camera-average and standard deviation of ratio of Model over Data vs. wavelength, for each orbit of the test dataset, including 20 calibrations in extrapolation, with a colour code for each calibration from blue (oldest) to red (most recent).

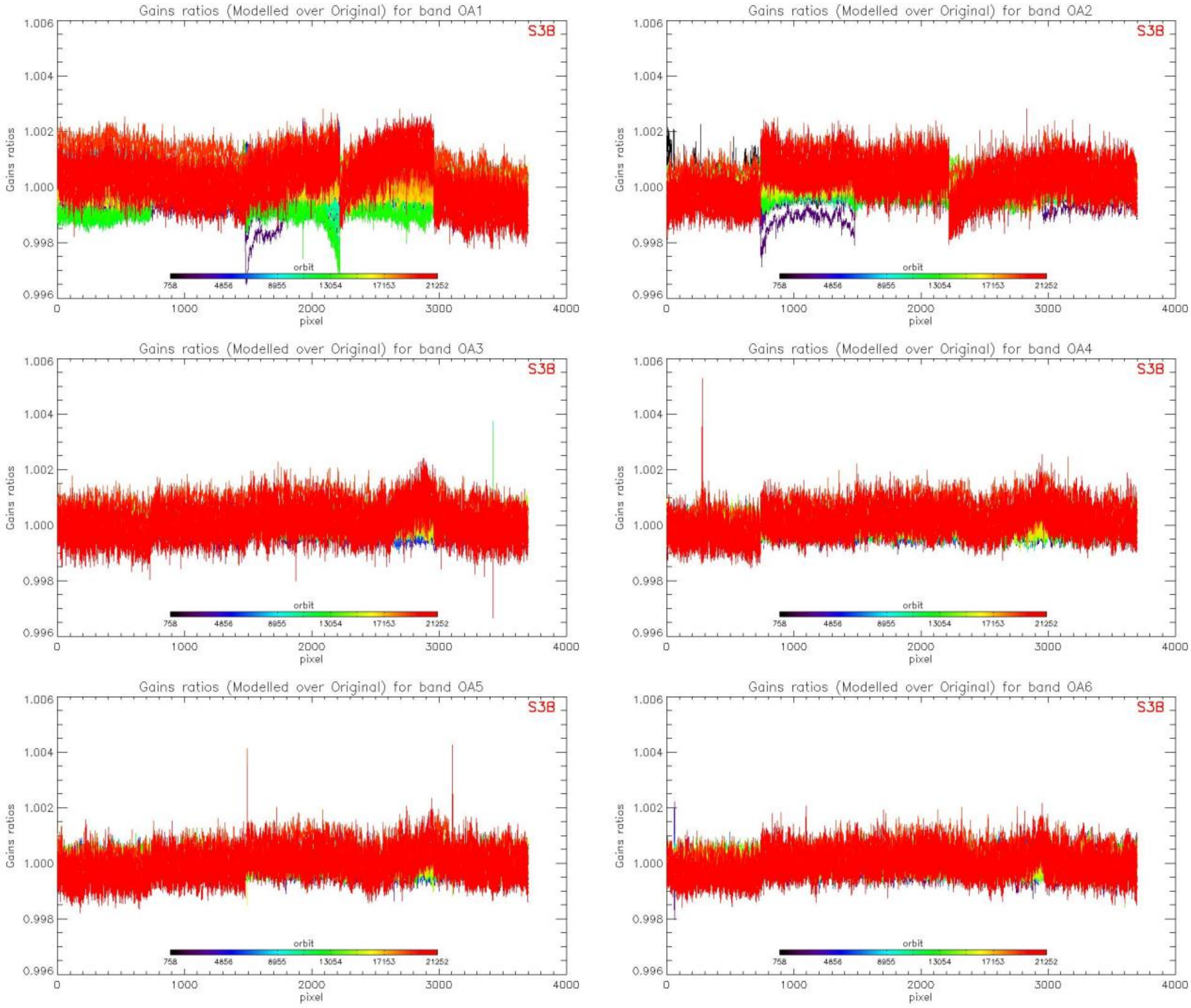

Figure 37: OLCI-B evolution model performance, as ratio of Model over Data vs. pixels, all cameras side by side, over the whole current calibration dataset (since instrument programming update), including 20 calibrations in extrapolation, channels Oa1 to Oa6.

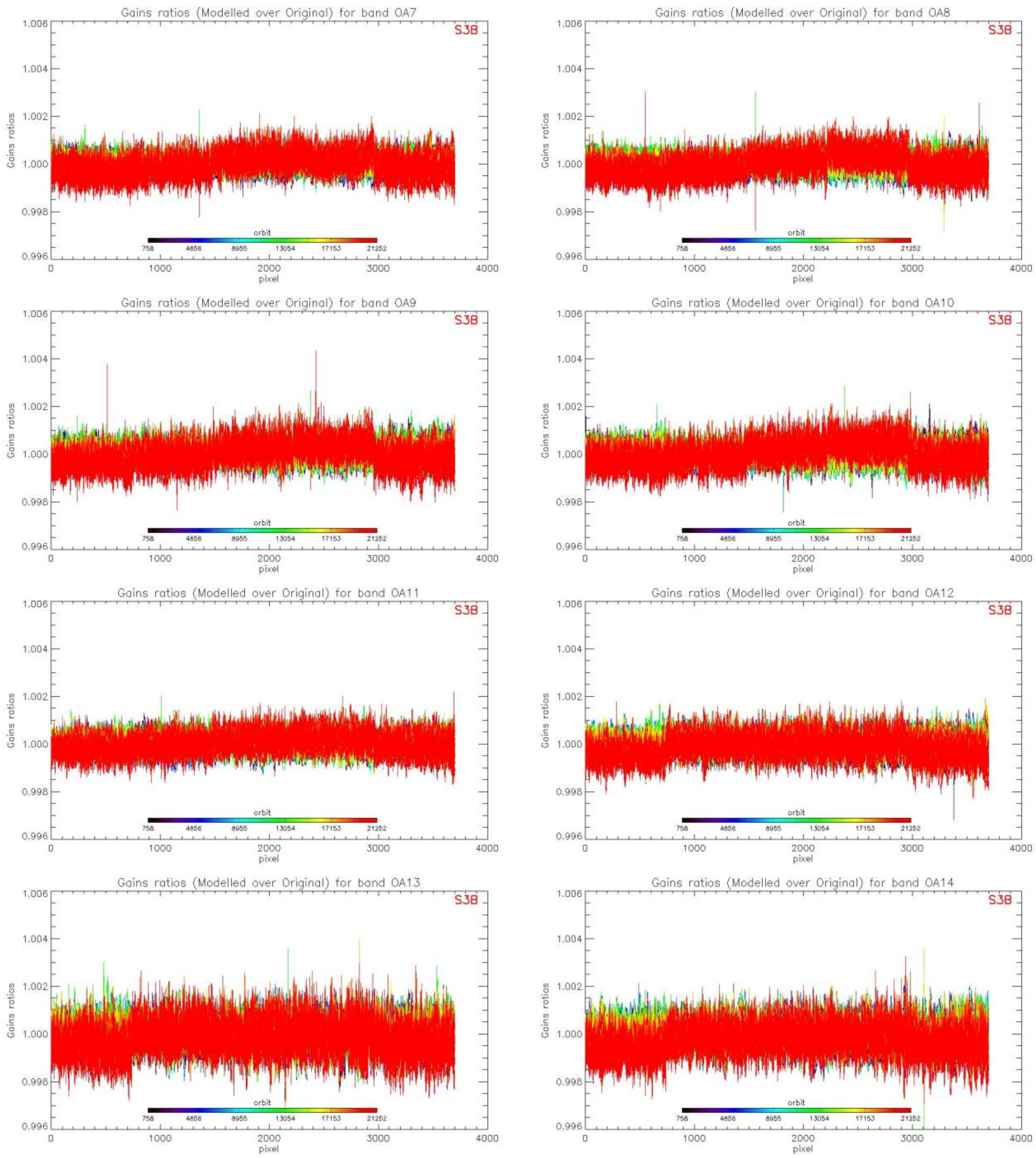

Figure 38: same as Figure 37 for channels Oa7 to Oa14.

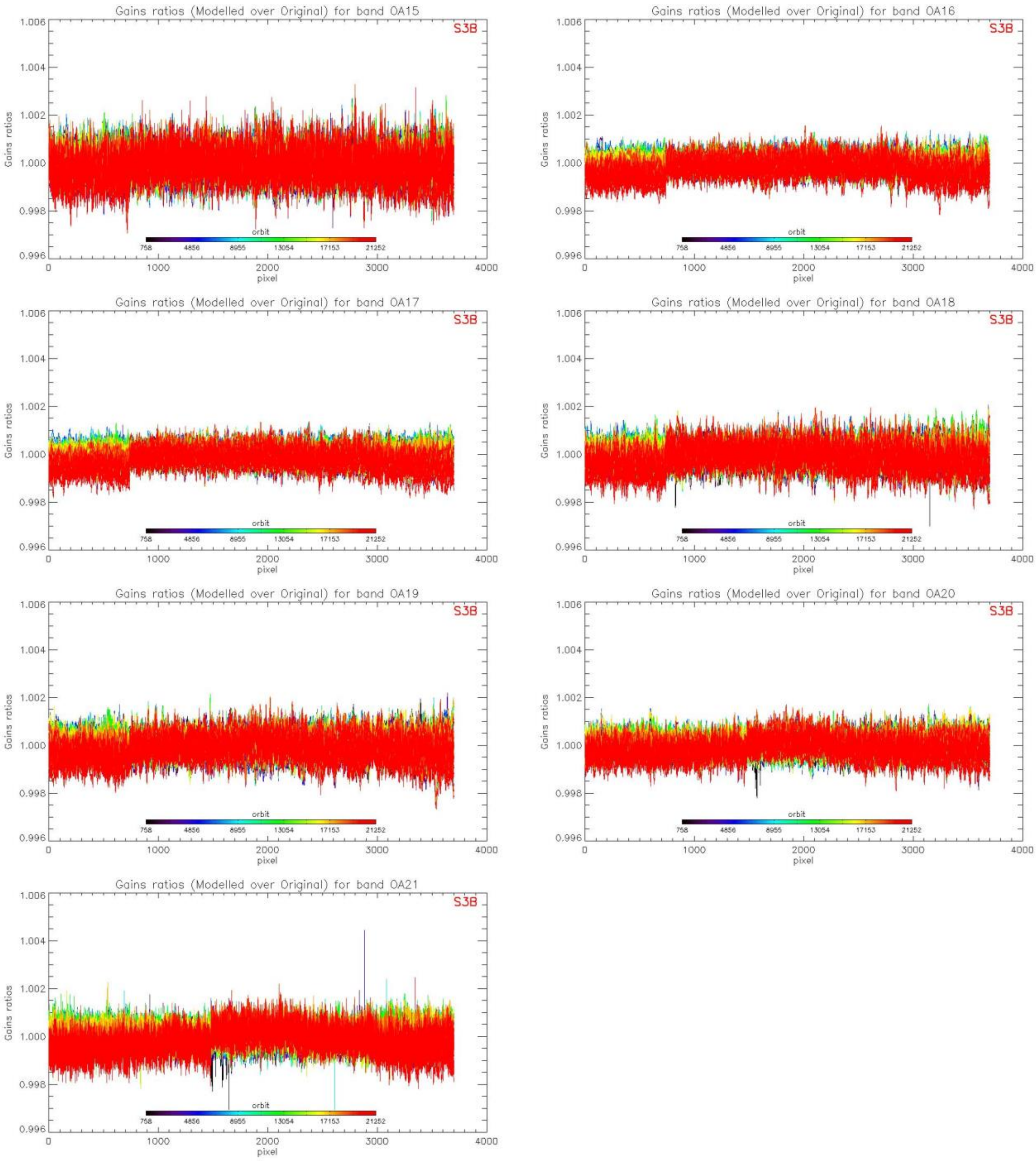

Figure 39: same as for channels Oa15 to Oa21.

2.2.3 Ageing of nominal diffuser [OLCI-L1B-CV-240]

2.2.3.1 OLCI-A

There has been no calibration sequence S05 (reference diffuser) for OLCI-A during the current reported period.

Consequently, the last ageing results, presented in March 2022 DQR, remain valid.

2.2.3.2 OLCI-B

There has been no calibration sequence S05 (reference diffuser) for OLCI-B during the current reported period.

Consequently, the last ageing results, presented in March 2022 DQR, remain valid.

2.2.4 Updating of calibration ADF [OLCI-L1B-CV-260]

2.2.4.1.1 OLCI-A

One CAL_AX ADF has been delivered during the report period for OLCI-A:

S3A_OL_1_CAL_AX_20211027T000000_20991231T235959_20220505T120000________________MPC_O_AL_026.SEN3

It contains updated Radiometric Gain Model coefficients.

2.2.4.1.2 OLCI-B

One CAL_AX ADF has been delivered during the report period for OLCI-B:

S3B_OL_1_CAL_AX_20211027T000000_20991231T235959_20220505T120000________________MPC_O_AL_016.SEN3

It contains updated Radiometric Gain Model coefficients.

2.3 Spectral Calibration [OLCI-L1B-CV-400]

2.3.1 OLCI-A

There has been no S02+S03 Spectral Calibration for OLCI-A in the reporting period.

Consequently, the last Spectral Calibration results, presented in February 2022 DQR, remain valid.

2.3.2 OLCI-B

There has been no S02+S03 Spectral Calibration for OLCI-B in the reporting period.

Consequently, the last Spectral Calibration results, presented in February 2022 DQR, remain valid.

2.4 Signal to Noise assessment [OLCI-L1B-CV-620]

2.4.1 SNR from Radiometric calibration data

2.4.1.1 OLCI-A

SNR computed for all calibration data (S01, S04 and S05 sequences) as a function of band number is presented in Figure 40.

SNR computed for all calibration data as a function of orbit number for band Oa01 (the less stable band) is presented in Figure 41.

There is no significant evolution of this parameter during the current reporting period and the ESA requirement is fulfilled for all bands.

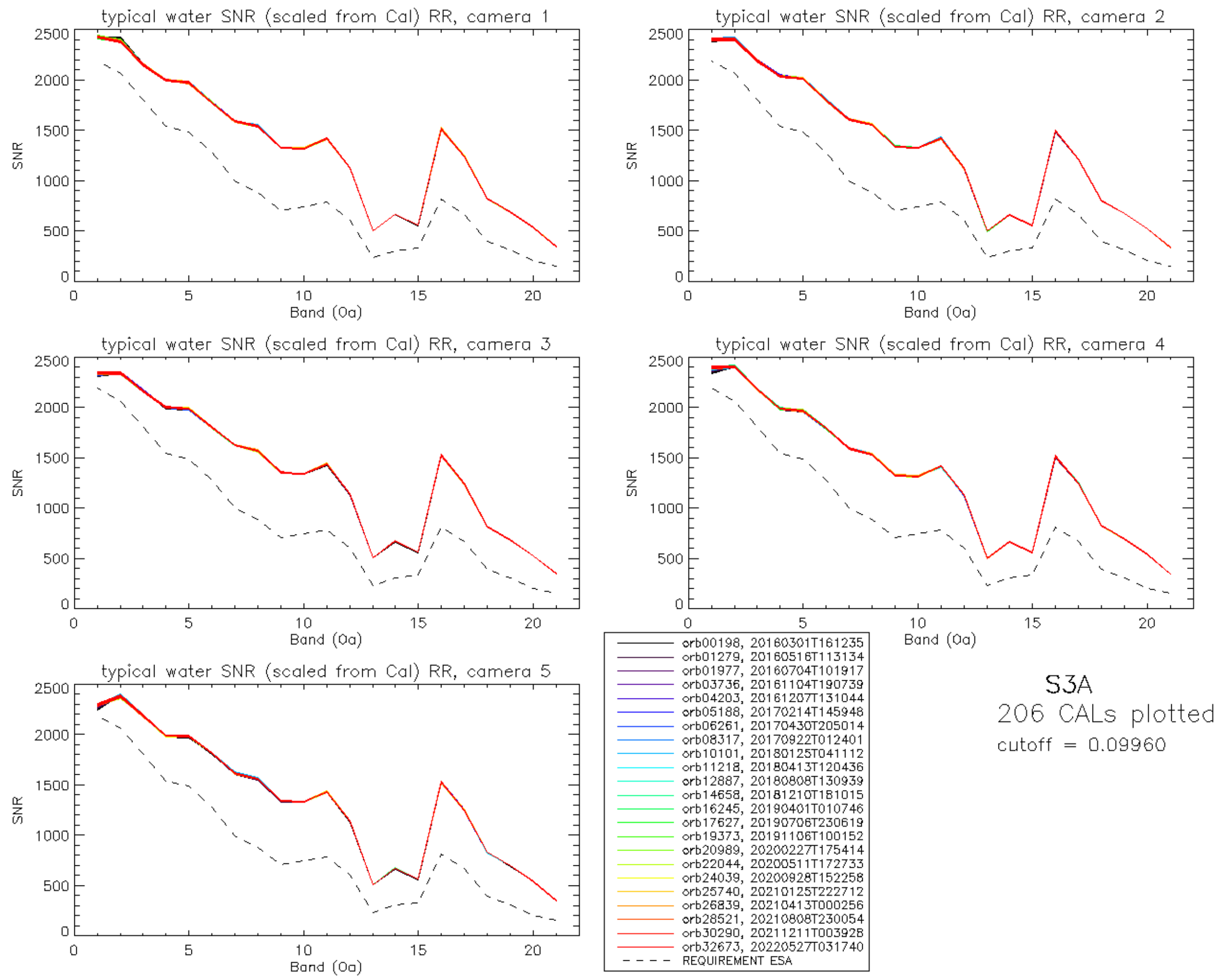

Figure 40: OLCI-A Signal to Noise ratio as a function of the spectral band for the 5 cameras. These results have been computed from radiometric calibration data. All calibrations except first one (orbit 183) are presents with

the colours corresponding to the orbit number (see legend). The SNR is very stable with time: the curves for all orbits are almost superimposed. The dashed curve is the ESA requirement.

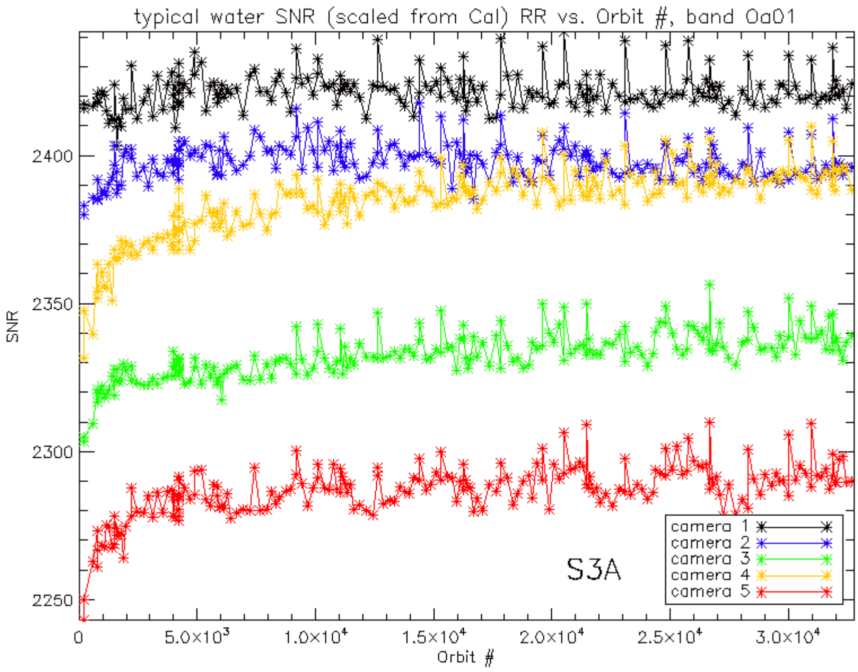

Figure 41: long-term stability of the SNR estimates from Calibration data, example of channel Oa1.

The mission averaged SNR figures are provided in Table 1 below, together with their radiance reference level. According to the OLCI SNR requirements, these figures are valid at these radiance levels and at Reduced Resolution (RR, 1.2 km). They can be scaled to other radiance levels assuming shot noise (CCD sensor noise) is the dominating term, i.e. radiometric noise can be considered Gaussian with its standard deviation varying as the square root of the signal; in other words: $SNR(L) = SNR(L_{ref}) \cdot \sqrt{\frac{L}{L_{ref}}}$. Following the same assumption, values at Full Resolution (300m) can be derived from RR ones as 4 times smaller.

Table 1: OLCI-A SNR figures as derived from Radiometric Calibration data. Figures are given for each camera (time average and standard deviation), and for the whole instrument. The requirement and its reference radiance level are recalled (in mW.sr^{-1}.m^{-2}.nm^{-1}).

	L_{ref}	SNR	C1		C2		C3		C4		C5		All	
nm	LU	RQT	avg	*std*	avg	*std*	avg	*std*	avg	*std*	avg	*std*	avg	*std*
400.000	63.0	2188	2421	6.1	2398	6.2	2332	7.9	2384	11.9	2286	9.1	2364	6.9
412.000	74.1	2061	2387	9.4	2403	7.0	2339	5.0	2401	5.0	2380	9.0	2382	5.6
442.000	65.6	1811	2158	6.0	2196	6.0	2163	4.9	2185	4.1	2193	5.8	2179	4.1
490.000	51.2	1541	1999	4.6	2036	4.8	1998	4.2	1984	4.4	1988	4.4	2001	3.2
510.000	44.4	1488	1979	5.3	2014	4.9	1986	4.5	1967	4.4	1985	4.2	1986	3.4
560.000	31.5	1280	1775	4.5	1802	4.1	1803	4.6	1794	3.8	1818	3.3	1799	3.0
620.000	21.1	997	1591	4.0	1608	4.3	1624	3.1	1593	3.3	1615	3.5	1606	2.6
665.000	16.4	883	1546	4.2	1557	4.5	1566	3.9	1533	3.6	1561	3.7	1553	3.0
674.000	15.7	707	1328	3.4	1337	3.7	1350	2.8	1323	3.2	1343	3.4	1336	2.4
681.000	15.1	745	1319	3.6	1325	3.3	1338	2.6	1314	2.5	1334	3.4	1326	2.2
709.000	12.7	785	1420	4.2	1420	4.0	1435	3.3	1414	3.5	1431	3.1	1424	2.7
754.000	10.3	605	1127	3.1	1121	2.8	1136	3.1	1125	2.5	1139	2.7	1130	2.2
761.000	6.1	232	502	1.1	498	1.1	505	1.1	501	1.1	508	1.3	503	0.8
764.000	7.1	305	663	1.6	658	1.5	668	2.0	662	1.5	670	2.0	664	1.3
768.000	7.6	330	558	1.4	554	1.3	563	1.3	557	1.3	564	1.3	559	1.0
779.000	9.2	812	1516	4.7	1498	4.5	1526	5.1	1512	4.9	1527	4.8	1516	4.0
865.000	6.2	666	1243	3.5	1213	3.4	1239	3.8	1246	3.5	1250	2.8	1238	2.8
885.000	6.0	395	823	1.7	801	1.6	814	1.9	824	1.5	831	1.6	819	1.1
900.000	4.7	308	691	1.6	673	1.3	683	1.6	693	1.5	698	1.5	688	1.0
940.000	2.4	203	534	1.2	522	1.2	525	0.9	539	1.1	542	1.3	532	0.7
1020.000	3.9	152	345	0.9	337	0.8	348	0.7	345	0.8	351	0.8	345	0.5

2.4.1.2 OLCI-B

SNR computed for all OLCI-B calibration data (S01, S04 (but not the dark-only S04) and S05 sequences) as a function of band number is presented in Figure 42.

SNR computed for all OLCI-B calibration data as a function of orbit number for band Oa01 (the less stable band) is presented in Figure 43.

As for OLCI-A the SNR is very stable in time. There is no significant evolution of this parameter during the current reporting and the ESA requirement is fulfilled for all bands.

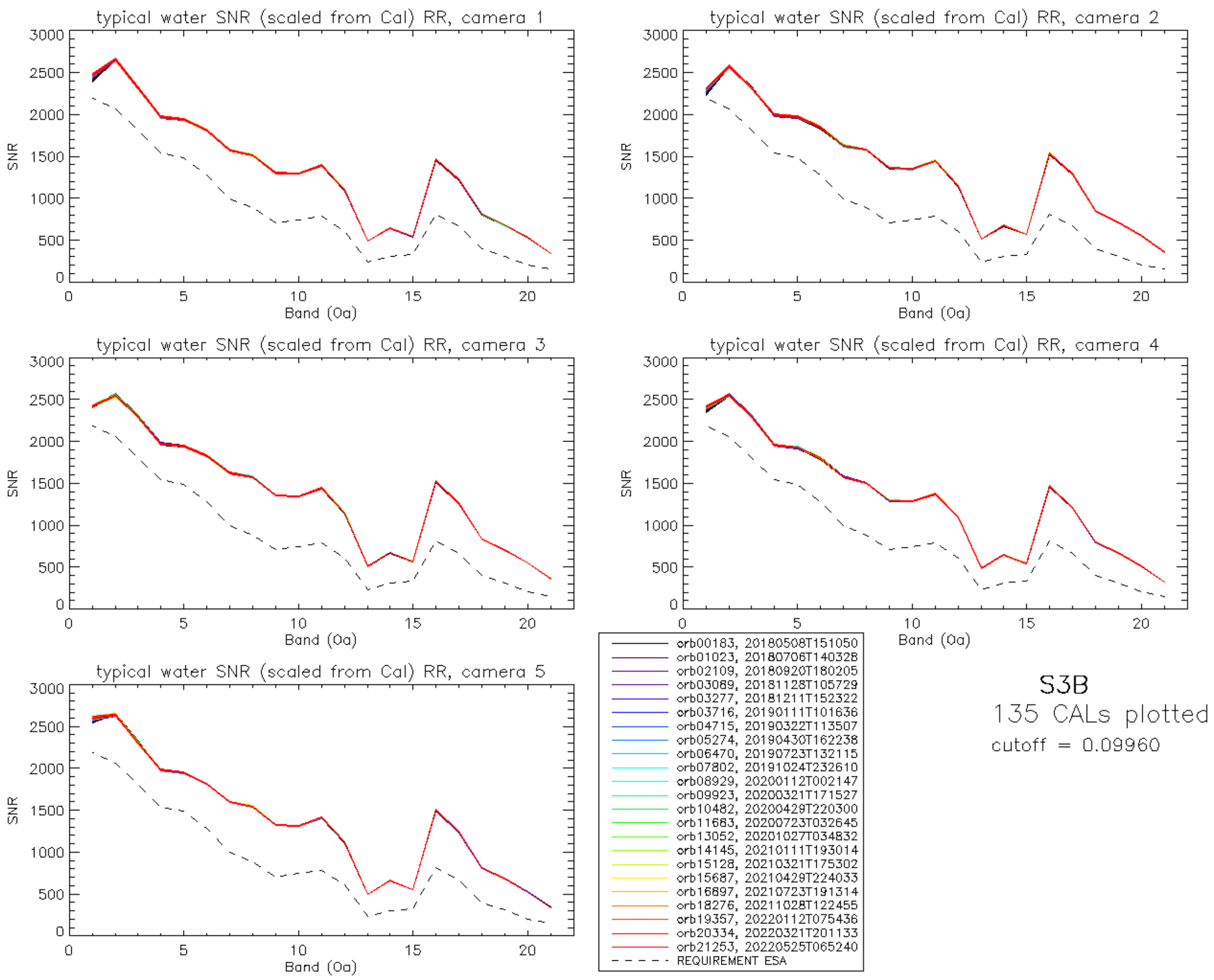

Figure 42: OLCI-B Signal to Noise ratio as a function of the spectral band for the 5 cameras. These results have been computed from radiometric calibration data. All calibrations except first one (orbit 167) are presents with the colours corresponding to the orbit number (see legend). The SNR is very stable with time: the curves for all orbits are almost superimposed. The dashed curve is the ESA requirement.

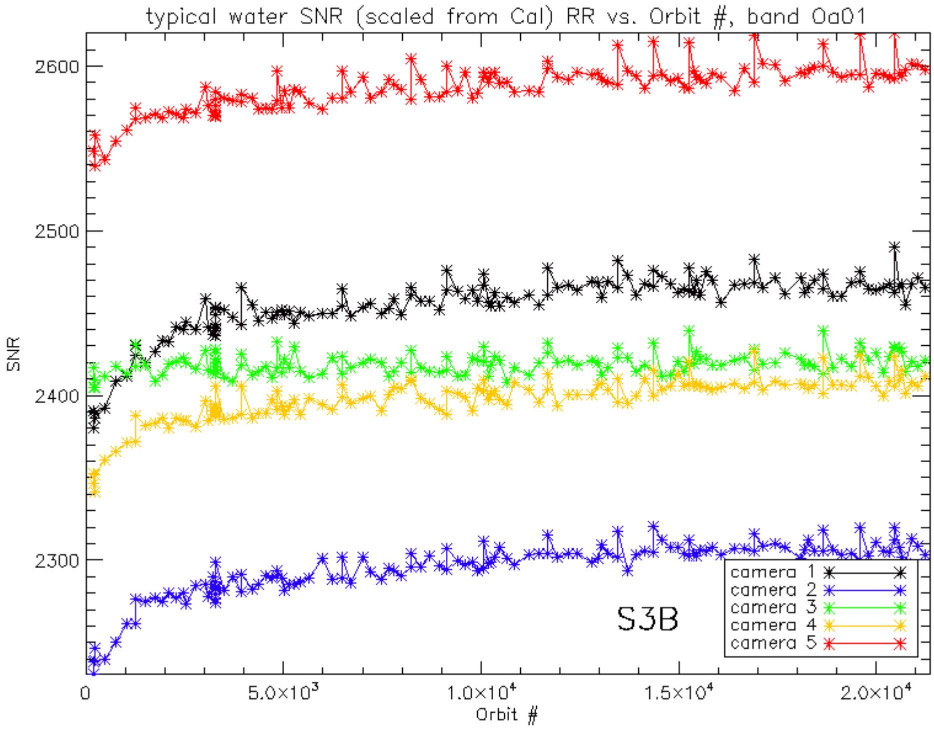

Figure 43: long-term stability of the OLCI-B SNR estimates from Calibration data, example of channel Oa1.

Table 2: OLCI-B SNR figures as derived from Radiometric Calibration data. Figures are given for each camera (time average and standard deviation), and for the whole instrument. The requirement and its reference radiance level are recalled (in mW.sr^{-1}.m^{-2}.nm^{-1}).

	L_{ref}	SNR	C1		C2		C3		C4		C5		All	
nm	LU	RQT	avg	*std*	avg	*std*	avg	*std*	avg	*std*	avg	*std*	avg	*std*
400.000	63.0	2188	2454	18.9	2294	16.8	2419	6.3	2397	13.9	2586	14.2	2430	13.0
412.000	74.1	2061	2655	6.8	2569	6.3	2544	8.2	2550	6.1	2638	7.3	2591	5.3
442.000	65.6	1811	2324	6.6	2316	5.9	2300	6.4	2303	6.7	2308	6.4	2310	5.4
490.000	51.2	1541	1966	4.8	1989	5.7	1971	5.1	1952	4.6	1979	4.6	1972	3.8
510.000	44.4	1488	1939	4.8	1968	5.9	1943	4.9	1924	5.0	1951	4.8	1945	4.0
560.000	31.5	1280	1813	4.8	1848	5.0	1829	4.6	1804	4.8	1817	4.0	1822	3.6
620.000	21.1	997	1572	4.3	1626	4.6	1624	3.7	1576	3.7	1601	3.4	1600	2.9
665.000	16.4	883	1513	4.2	1579	3.8	1573	3.8	1501	3.0	1546	3.8	1542	2.8
674.000	15.7	707	1301	3.8	1358	3.5	1353	3.2	1292	2.7	1328	3.0	1326	2.3
681.000	15.1	745	1293	3.5	1347	3.2	1343	2.9	1285	2.7	1316	3.0	1317	2.1
709.000	12.7	785	1390	4.0	1447	4.0	1443	4.1	1373	2.9	1412	3.7	1413	3.0
754.000	10.3	605	1096	3.7	1143	3.7	1142	3.4	1089	2.8	1116	3.2	1117	2.9
761.000	6.1	232	487	1.2	509	1.2	509	1.4	485	1.2	498	1.4	498	1.0
764.000	7.1	305	643	1.6	672	2.0	672	1.8	641	1.8	658	1.9	657	1.5
768.000	7.6	330	541	1.4	568	1.5	564	1.3	541	1.4	555	1.6	554	1.1
779.000	9.2	812	1467	4.2	1535	4.7	1527	5.4	1467	4.1	1506	4.3	1501	3.8
865.000	6.2	666	1221	3.6	1287	3.8	1258	3.7	1205	3.6	1238	2.9	1242	2.8
885.000	6.0	395	808	2.3	847	1.8	834	2.0	799	1.7	815	2.1	821	1.5
900.000	4.7	308	679	1.5	714	1.9	704	1.7	670	1.6	683	1.5	690	1.2
940.000	2.4	203	527	1.3	549	1.6	551	1.3	510	1.1	522	1.3	532	0.9
1020.000	3.9	152	336	0.8	358	1.2	358	0.8	318	0.7	338	0.9	342	0.6

2.5 Geometric Calibration/Validation

2.5.1 OLCI-A

OLCI-A georeferencing performance is compliant since the introduction of MPC Geometric Calibration, put in production on the 14th of March 2018. It has however significantly improved after its last full revision of GCMs (Geometric Calibration Models, or platform to instrument alignment quaternions) and IPPVMs (Instrument Pixels Pointing Vectors) both derived using the GeoCal Tool and put in production on 30/07/2019.

The following figures (Figure 44 to Figure 49) show time series of the overall RMS performance (requirement criterion) and of the across-track and along-track biases for each camera. New plots (Figure 50 and Figure 51) introduce monitoring of the performance homogeneity within the field of view: georeferencing errors in each direction at camera transitions (difference between last pixel of camera N and first pixel of camera N+1) and within a given camera (maximum bias minus minimum inside each camera). The performance improvement since the 30/07/2019 is significant on most figures: the global RMS value decreases form around 0.35 to about 0.2 (Figure 44), the across-track biases decrease significantly for all cameras (Figure 45 to Figure 49), the along-track bias reduces for at least camera 3 (Figure 47) and the field of view homogeneity improves drastically (Figure 50 and Figure 51, but also reduction of the dispersion – distance between the ± 1 sigma lines – in Figure 45 to Figure 49).

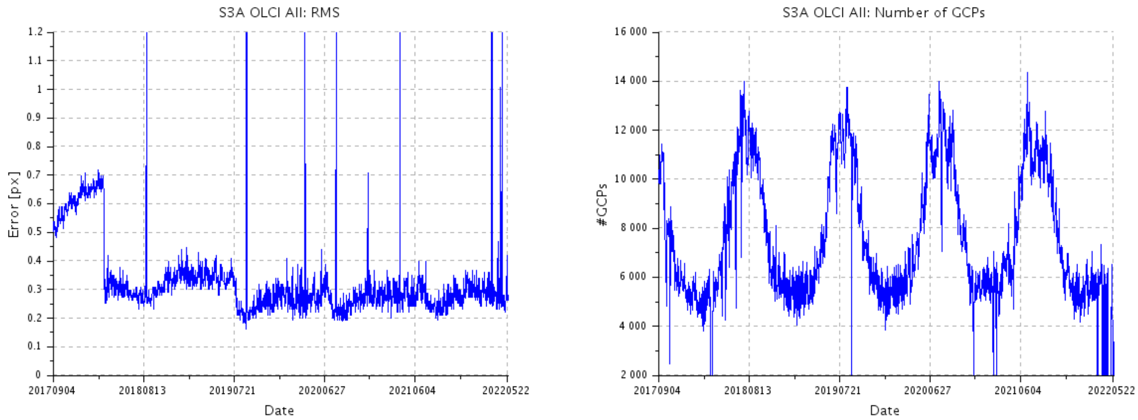

Figure 44: overall OLCI-A georeferencing RMS performance time series (left) and number of validated control points corresponding to the performance time series (right) over the whole monitoring period

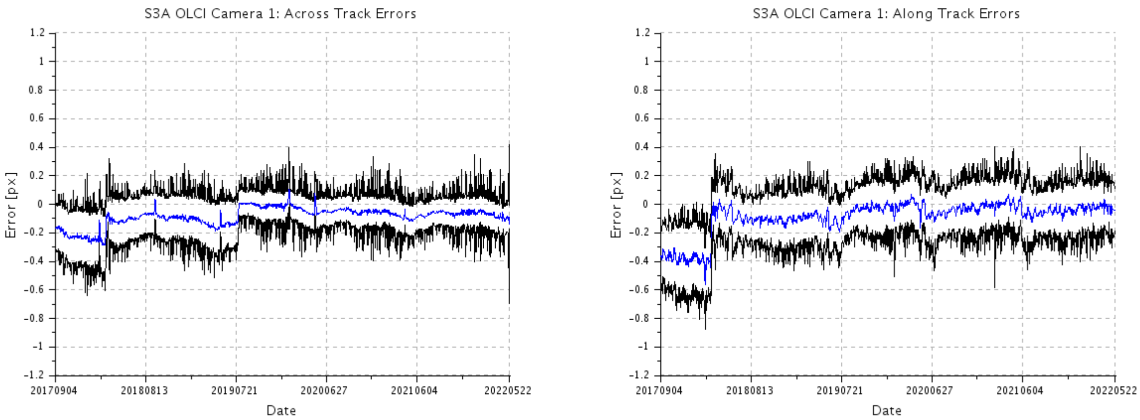

Figure 45: across-track (left) and along-track (right) OLCI-A georeferencing biases time series for Camera 1. Blue line is the average, black lines are average plus and minus 1 sigma.

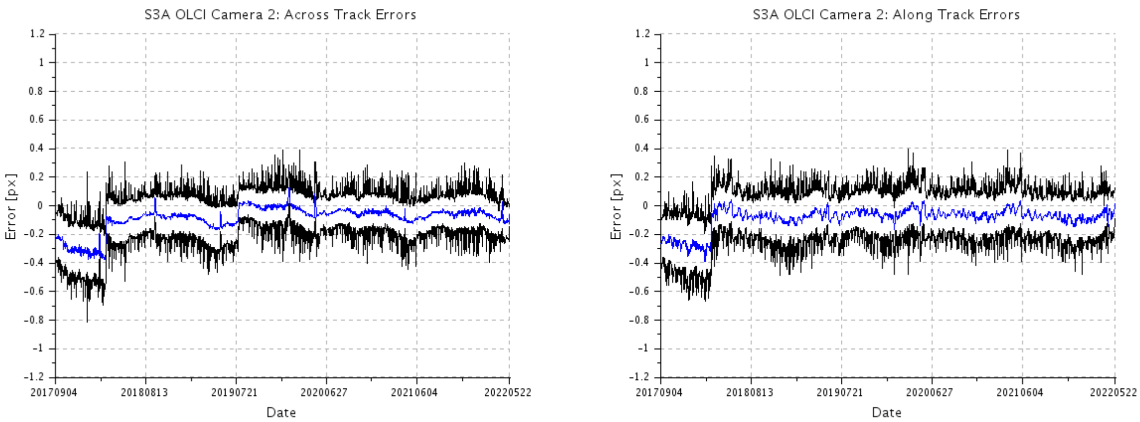

Figure 46: same as Figure 45 for Camera 2.

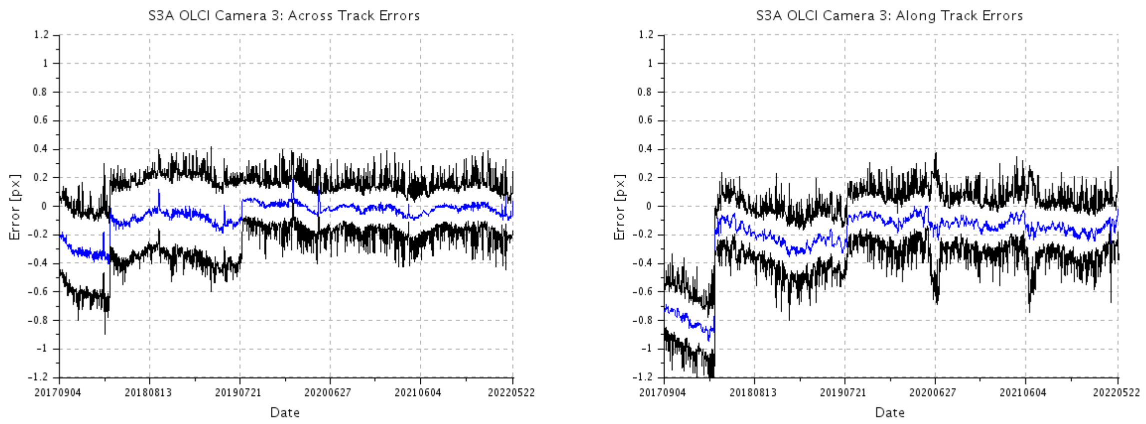

Figure 47: same as Figure 45 for Camera 3.

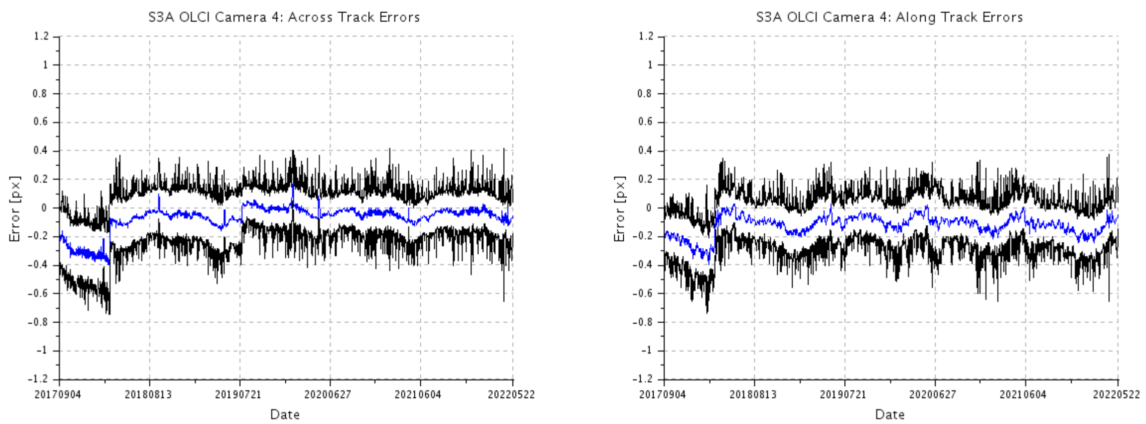

Figure 48: same as Figure 45 for Camera 4.

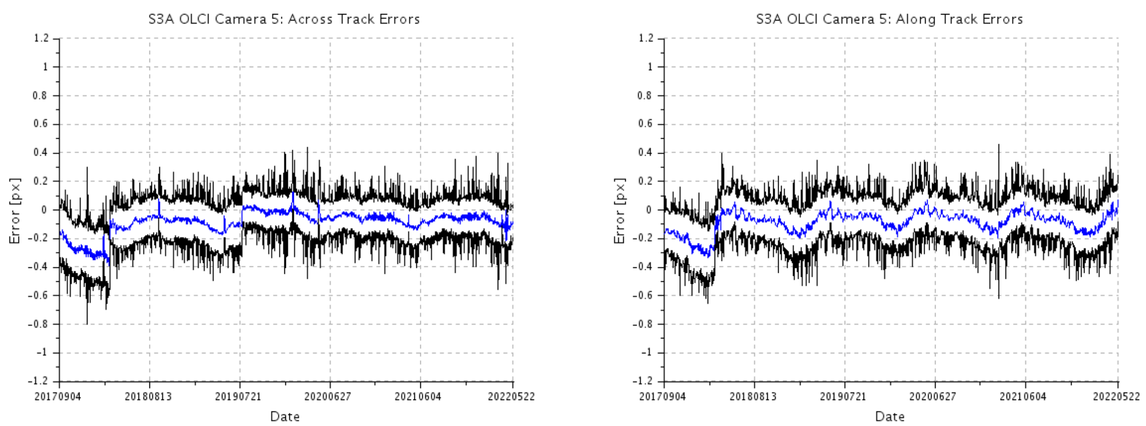

Figure 49: same as Figure 45 for Camera 5.

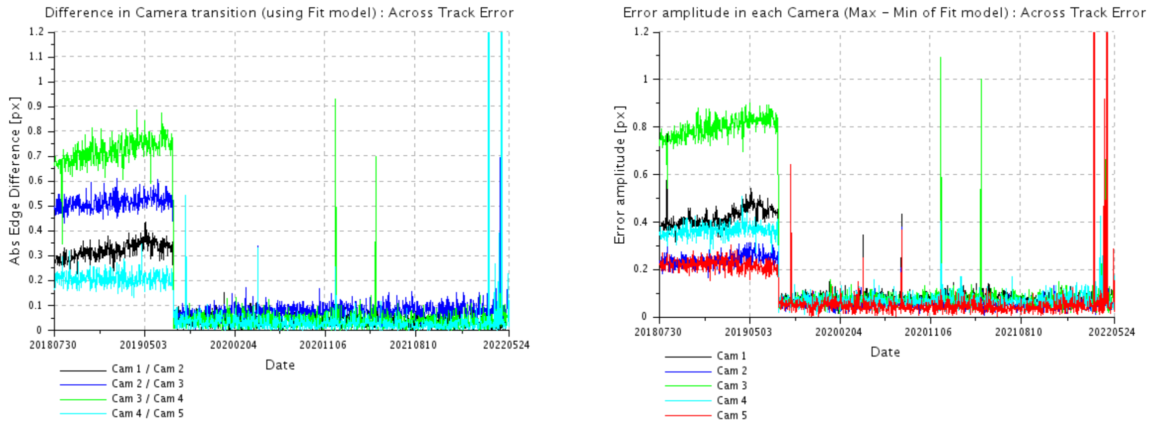

Figure 50: OLCI-A spatial across-track misregistration at each camera transition (left) and maximum amplitude of the across-track error within each camera (left).

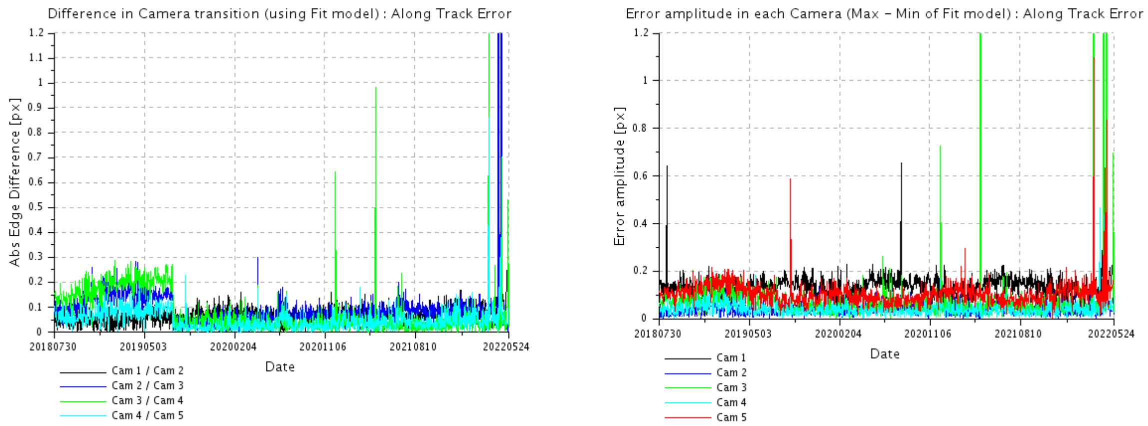

Figure 51: OLCI-A spatial along-track misregistration at each camera transition (left) and maximum amplitude of the along-track error within each camera (left).

2.5.2 OLCI-B

Georeferencing performance of OLCI-B improved significantly with the fourth geometric calibration introduced the 30/07/2019. However, the instrument pointing is still evolving, in particular for camera 2 (Figure 58) and a new geometric calibration has been done and introduced in the processing chain on the 16th of April 2020. Its impact is significant on the along-track biases of all cameras (Figure 53 to Figure 57), but also on the continuity at camera interfaces (Figure 58, left) and on intra-camera homogeneity (Figure 58, right). Since then, further adjustments to the geometric calibration have been introduced, mainly to correct the along-track drifts. The most recent was put in production on 29/07/2021and its effect can be seen e.g. on left graphs of Figure 54, Figure 55 and Figure 57 (across-track biases of cameras 2, 3 & 5).

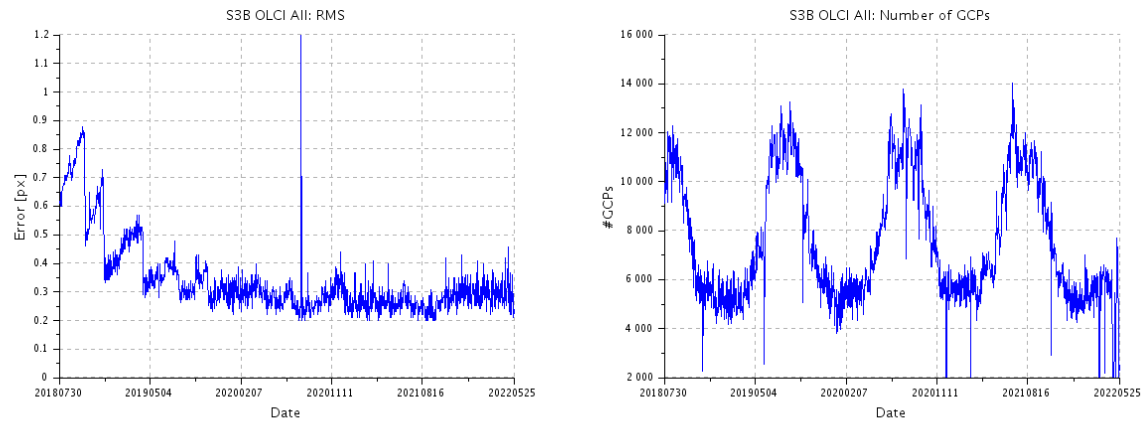

Figure 52: overall OLCI-B georeferencing RMS performance time series over the whole monitoring period (left) and corresponding number of validated control points (right)

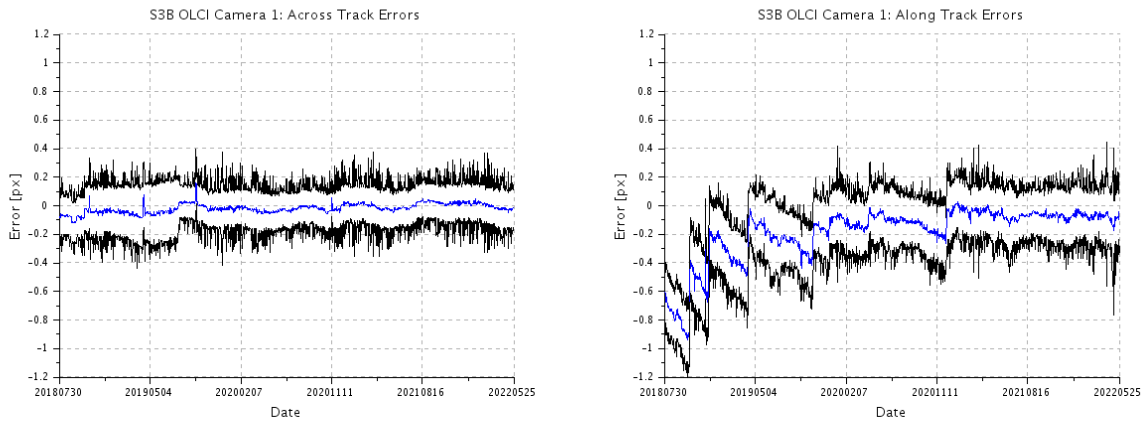

Figure 53: across-track (left) and along-track (right) OLCI-B georeferencing biases time series for Camera 1.

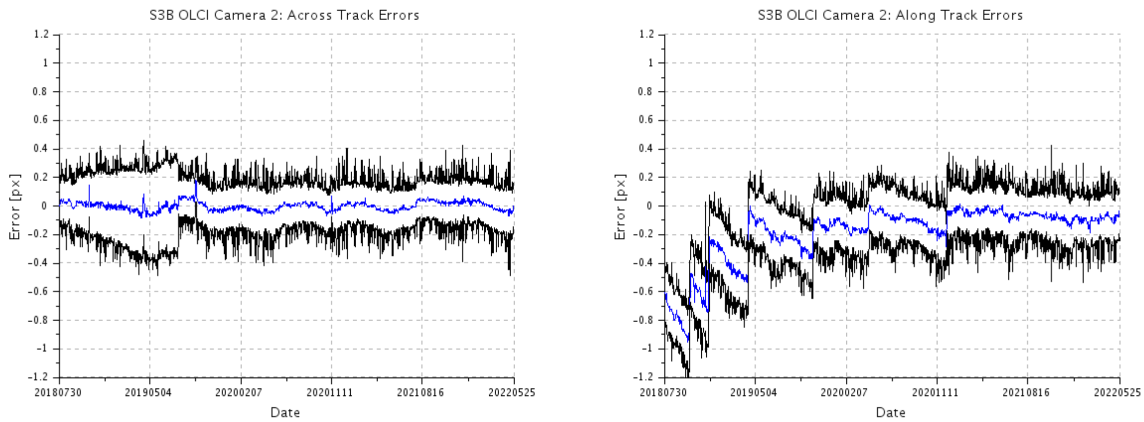

Figure 54: same as Figure 53 for Camera 2.

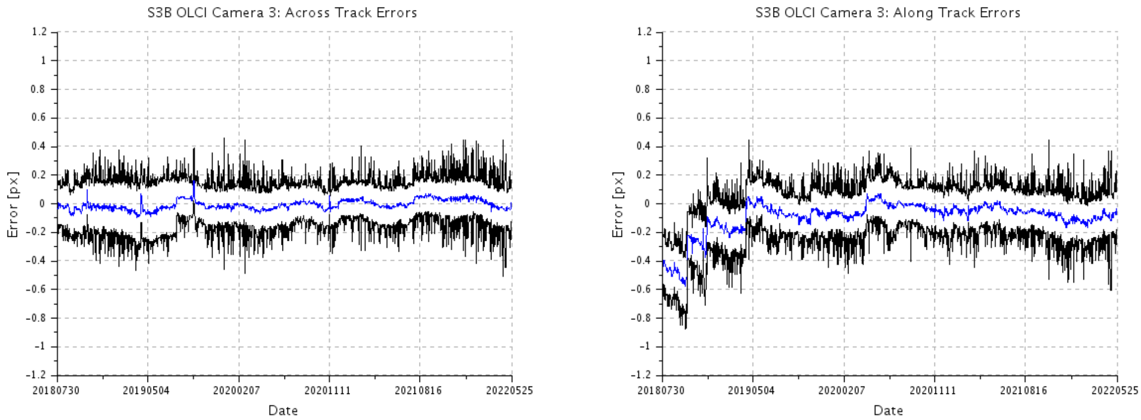

Figure 55: same as Figure 53 for Camera 3.

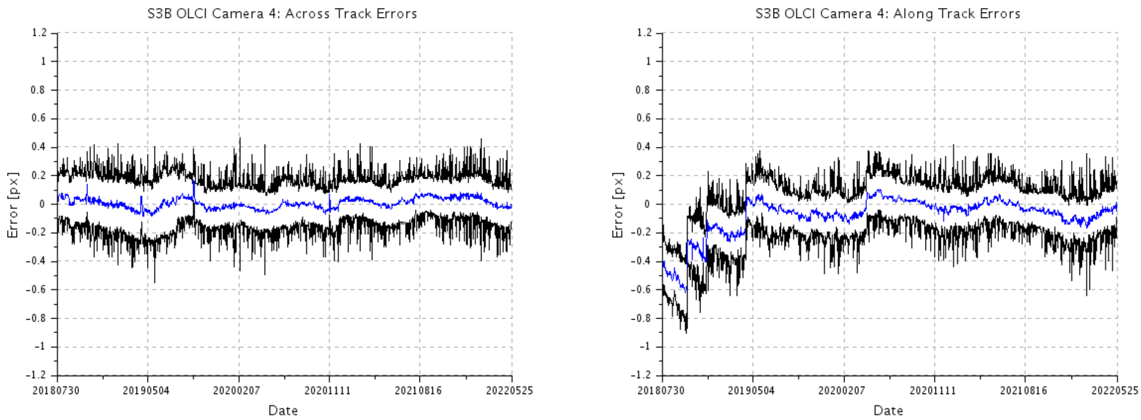

Figure 56: same as Figure 53 for Camera 4.

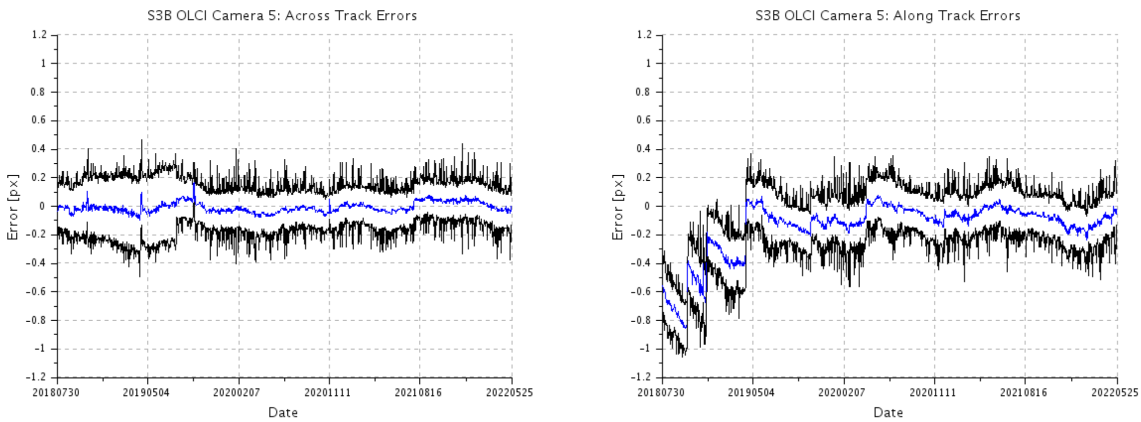

Figure 57: same as Figure 53 for Camera 5.

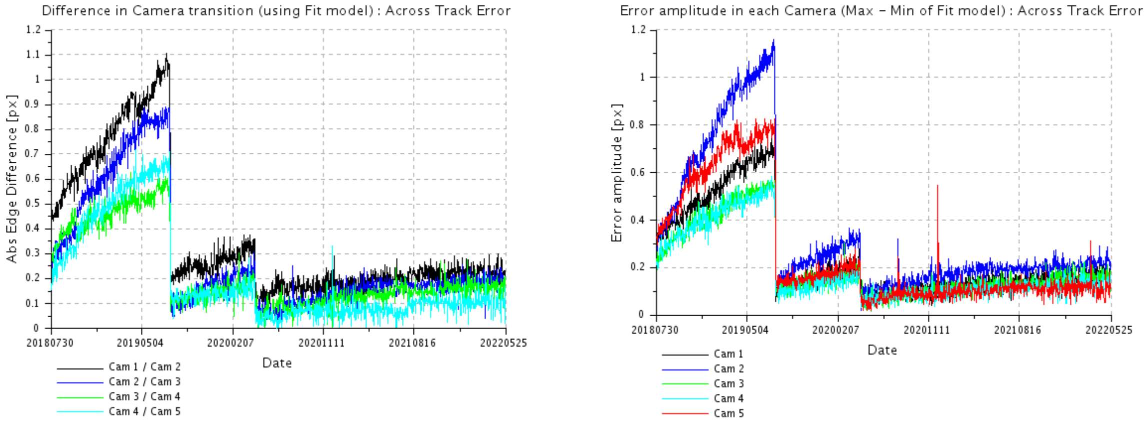

Figure 58: OLCI-B spatial across-track misregistration at each camera transition (left) and maximum amplitude of the across-track error within each camera (left).

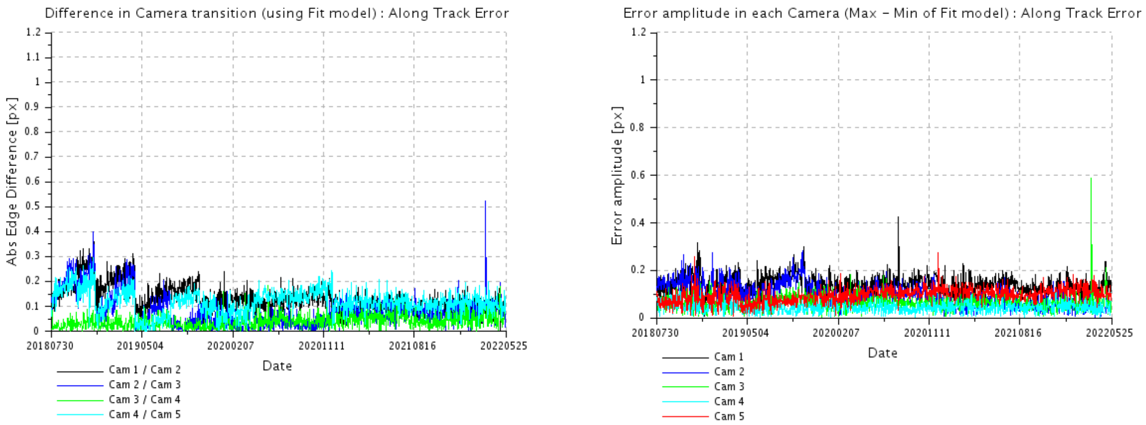

Figure 59: OLCI-B spatial along-track misregistration at each camera transition (left) and maximum amplitude of the along-track error within each camera (left).

3 OLCI Level 1 Product validation

3.1 [OLCI-L1B-CV-300], [OLCI-L1B-CV-310] – Radiometric Validation

3.1.1 S3ETRAC Service

Activities done

The S3ETRAC service extracts OLCI L1 RR and SLSTR L1 RBT data and computes associated statistics over 49 sites corresponding to different surface types (desert, snow, ocean maximizing Rayleigh signal, ocean maximizing sunglint scattering and deep convective clouds). The S3ETRAC products are used for the assessment and monitoring of the L1 radiometry (optical channels) by the ESLs.

All details about the S3ETRAC/OLCI and S3ETRAC/SLSTR statistics are provided on the S3ETRAC website http://s3etrac.acri.fr/index.php?action=generalstatistics.

- Number of OLCI products processed by the S3ETRAC service
- Statistics per type of target (DESERT, SNOW, RAYLEIGH, SUNGLINT and DCC)
- Statistics per sites
- Statistics on the number of records

For illustration, we provide below statistics on the number of S3ETRAC/OLCI records generated per type of targets (DESERT, SNOW, RAYLEIGH, SUNGLINT and DCC) for both OLCI-A (Figure 60) and OLCI-B (Figure 61).

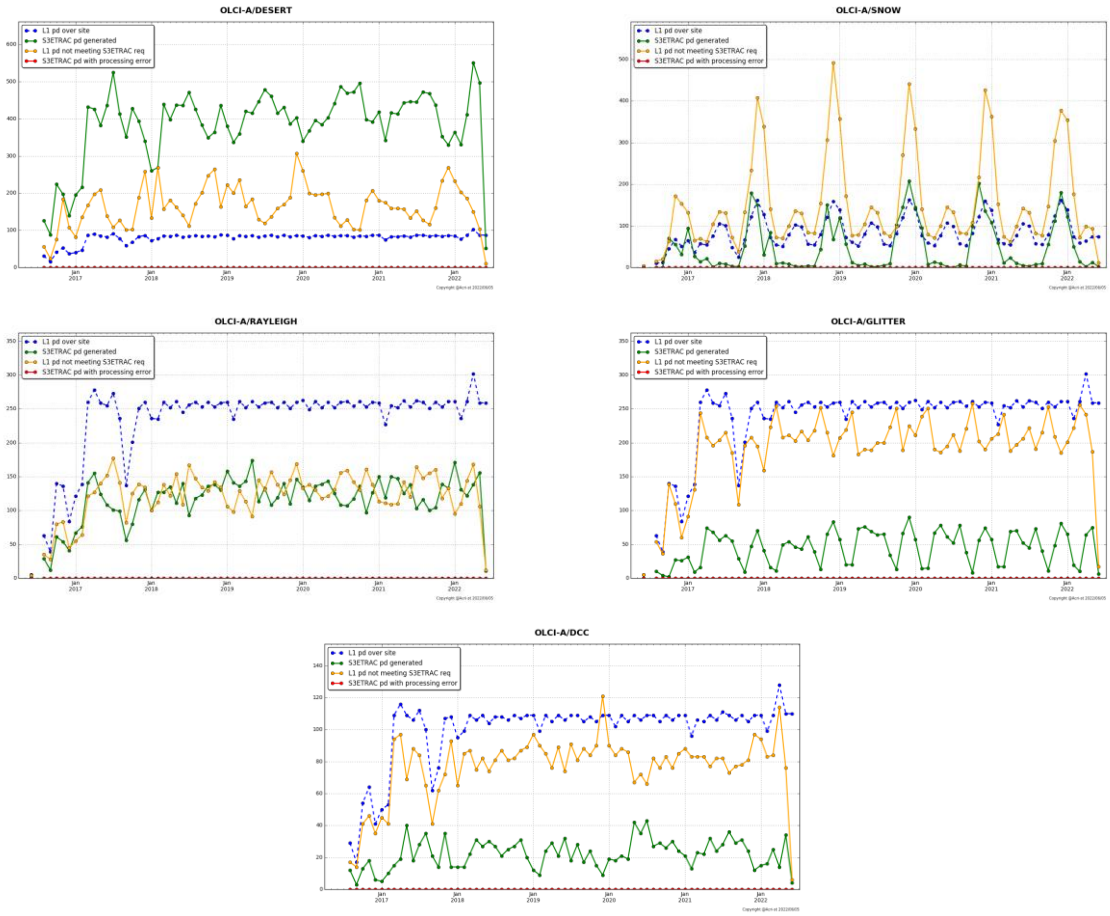

Figure 60: summary of S3ETRAC products generation for OLCI-A (number of OLCI-A L1 products Ingested, blue – number of S3ETRAC extracted products generated, green – number of S3ETRAC runs without generation of output product (data not meeting selection requirements), yellow – number of runs ending in error, red, one plot per site type).

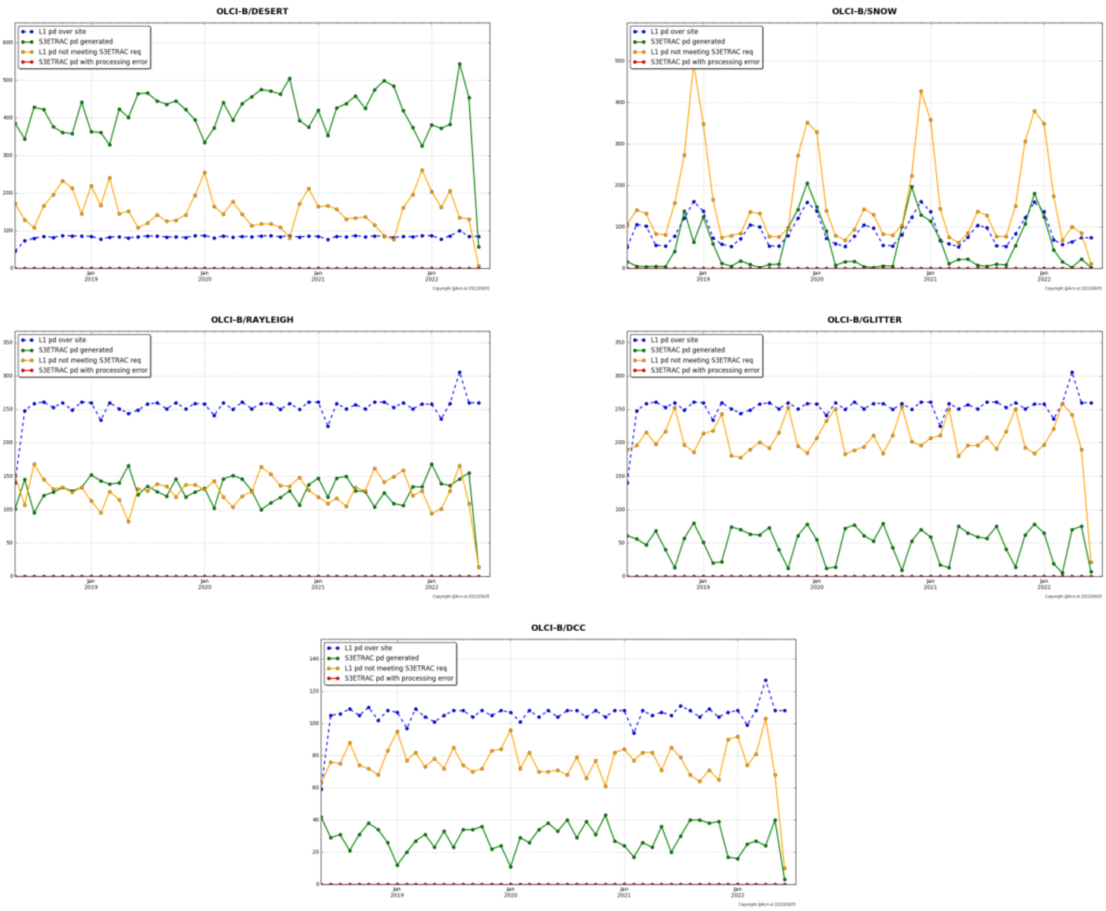

Figure 61: summary of S3ETRAC products generation for OLCI-B (number of OLCI-B L1 products Ingested, yellow – number of S3ETRAC extracted products generated, blue – number of S3ETRAC runs without generation of output product (data not meeting selection requirements), green – number of runs ending in error, red, one plot per site type).

3.1.2 Radiometric validation with DIMITRI

Highlights

OLCI-A and OLCI-B L1B radiometry verification has been processed as follows:

- The verification is performed over Ocean and Desert sites **until 30th of April 2022**, as reported in last DQR (April 2022). For technical reasons it was not possible to collect and process May's overflights.
- Only cross-mission comparisons have been updated with SLSTR-B results.

Verification and Validation over PICS

There has been no new results processed over the reporting period. Consequently, the last results, presented in April 2022 DQR, remain valid.

Validation over Rayleigh

There has been no new results processed over the reporting period. Consequently, the last results, presented in April 2022 DQR, remain valid.

Validation over Glint and synthesis

There has been no new results processed over the reporting period. Consequently, the last results, presented in April 2022 DQR, remain valid.

Cross-mission Intercomparison over PICS:

X-mission Intercomparison between OLCI-A, OLCI-B, MODIS-A, MSI-A, MSI-B, SLSTR-A and SLSTR-B has been performed until January 2022.

Figure 62 shows the estimated time-averaged gain over different time-series for different sensors over PICS. The spectral bands with significant absorption from water vapor and O_2 are excluded. OLCI-A seems to have higher gain wrt the other sensors (except SLSTR-A/B), and about 1-2% higher gain wrt to OLCI-B over VNIR spectral range.

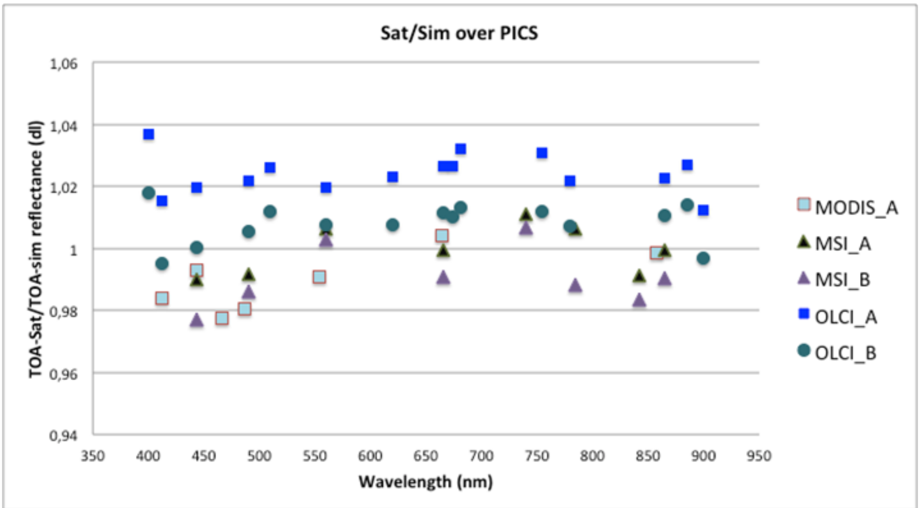

Figure 62: Ratio of observed TOA reflectance to simulated one for (green-yellow) S2A/MSI, (red) Aqua/MODIS, (blue) S3A/OLCI and (green) S3B/OLCI averaged over the six PICS test sites as a function of wavelength.

3.1.3 Radiometric validation with OSCAR

OSCAR Rayleigh results

The OSCAR Rayleigh have been applied to the S3A and S3B S3ETRAC data from the 6 oceanic calibration sites (Table 3) using a new chlorophyll climatology which has been derived from the CMEMS OLCI monthly CHL products from considering the years 2017, 2018 and 2019.

Table 3: S3ETRAC Rayleigh Calibration sites

Site Name	Ocean	North Latitude	South Latitude	East Longitude	West Longitude
PacSE	South-East of Pacific	-20.7	-44.9	-89	-130.2
PacNW	North-West of Pacific	22.7	10	165.6	139.5
PacN	North of Pacific	23.5	15	200.6	179.4
AtlN	North of Atlantic	27	17	-44.2	-62.5
AtlS	South of Atlantic	-9.9	-19.9	-11	-32.3
IndS	South of Indian	-21.2	-29.9	100.1	89.5

In Figure 63 the average OSCAR OLCI-A and OLCI-B Rayleigh results are given for May 2022. In Figure 64 and Table 4 the average of all 2022 scenes currently processed with this new climatology is given. The processing was done on the S3ETRAC scenes from Jan – April. 2022.

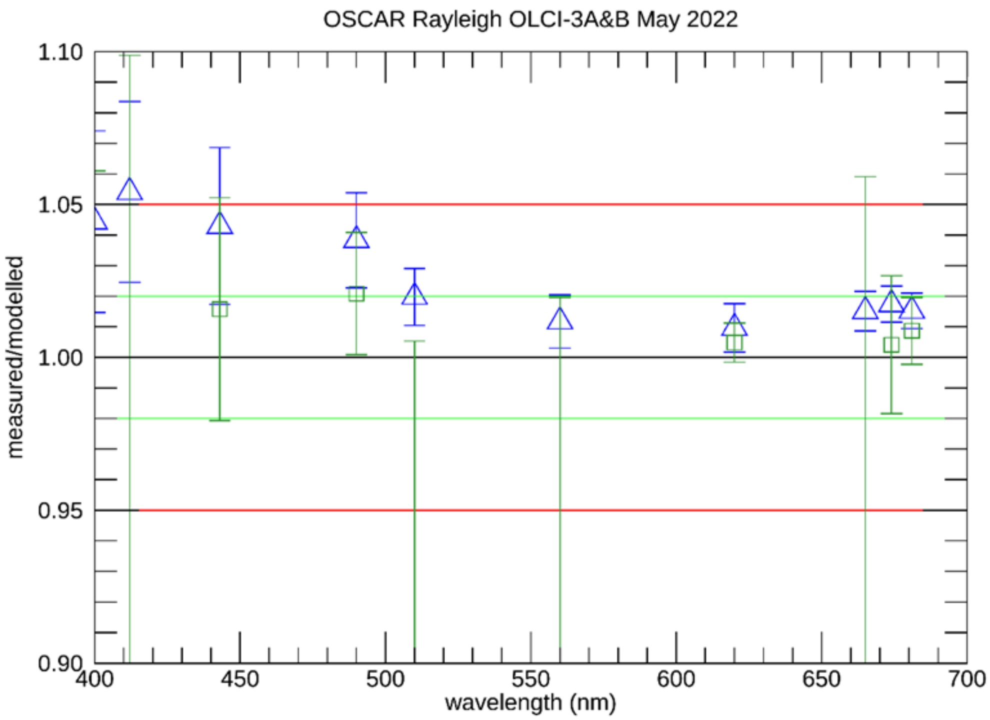

Figure 63: OSCAR Rayleigh S3A and S3B Calibration results as a function of wavelength for March 2022. The results are obtained with a new climatology derived from CMEMS OLCI monthly CHL products.

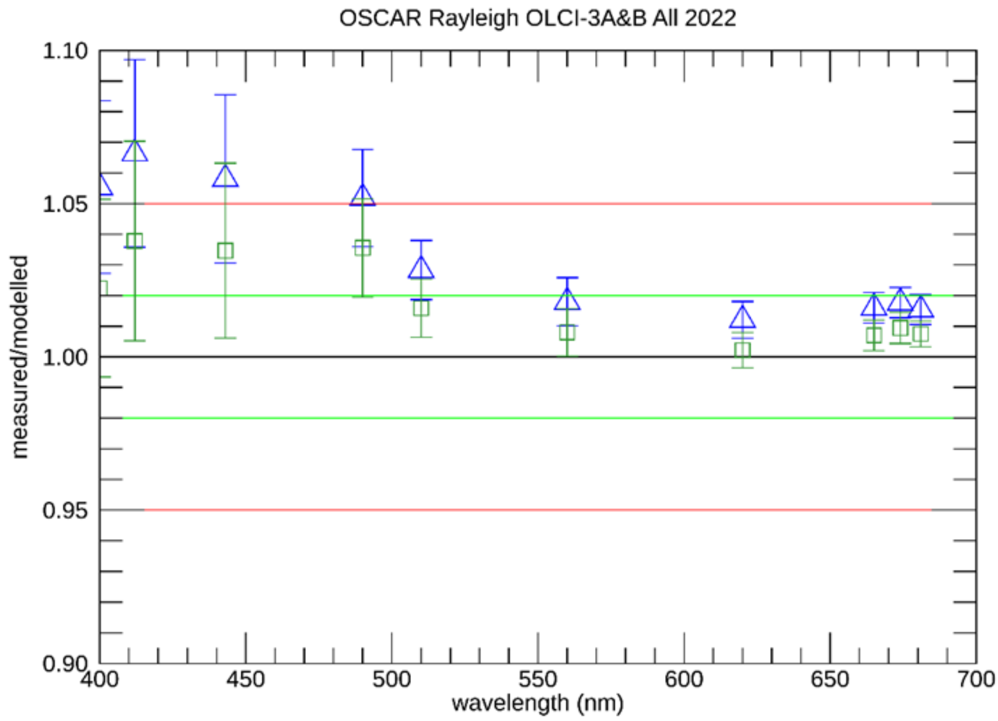

Figure 64. OSCAR Rayleigh S3A and S3B Calibration results as a function of wavelength for Jan – April 2022. Average and standard deviation over all scenes currently (re)processed with the new climatology.

Table 4. OSCAR Rayleigh calibration results for S3A and S3B (average and standard deviation over all acquisitions) over all scenes currently (re)processed with the new climatology and observed difference (in %) between OLCIA and OLCIB

OLCI band	Wavelength (nm)	Oscar Rayleigh OLCIA		Oscar Rayleigh OLCIB		% difference OLCIA and OLCIB
		avg	stdev	avg	stdev	
Oa01	400	1.055	0.028	1.022	0.029	3.12%
Oa02	412	1.066	0.031	1.038	0.033	2.68%
Oa03	443	1.058	0.027	1.035	0.029	2.21%
Oa04	490	1.052	0.016	1.036	0.016	1.55%
Oa05	510	1.028	0.010	1.016	0.009	1.21%
Oa06	560	1.018	0.008	1.008	0.008	0.98%
Oa07	620	1.012	0.006	1.002	0.006	0.98%
Oa08	665	1.016	0.005	1.007	0.005	0.89%
Oa09	674	1.018	0.005	1.009	0.005	0.81%
Oa10	681	1.015	0.005	1.008	0.004	0.78%
Oa11	709	0.999	0.006	0.992	0.006	0.70%
Oa12	754	1.010	0.001	1.008	0.001	0.16%

3.1.4 Radiometric validation with Moon observations

There has been no new result during the reporting period. Last figures (reported in Data Quality Report for February 2022) are considered valid.

4 Level 2 Land products validation

4.1 [OLCI-L2LRF-CV-300]

4.1.1 Routine extractions

- The focus for this time period has been on the rolling archive Non Time Critical (NT) data until the 31st of May 2022. More data available for statistical analysis as a concatenation procedure for all available data in the MERMAID processing has been implemented.
- Concatenated time series of OLCI Global Vegetation Index and OLCI Terrestrial Chlorophyll Index have been regenerated on the current rolling archive availability including previous extractions since June 2016 and April 2018 for S3A and S3B respectively.

4.1.1.1 OLCI-A

Figure 65 to Figure 74 below present the Core Land Sites OLCI-A time series over the current period.

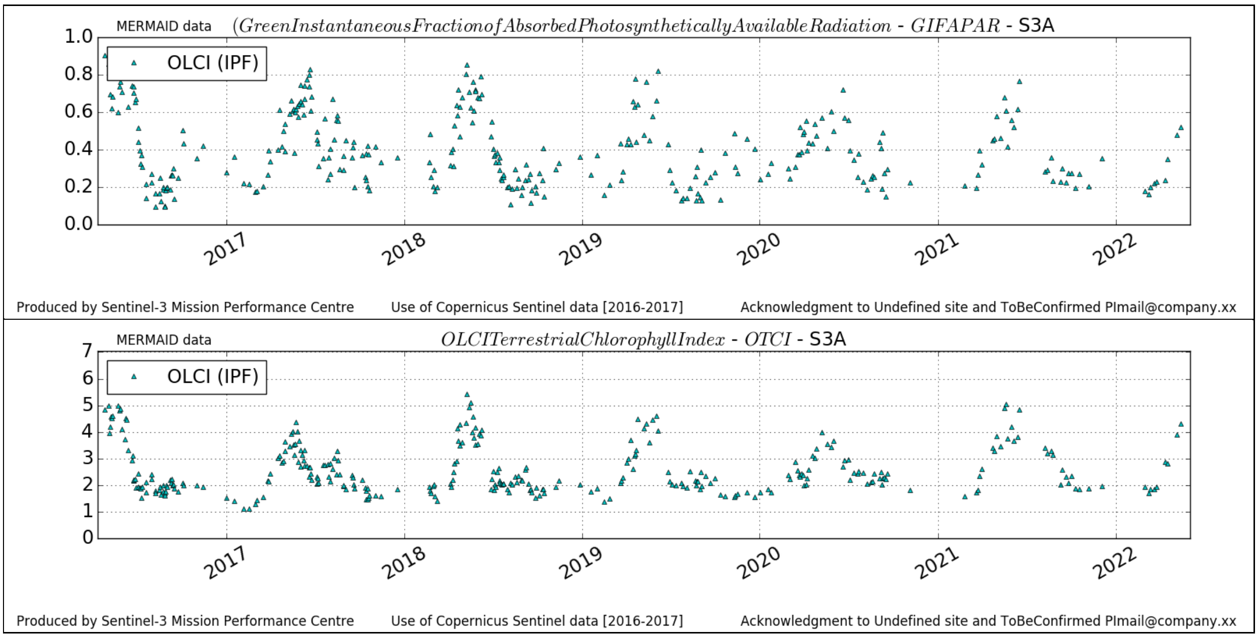

Figure 65: DeGeb time series over current report period

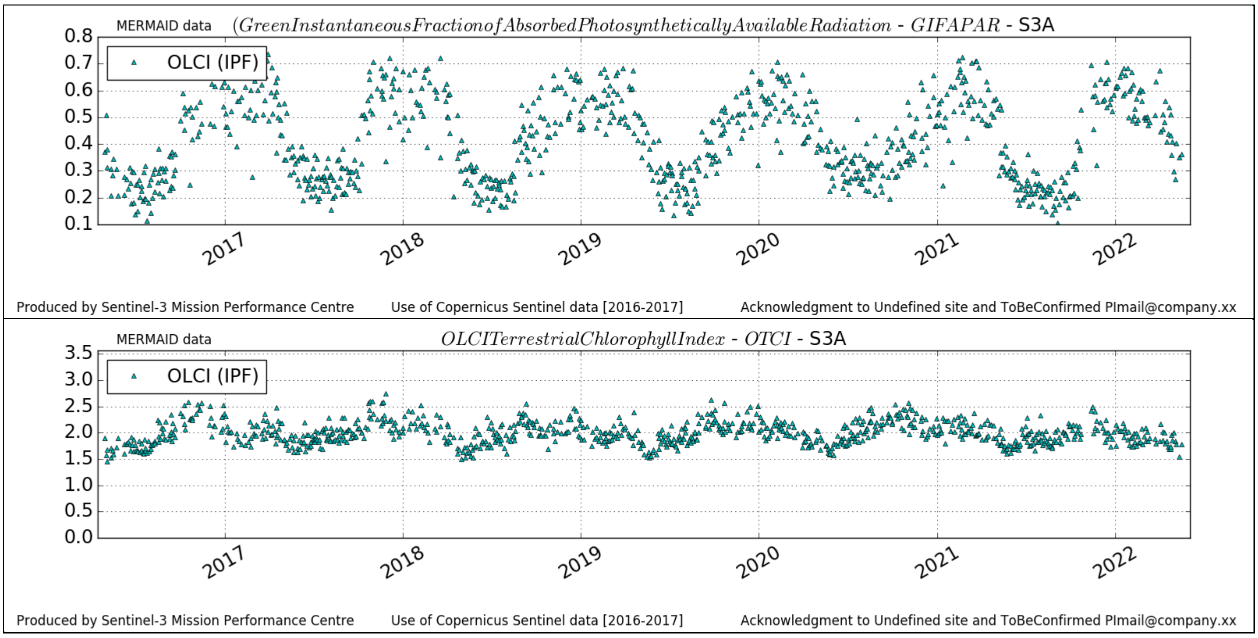

Figure 66: ITCat time series over current report period

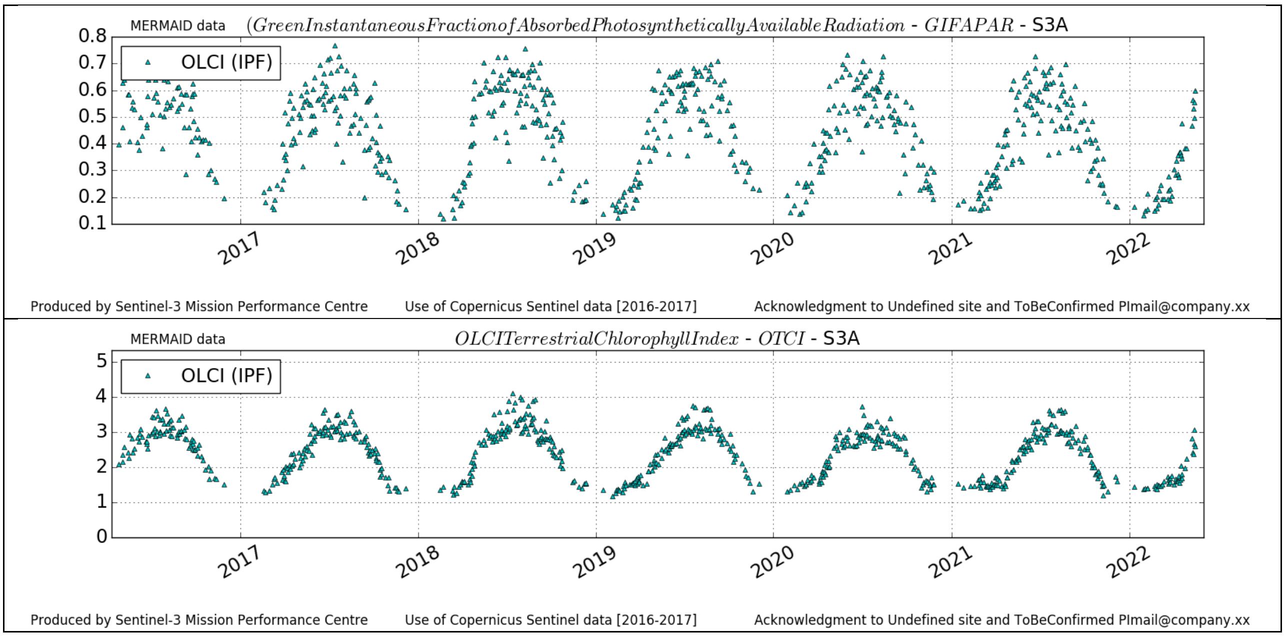

Figure 67: ITIsp time series over current report period

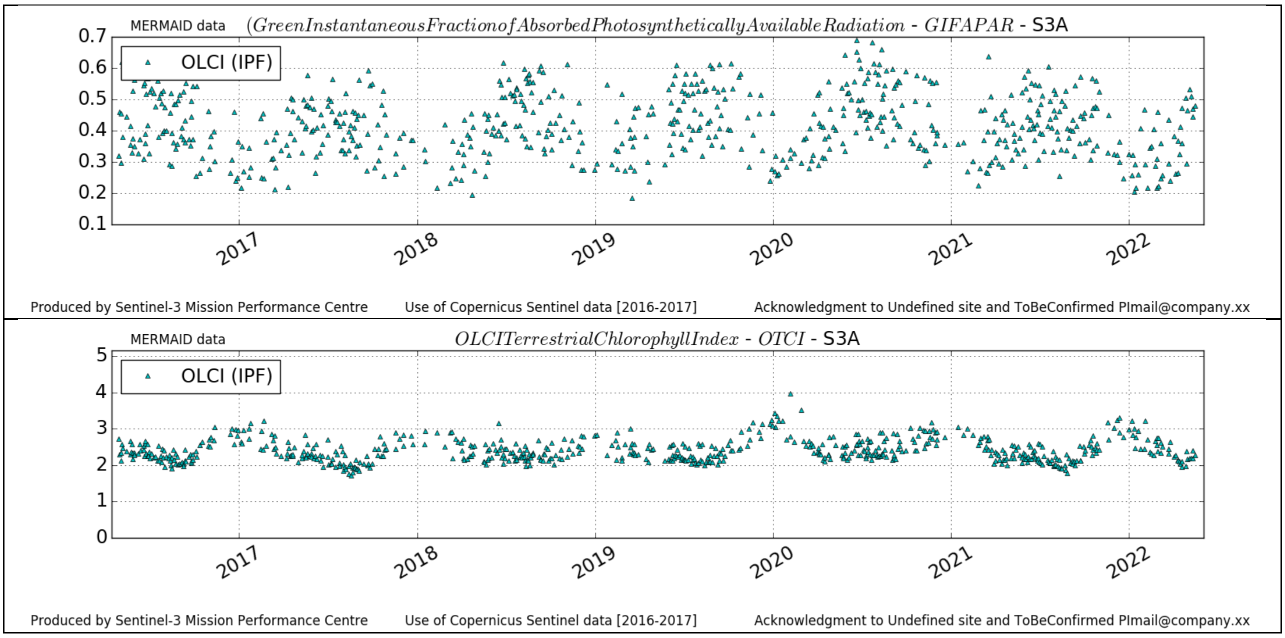

Figure 68: ITSro time series over current report period

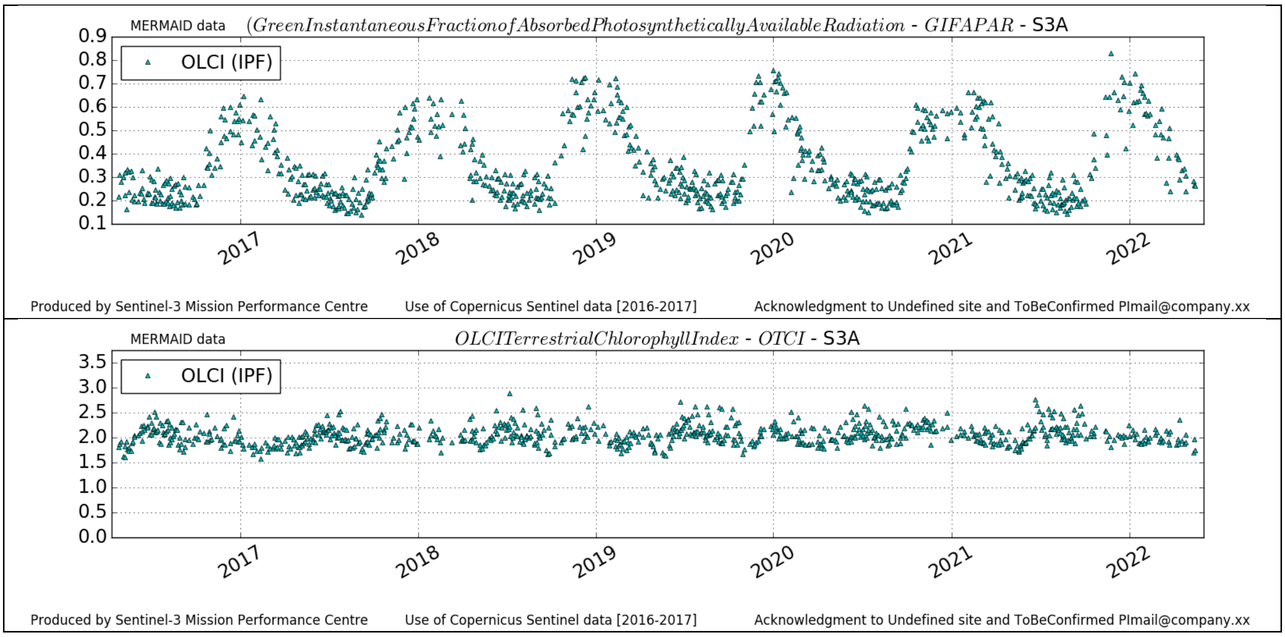

Figure 69: ITTra time series over current report period

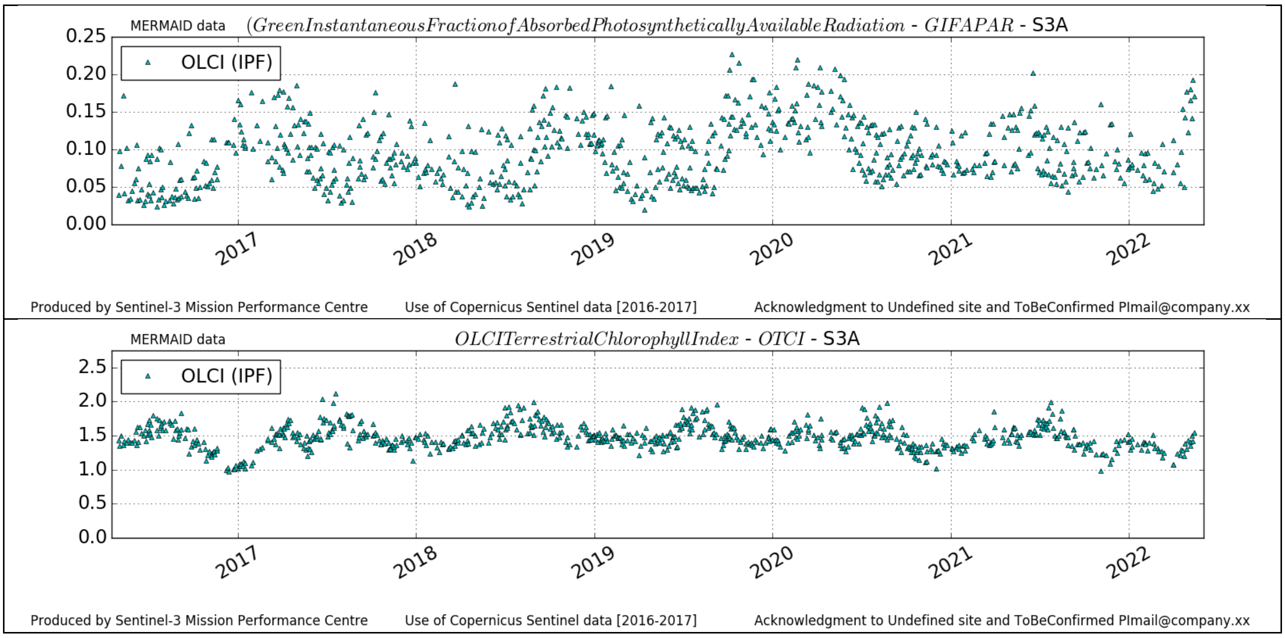

Figure 70: SPAli time series over current report period

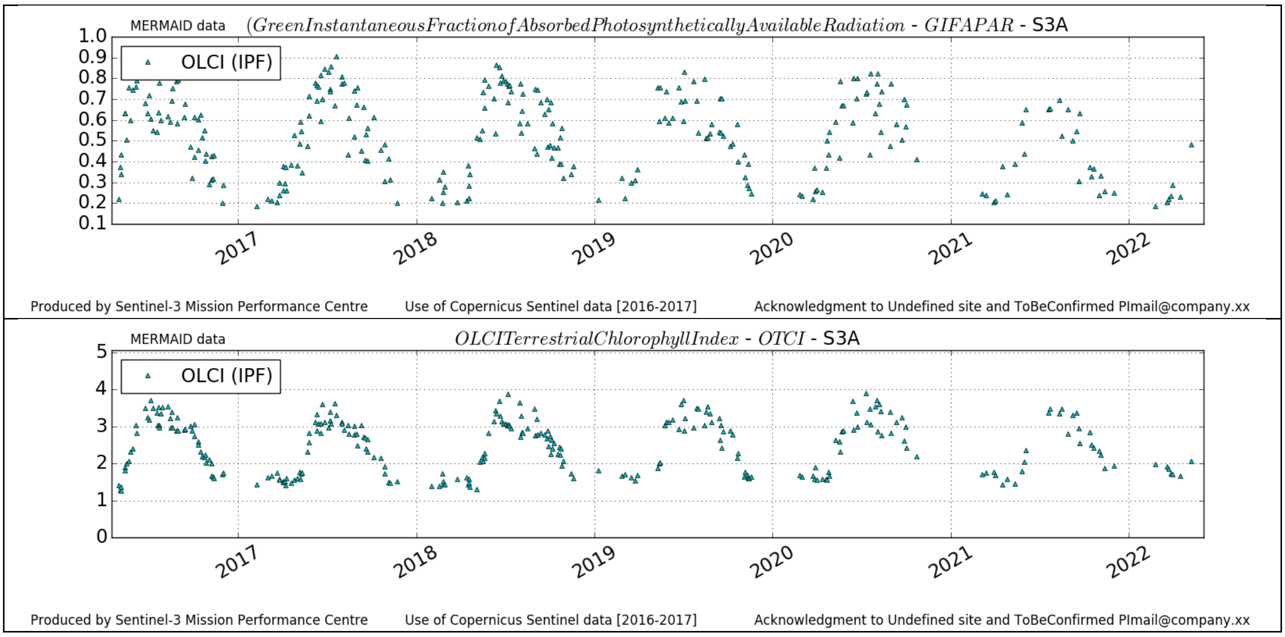

Figure 71: UKNFo time series over current report period

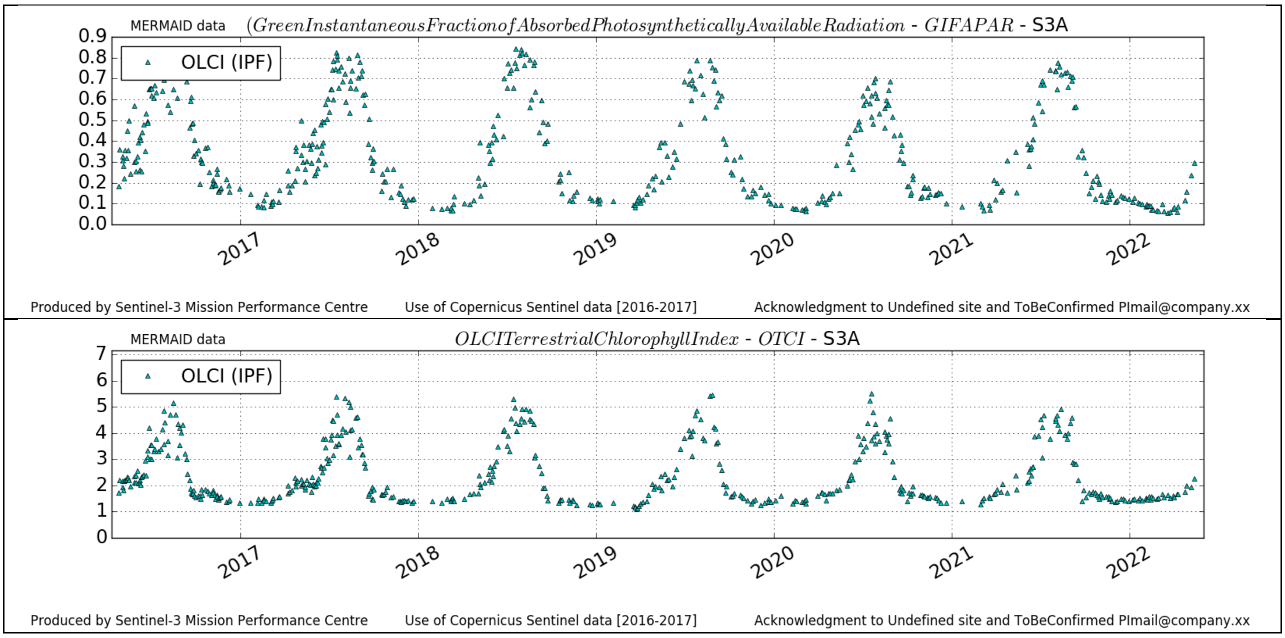

Figure 72: USNe1 time series over current report period

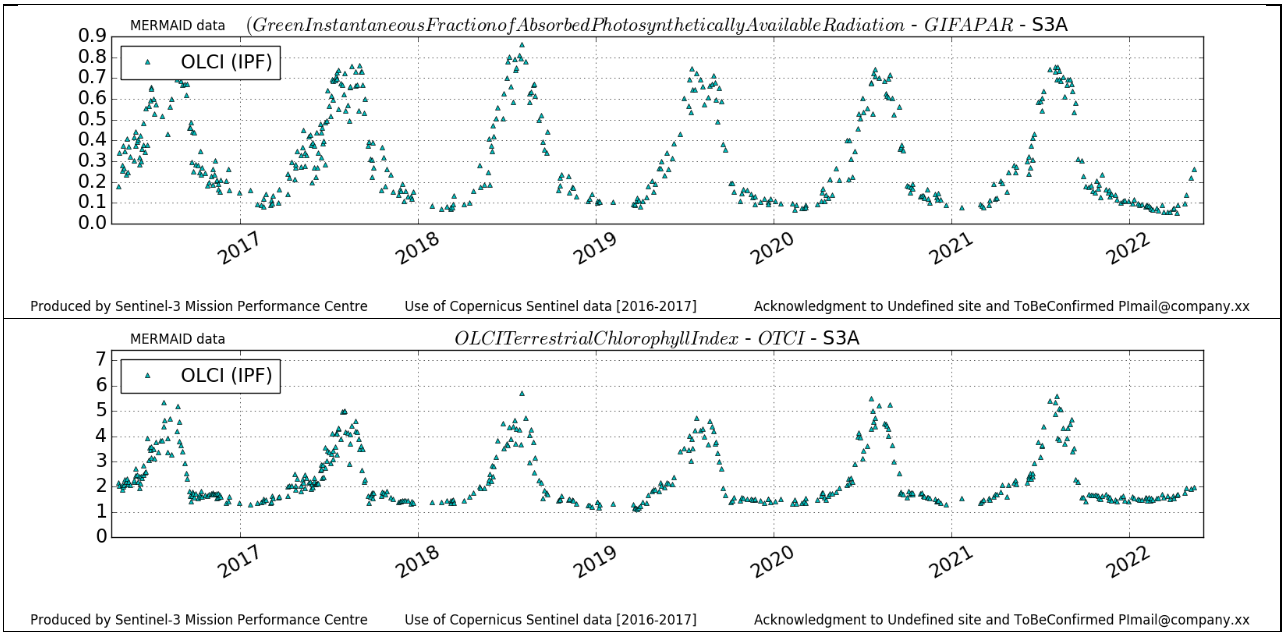

Figure 73: USNe2 time series over current report period

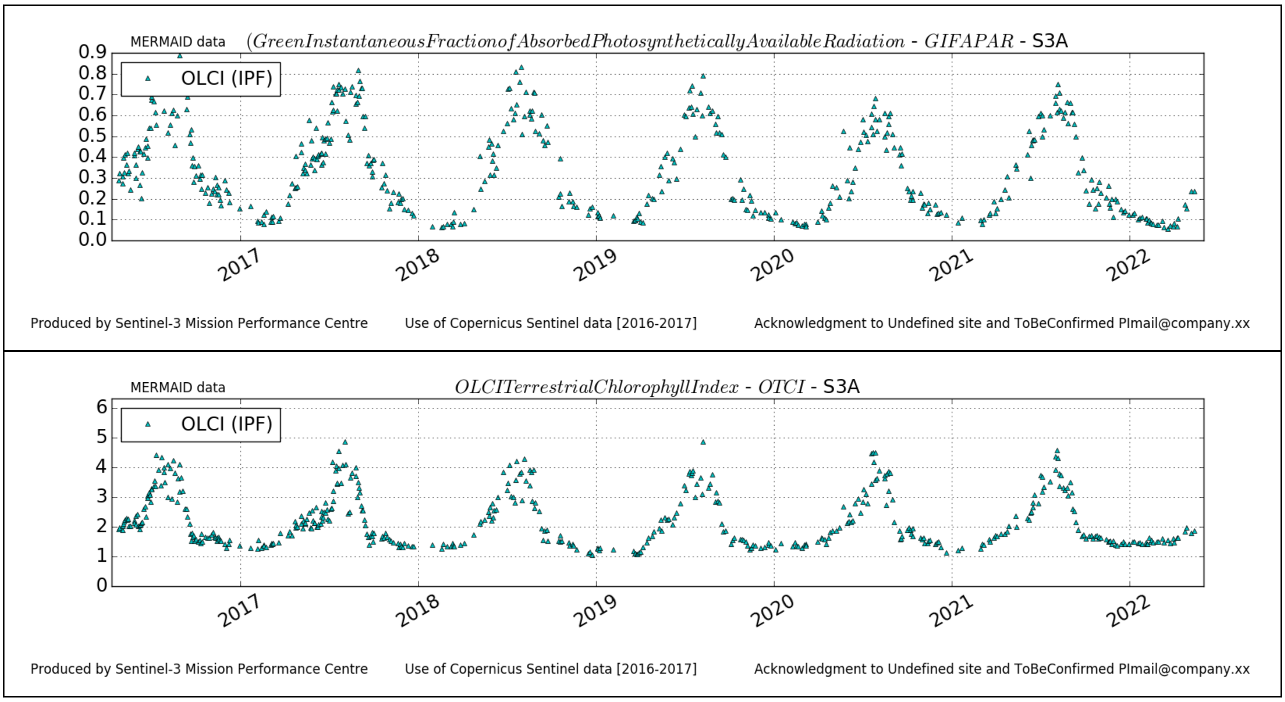

Figure 74: USNe3 time series over current report period

4.1.1.2 OLCI-B

Figure 75 to Figure 84 below present the Core Land Sites OLCI-B time series over the current period.

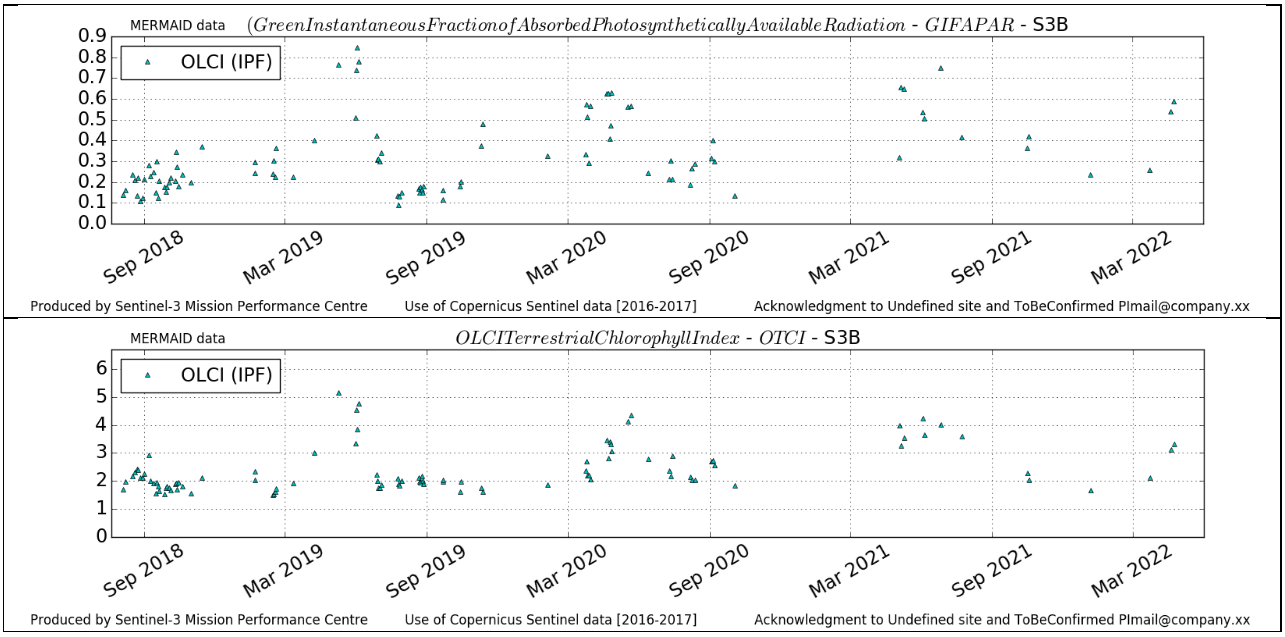

Figure 75: DeGeb time series over current report period

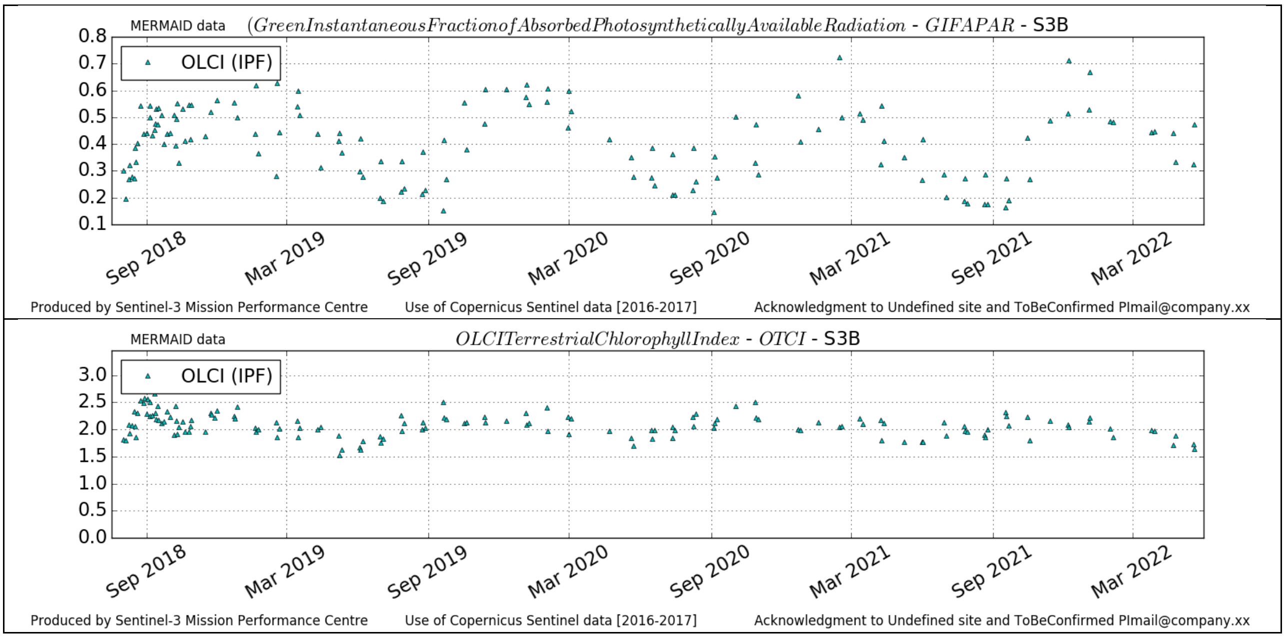

Figure 76: ITCat time series over current report period

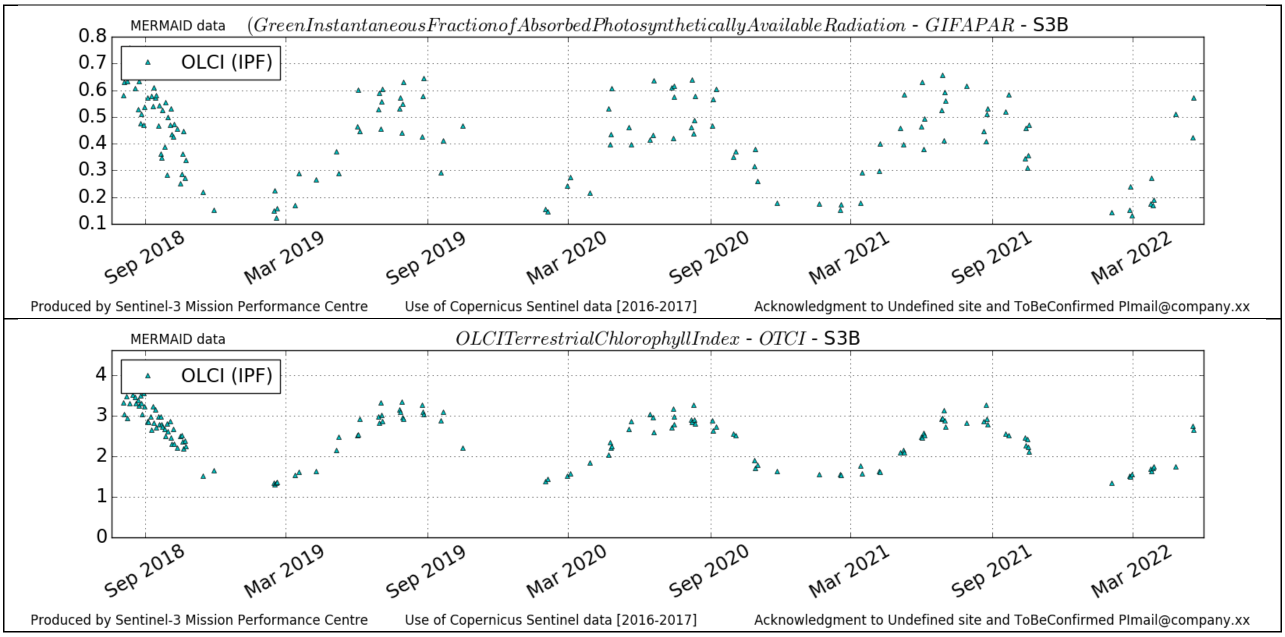

Figure 77: ITIsp time series over current report period

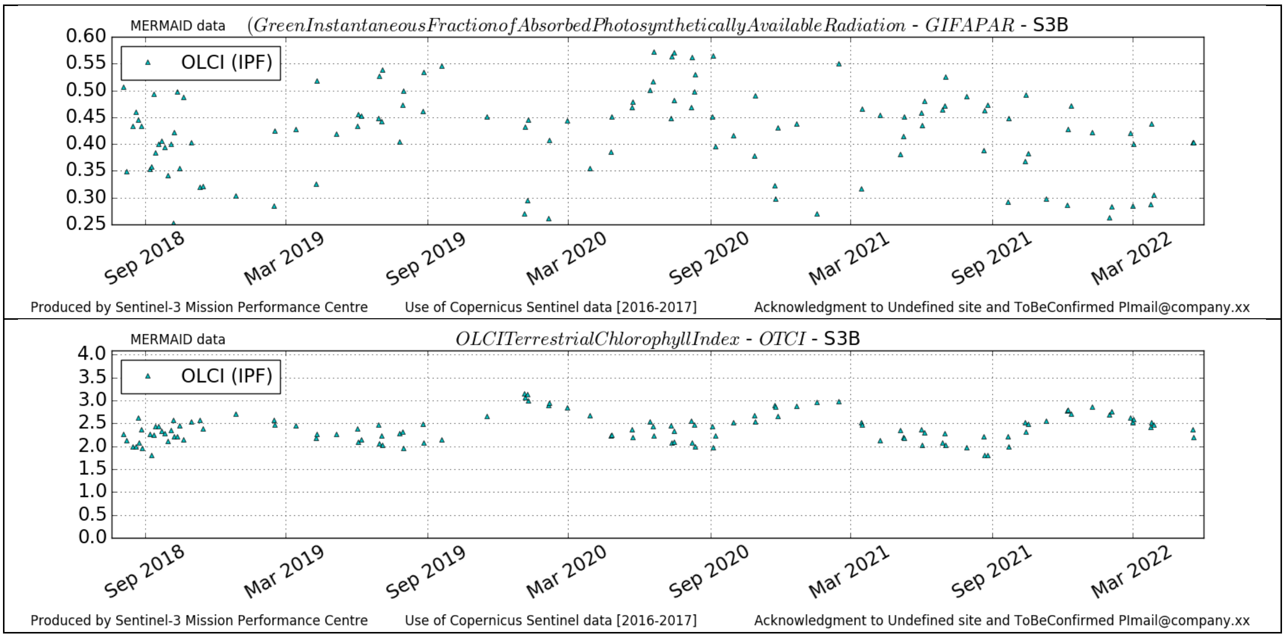

Figure 78: ITSro time series over current report period

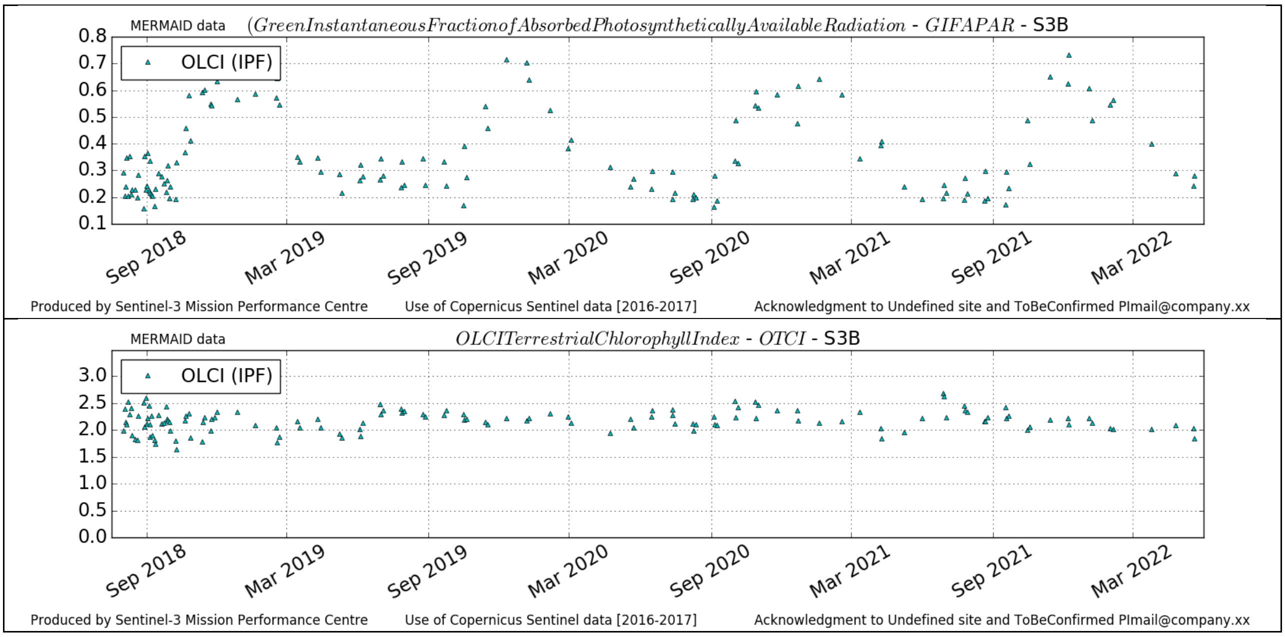

Figure 79: ITTra time series over current report period

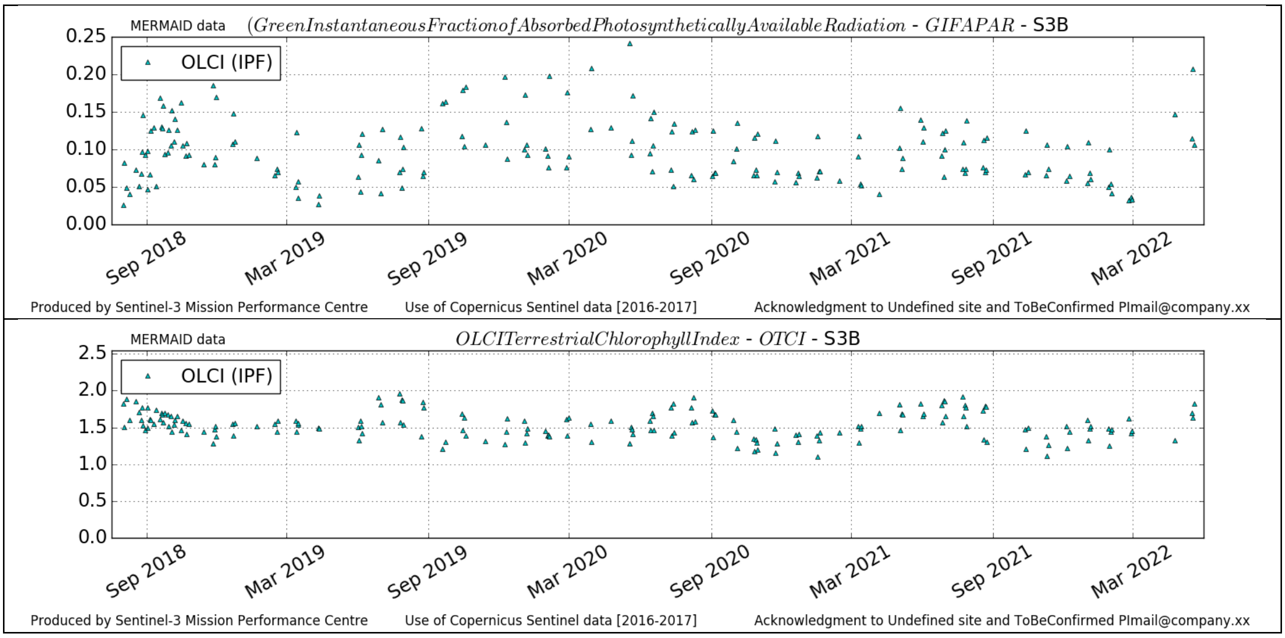

Figure 80: SPAli time series over current report period

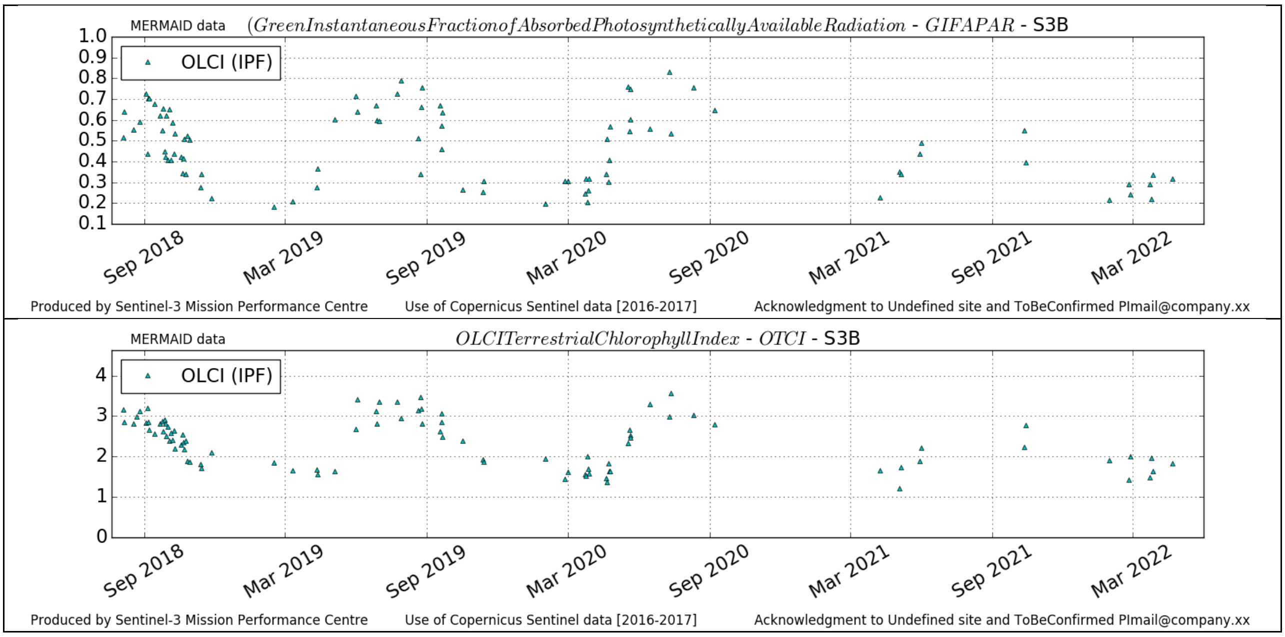

Figure 81: UKNFo time series over current report period

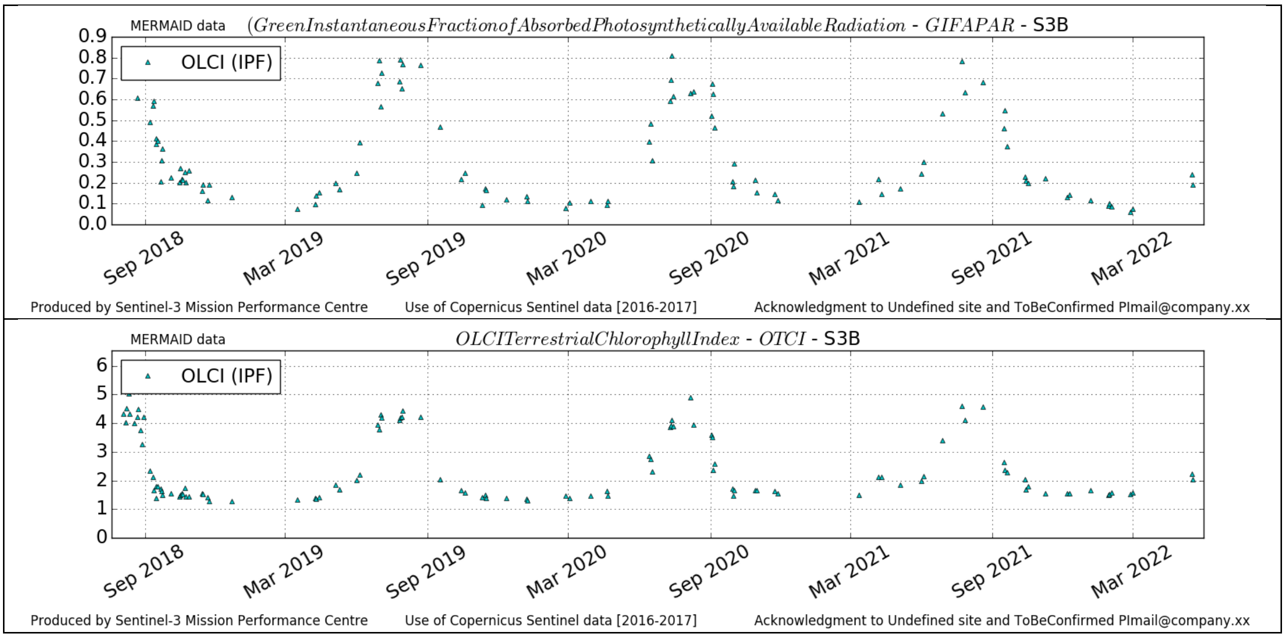

Figure 82: USNe1 time series over current report period

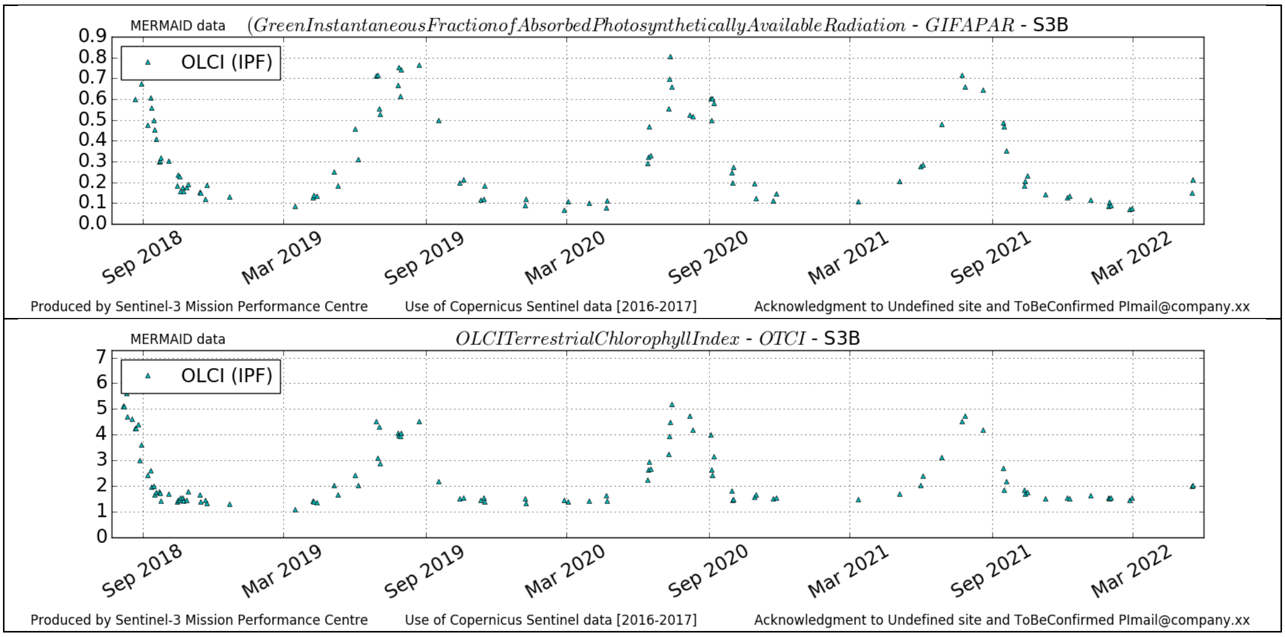

Figure 83: USNe2 time series over current report period

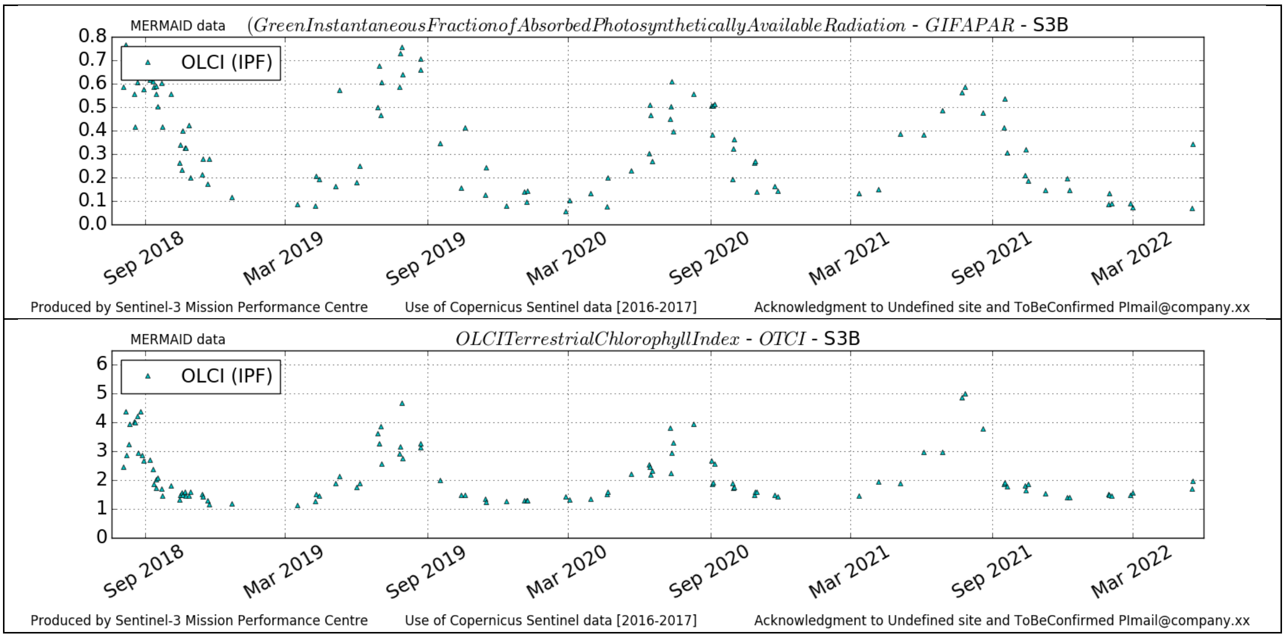

Figure 84: USNe3 time series over current report period

4.1.2 Comparisons with MERIS MGVI and MTCI climatology

This report presents the comparison between MERIS and OLCI land products between the 1st and the 31st of May 2022. The comparison is conducted using 3x3 pixel extractions over 42 established validation sites. The sites are distributed across a range of latitudes and include representative land cover types (Table 5). Statistical measures of the comparison between MERIS and OLCI products are presented in Table 6. In general, there is good agreement between the land products with strong R^2 values and biases around 0. There are similar seasonal trajectories and timings shown in the extractions from both products at the following sites reviewed in this monthly report: BE-Brasschaat, DE-Haininch and FR-EstreesMons (Figure 85 to Figure 87). The monthly mean extractions from all sites is shown in Figure 88. OTCI from S3A shows a strong agreement with the MERIS archive, $R^2 = 0.93$, NRMSD < 0.08 with a low bias, -0.02. OGVI similarly shows a strong agreement with the MERIS archive, $R^2 = 0.93$, NRMSD < 0.15 with a slightly higher bias of 0.06.

Table 5: Validation sites analysed in monthly report. Land cover data from GLC2000 grouped according to the International Geosphere-Biosphere Programme (IGBP) designations.

Acronym	Country	Network	Lat	Lon	Land cover
AU-Cape-Tribulation	Australia	TERN-SuperSites, OzFlux	-16.106	145.378	EBF
AU-Cumberland	Australia	TERN-SuperSites, AusCover/OzFlux	-33.615	150.723	EBF
AU-Great-Western	Australia	TERN-SuperSites, AusCover/OzFlux	-30.192	120.654	DBF
AU-Litchfield	Australia	TERN-SuperSites, AusCover/OzFlux	-13.18	130.79	EBF
AU-Robson-Creek	Australia	TERN-SuperSites, AusCover/OzFlux	-17.117	145.63	EBF
AU-Rushworth	Australia	TERN-AusCover	-36.753	144.966	DBF
AU-Tumbarumba	Australia	TERN-SuperSites, AusCover/OzFlux	-35.657	148.152	EBF
AU-Warra-Tall	Australia	TERN-SuperSites, AusCover/OzFlux	-43.095	146.654	EBF
AU-Watts-Creek	Australia	TERN-AusCover	-37.689	145.685	EBF
AU-Wombat	Australia	TERN-SuperSites, AusCover/OzFlux	-37.422	144.094	EBF
BE-Brasschaat	Belgium	ICOS	51.308	4.52	ENF
BE-Vielsalm	Belgium	ICOS	50.305	5.998	ENF
BR-Mata-Seca	Brazil	ENVIRONET	-14.88	-43.973	non-forest
CA-Mer-Bleue	Canada	National Capitol Comission	45.4	-75.493	non-forest
CR-Santa-Rosa	Costa Rica	ENVIRONET	10.842	-85.616	EBF
CZ-Bili-Kriz	Czechia	ICOS	49.502	18.537	ENF
DE-Haininch	Deutschland	ICOS Associated	51.079	10.453	DBF
DE-Hones-Holz	Deutschland	ICOS	52.085	11.222	DBF
DE-Selhausen	Deutschland	ICOS	50.866	6.447	cultivated
DE-Tharandt	Deutschland	ICOS	50.964	13.567	ENF
FR-Aurade	France	ICOS	43.55	1.106	cultivated
FR-Estrees-Mons	France	ICOS Associated	49.872	3.021	cultivated
FR-Guayaflux	France	ICOS Associated	5.279	-52.925	EBF
FR-Hesse	France	ICOS	48.674	7.065	DBF
FR-Montiers	France	ICOS	48.538	5.312	DBF
FR-Puechabon	France	ICOS	43.741	3.596	ENF
IT-Casterporziano2	Italy	ICOS	41.704267	12.357293	DBF
IT-Collelongo	Italy	EFDC	41.849	13.588	DBF
IT-Lison	Italy	ICOS	45.74	12.75	cultivated
NE-Loobos	Netherlands	ICOS Associated	52.166	5.744	ENF
SE-Dahra	Senegal	KIT / UC	15.4	-15.43	cultivated
UK-Wytham-Woods	United Kingdom	ForestGeo - NPL	51.774	-1.338	DBF
US-Bartlett	United States	NEON, AERONET	44.064	-71.287	DBF
US-Central-Plains	United States	NEON, AERONET	40.816	-104.746	non-forest
US-Harvard	United States	NEON, AERONET	42.537	-72.173	DBF
US-Moab-Site	United States	NEON, AERONET	38.248	-109.388	non-forest
US-Mountain-Lake	United States	NEON, AERONET	37.378	-80.525	DBF
US-Oak-Rige	United States	NEON, AERONET	35.964	-84.283	DBF
US-Ordway-Swisher	United States	NEON, AERONET	29.689	-81.993	ENF
US-Smithsonian	United States	NEON, AERONET	38.893	-78.14	DBF
US-Steigerwarldt	United States	NEON	45.509	-89.586	DBF
US-Talladega	United States	NEON, AERONET	32.95	-87.393	ENF

Table 6: Comparison statistics between monthly S3A/B OLCI land products and MERIS archive data

Site Acronym	S3A								S3B							
	OTCI vs MTCI				OGVI vs MGVI				OTCI vs MTCI				OGVI vs MGVI			
	n	R2	NRMSD	Bias	n	R2	NRMSD	Bias	n	R2	NRMSD	Bias	n	R2	NRMSD	Bias
AU-Cape-Tribulation	12	0.82	0.04	-0.11	12	0.29	0.04	0.16	12	0.82	0.04	-0.16	12	0.08	0.1	0.18
AU-Cumberland	12	0.82	0.02	-0.01	12	0.64	0.07	0.09	12	0.57	0.04	0.03	12	0.67	0.1	0.09
AU-Great-Western	12	0.96	0.02	0.1	12	0.92	0	0.04	12	0.96	0.02	0.09	12	0.8	0.1	0.02
AU-Robson-Creek	12	0.9	0.04	-0.04	12	0.9	0.04	0.11	12	0.88	0.04	-0.13	12	0.8	0.07	0.13
AU-Rushworth	12	0.83	0.04	0.13	12	0.56	0.04	0.09	12	0.84	0.03	0.02	12	0.49	0.08	0.06
AU-Tumbarumba	12	0.89	0.04	0.31	12	0.52	0.06	0.09	12	0.92	0.03	0.15	12	0.17	0.1	0.01
AU-Warra-Tall	12	0.72	0.06	-0.06	12	0.26	0.17	0.04	10	0.48	0.07	-0.43	10	0.41	0.1	-0.02
AU-Watts-Creek	12	0.69	0.05	0.03	12	0.03	0.06	0.08	12	0.8	0.04	0.01	12	0.3	0.08	0.09
AU-Wombat	12	0.91	0.03	0.11	12	0.49	0.05	0.07	12	0.9	0.03	0	12	0.04	0.08	0.05
BE-Brasschaat	11	0.99	0.03	-0.08	11	0.96	0.08	0.04	10	0.96	0.05	-0.07	10	0.94	0.08	0.02
BE-Vielsalm	3	1	0	0.33	3	0.08	0.11	0.12	10	0.88	0.05	-0.02	10	0.91	0.11	0.13
CA-Mer-Bleue	10	0.95	0.05	0.01	10	0.99	0.06	0.03	10	0.94	0.05	-0.02	10	0.98	0.06	0.01
CZ-Bili-Kriz	10	0.95	0.02	0.04	10	0.96	0.07	0.07	10	0.87	0.04	-0.07	10	0.9	0.1	0.05
DE-Haininch	10	0.99	0.07	-0.04	10	0.98	0.08	0.06	10	0.95	0.12	-0.09	10	0.94	0.18	0.07
DE-Hones-Holz	11	1	0.03	0.08	11	1	0.02	0.04	9	0.92	0.14	-0.05	9	0.94	0.12	0.03
DE-Selhausen	12	0.89	0.07	-0.03	12	0.55	0.21	0.06	12	0.8	0.1	-0.13	12	0.29	0.27	0.02
DE-Tharandt	12	0.97	0.04	-0.03	12	0.96	0.09	0.08	10	0.97	0.05	-0.22	10	0.97	0.09	0.09
FR-Aurade	12	0.79	0.11	0.07	12	0.84	0.16	0.13	11	0.89	0.07	0	11	0.83	0.16	0.08
FR-Estrees-Mons	12	0.94	0.07	0.05	12	0.89	0.11	0.06	12	0.86	0.12	0.14	12	0.89	0.11	0.04
FR-Guayaflux	12	0.7	0.04	-0.16	12	0.22	0.1	0.18	12	0.64	0.04	-0.23	12	0.01	0.2	0.18
FR-Montiers	12	1	0.03	-0.11	12	0.98	0.06	0.05	11	0.96	0.08	-0.15	11	0.95	0.13	0.08
FR-Puechabon	12	0.92	0.02	-0.06	12	0.96	0.03	0.08	12	0.9	0.03	-0.01	12	0.91	0.09	0.06
IT-Casterporziano2	12	0.96	0.02	-0.12	12	0.85	0.03	0.05	12	0.93	0.03	-0.07	12	0.67	0.08	0.01
IT-Collelongo	12	0.98	0.07	0.01	12	0.99	0.08	0.03	12	0.94	0.11	0.06	12	0.93	0.16	0.02
IT-Lison	12	0.99	0.03	-0.05	12	0.97	0.07	0.08	12	0.94	0.05	-0.07	12	0.95	0.1	0.07
NE-Loobos	12	0.76	0.07	0.08	12	0.89	0.1	0.05	12	0.52	0.07	0.05	12	0.86	0.1	0.04
UK-Wytham-Woods	12	0.97	0.05	0.11	12	0.97	0.07	0.11	12	0.94	0.07	0.01	12	0.87	0.14	0.09
US-Bartlett	12	0.96	0.04	-0.01	12	0.98	0.1	0.06	12	0.95	0.05	-0.06	12	0.95	0.12	0.03
US-Central-Plains	12	0.69	0.03	-0.01	12	0.93	0.1	0.01	11	0.72	0.03	-0.04	11	0.81	0.21	0
US-Harvard	12	0.99	0.04	-0.2	12	0.97	0.09	0.04	12	0.98	0.05	-0.23	12	0.93	0.14	0.02
US-Jornada	11	0.67	0.05	0.05	11	0.88	0.2	0.01	10	0.78	0.04	0.07	10	0.38	0.4	0.01
US-Moab-Site	12	0.7	0.02	0.06	12	0.15	0.22	0.01	12	0.75	0.02	0.04	12	0.12	0.22	0.03
US-Mountain-Lake	12	0.99	0.04	-0.18	12	1	0.05	0.04	11	0.99	0.04	-0.29	11	0.98	0.11	0.01
US-Oak-Rige	12	1	0.02	-0.07	12	0.99	0.07	0.05	12	0.99	0.04	-0.09	12	0.98	0.07	0.04
US-Smithsonian	11	0.99	0.04	-0.2	11	0.99	0.07	0.04	10	0.99	0.05	-0.2	10	0.99	0.07	-0.01
US-Steigerwarldt	12	0.99	0.03	0.02	12	0.99	0.05	0	9	0.95	0.06	-0.06	9	0.99	0.05	0.01
US-Talladega	12	0.98	0.02	-0.13	12	0.98	0.05	0.07	12	0.93	0.04	-0.2	12	0.94	0.1	0.06

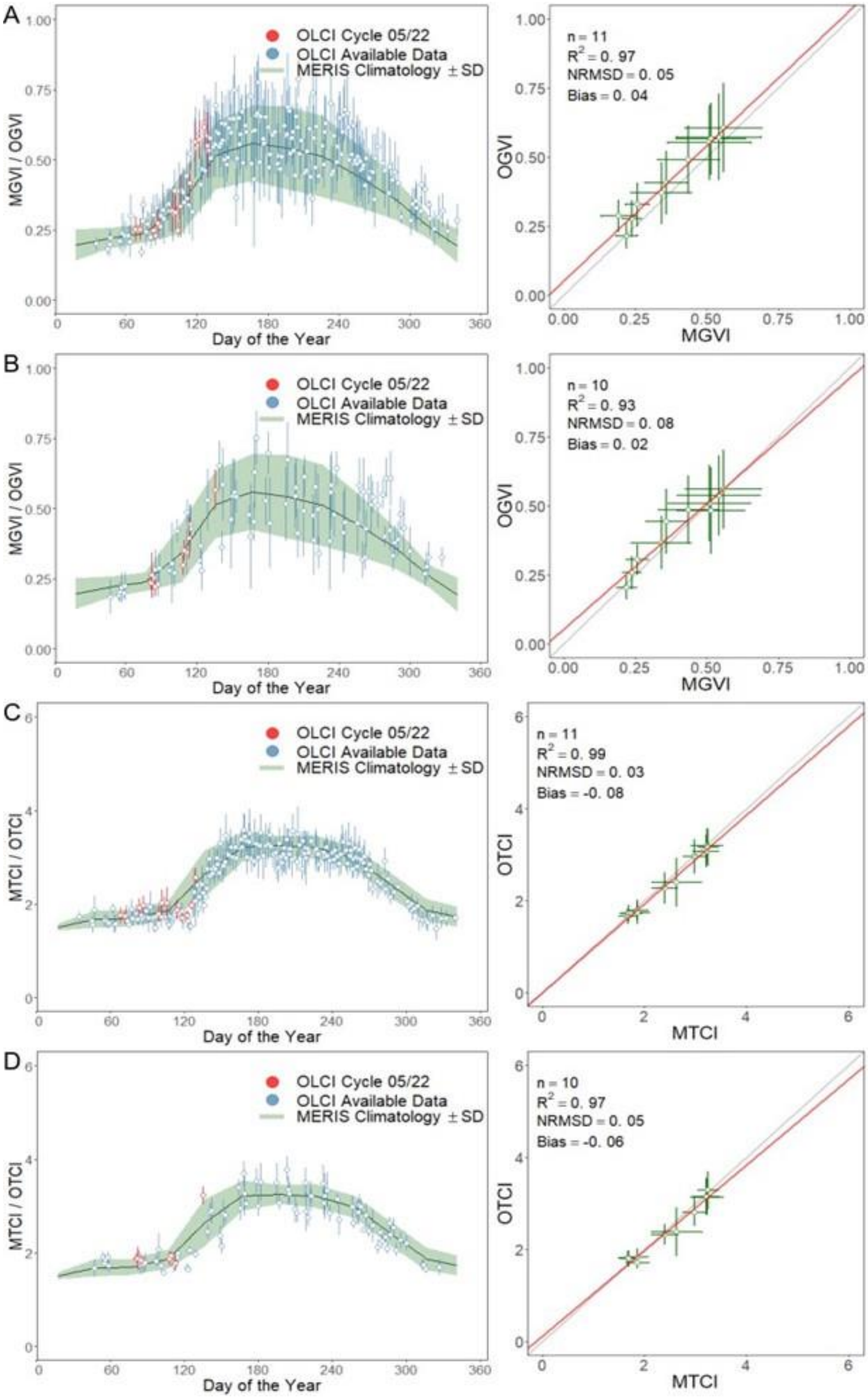

Figure 85: Time-series OGVI and OTCI and corresponding scatterplot of monthly mean for site BE-Brasschaat, Belgium, land cover Needle-leaved, evergreen. A and C represent S3A; B and D represent S3B.

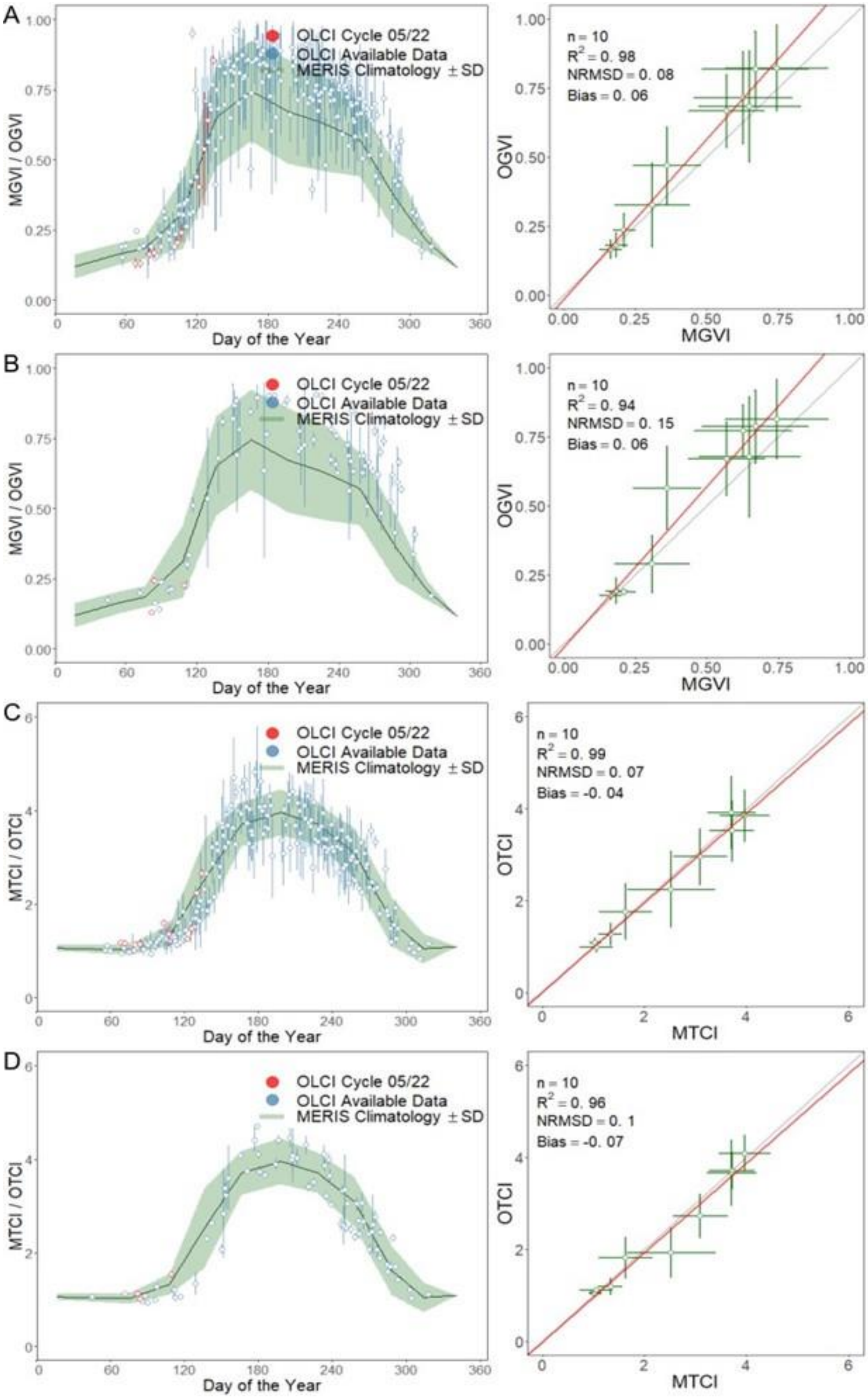

Figure 86: Time-series OGVI and OTCI and corresponding scatterplot of monthly mean for site DE-Hainich, Deutschland, land cover Broadleaved, deciduous, closed. A and C represent S3A; B and D represent S3B.

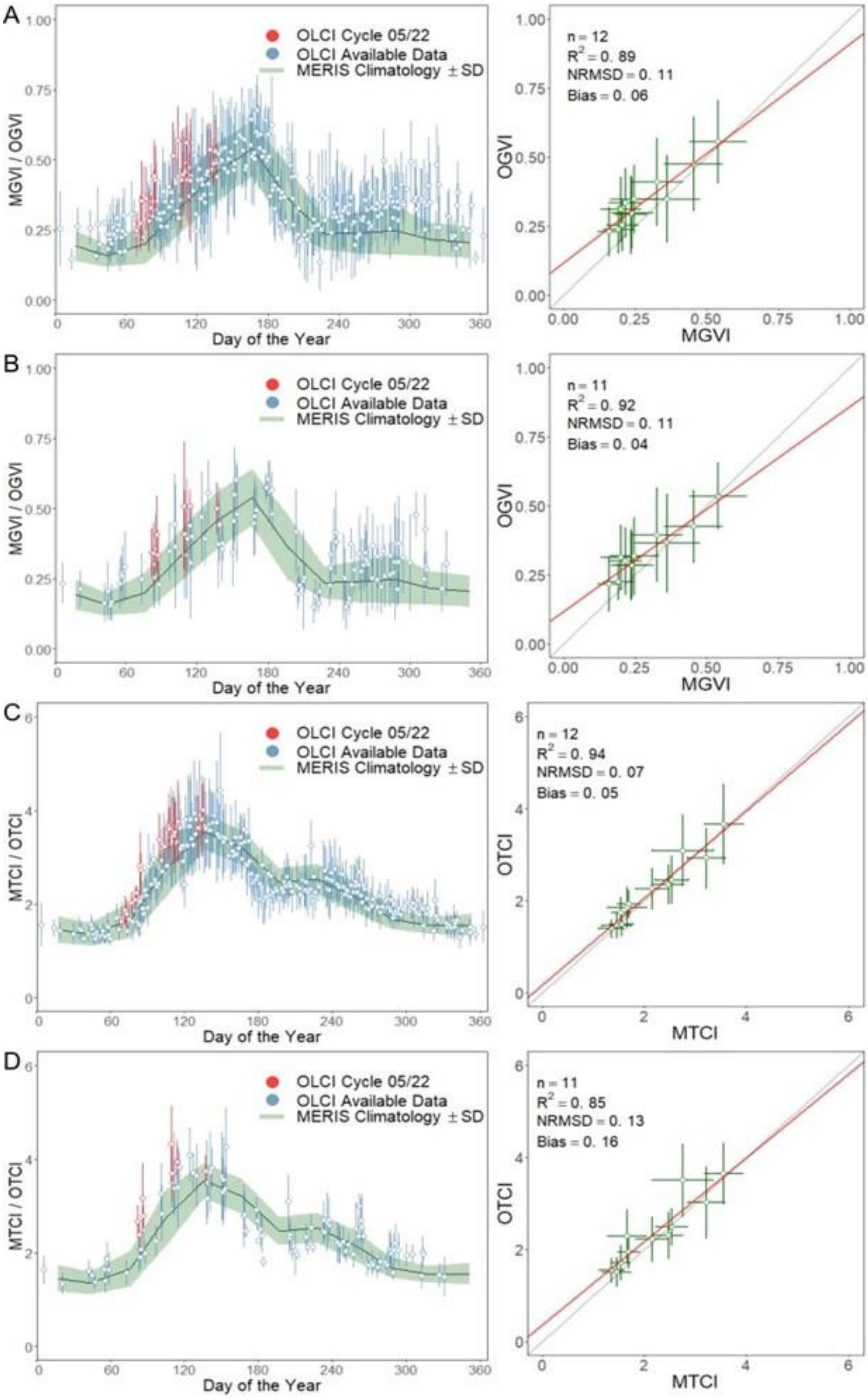

Figure 87: Time-series OGVI and OTCI and corresponding scatterplot of monthly mean for site FR-EstreesMons, France, land cover Cultivated and managed areas. A and C represent S3A; B and D represent S3B.

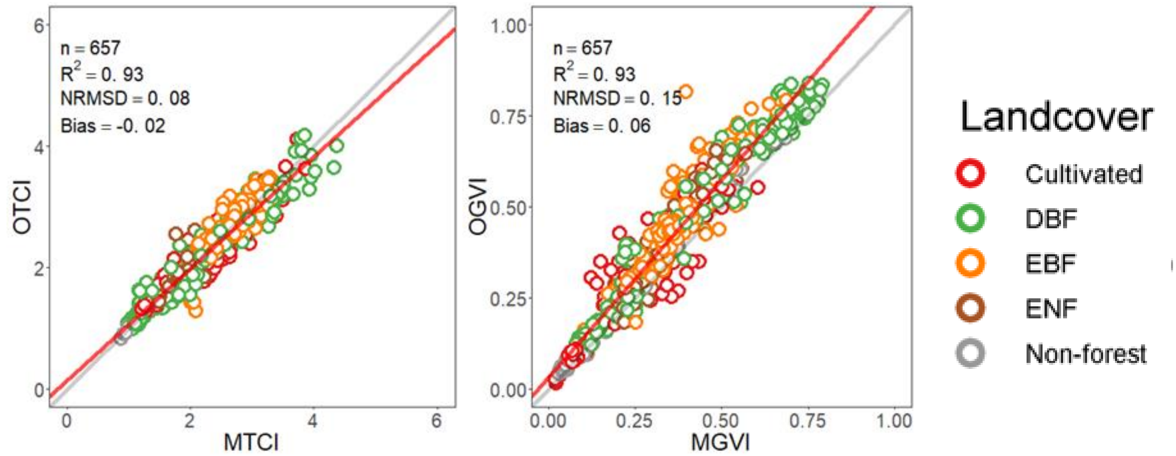

Figure 88: Comparison of OTCI-MTCI (a) and OGVI-MGVI (b). Points in the scatterplot represent the monthly mean of all available S3A and MERIS archive over 42 validation sites. Red and grey lines represent the modelled and 1:1 lines respectively. The scatterplots are updated to include extractions from the latest month

4.2 [OLCI-L2LRF-CV-410 & OLCI-L2LRF-CV-420] – Cloud Masking & Surface Classification for Land Products

There has been no new result during the reporting period. Last figures (reported in OLCI Cyclic Report 074-055) are considered valid.

Routine monitoring activities have been continued.

5 Validation of Integrated Water Vapour over Land & Water

The OLCI L2 IWV processor distinguishes between ocean and land surfaces and works very differently above the respective surfaces. The algorithm above water shows some serious flaws, nevertheless we use comparison to ground truth as a stability measure, since the ocean retrievals belong to low light conditions in contrast to land retrievals.
OLCI's IWV is validated using the following ground truth data:

1. Global GNSS data, with a focus to north America (SUOMI NET, Ware et al. 2000)
2. Microwave radiometer measurements at the *Atmospheric Radiation Measurement* (ARM) *Climate Research Facility* of the US Department of Energy (Turner et al. 2003, Turner et al. 2007).
3. GRUAN radiosonde observations IWV (Immler et al 2010, Bodeker 2015)
4. AERONET version 3 level 1.5 (Holben et al 1998, Gilles et al 2019), using atmospheric transmission measurements at 0.9µm

The focus for the routine observation is on L2 *wrr NT* (Ocean Colour Product, reduced resolution, non time critical). SUOMI NET and AERONET level 1.5 are used as ground truth.

OLCI A data partly belong to reprocessed data if processed before Nov. 2017. The ocean colour products from OLCI A have been taken from EUMETSAT's rolling archive CODA (Copernicus Online Data Access) CODA (https://coda.eumetsat.int/#/home) or reprocessed OLCI A CODAREP (https://codarep.eumetsat.int/#/home) websites. All OLCI B data is from EUMETSAT's CODA.

SUOMI NET provides by far the most data with an almost near real time availability and a low uncertainty. On this account, we choose it as the principal for system monitoring. 621,000 (OLCI-A) and 306000 (OLCI-B) potential matchups within the period of June 2016 (OLCI-A) January 2019 (OLCI-B) to May 2022 have been analysed yet. The global service of SUOMI-NET has been reduced at the end of 2018, thus OLCI-B colocations are rare outside North America. Only OLCI measurements are taken for the validation which are above land and are cloud-free in an area of about 10x10 km^2 around the GNSS stations. For the cloud detection, the standard L2 cloud-mask has been applied (including the cloud ambiguous and cloud margin flags). The comparison of OLCI and GNSS shows a very high agreement (Figure 89). The correlation between both quantities is 0.97-0.98. The root-mean-squared-difference is 1.9 -2.1 kg/m^2. The systematic overestimation by OLCI is 11%-12%. The bias corrected *rmsd* is around 1.3 kg/m^2. The spatial distribution of AERONET data covers the globe better than SUOMI NET, thus we choose it as an additional measure, ignoring the fact that AERONET water vapour retrievals show a dry bias (Perez-Ramirez et al 2014). The temporal evolution of several quality measures (Figure 90 compared to SUOMI NET, Figure 91 compared to AERONET), indicates small seasonal variations, which are certainly related to retrieval assumptions. Apart from these features, neither systematic temporal changes nor differences between OLCI A and B have been observed
Similar investigations have been performed for water surfaces using AERONET–OC data as reference. As mentioned before, the quality over ocean is much worse, but neither a temporal evolution nor an instrumental difference is perceivable (Figure 92).

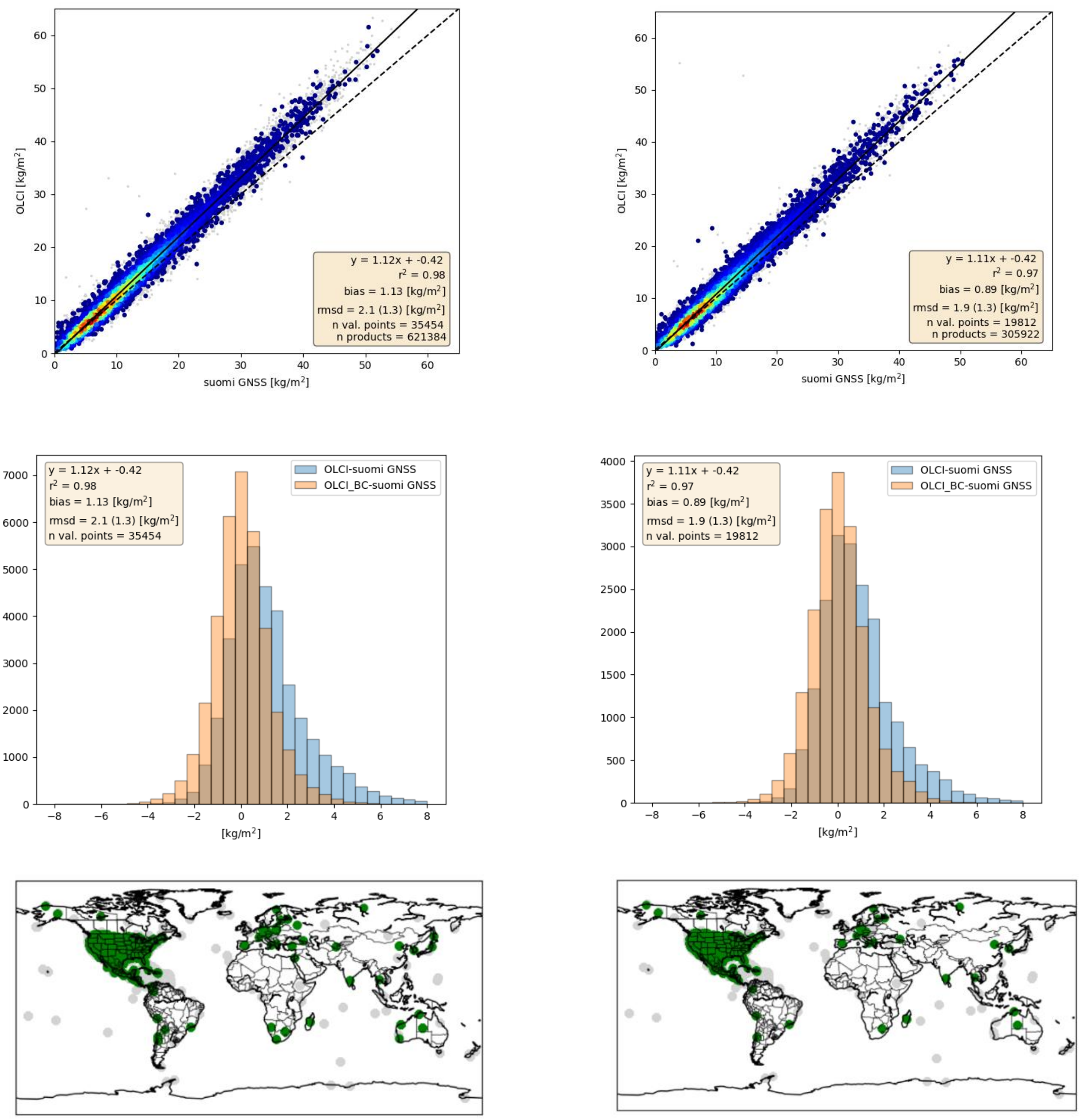

Figure 89: Upper: Scatter plot of the IWV products, derived from OLCI (A left, B right) above land and from SUOMI NET GNSS measurements. Middle: Histogram of the difference between OLCI (A: left, B: right) and GNSS (blue: original OLCI, orange: bias corrected OLCI). Lower: Positions of the GNSS (A: left, B: right).

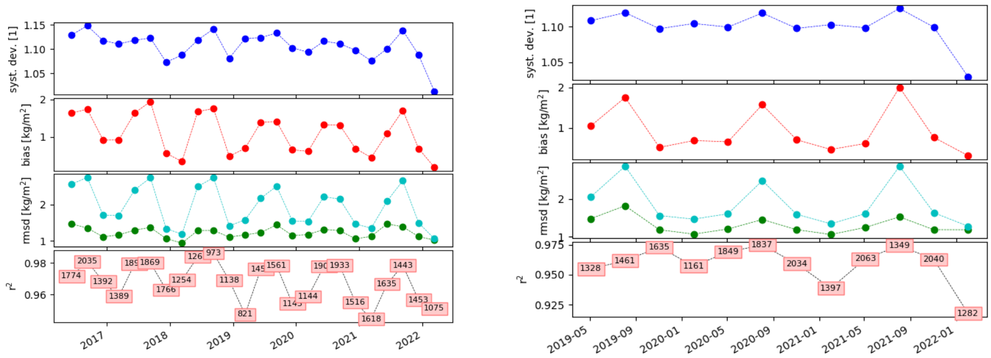

Figure 90: Temporal evolution of different quality measures for OLCI A (left) and OLCI B (right) with respect to SUOMI Net. From top to bottom: systematic deviation factor, bias, root mean squared difference (with and without bias correction), explained variance (number in boxes are the numbers of matchups)

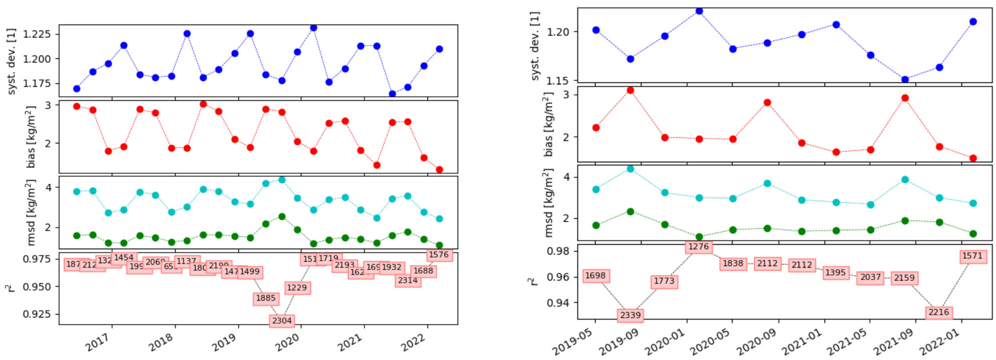

Figure 91: As Figure 90 but with respect to Aeronet version 3 level 1.5

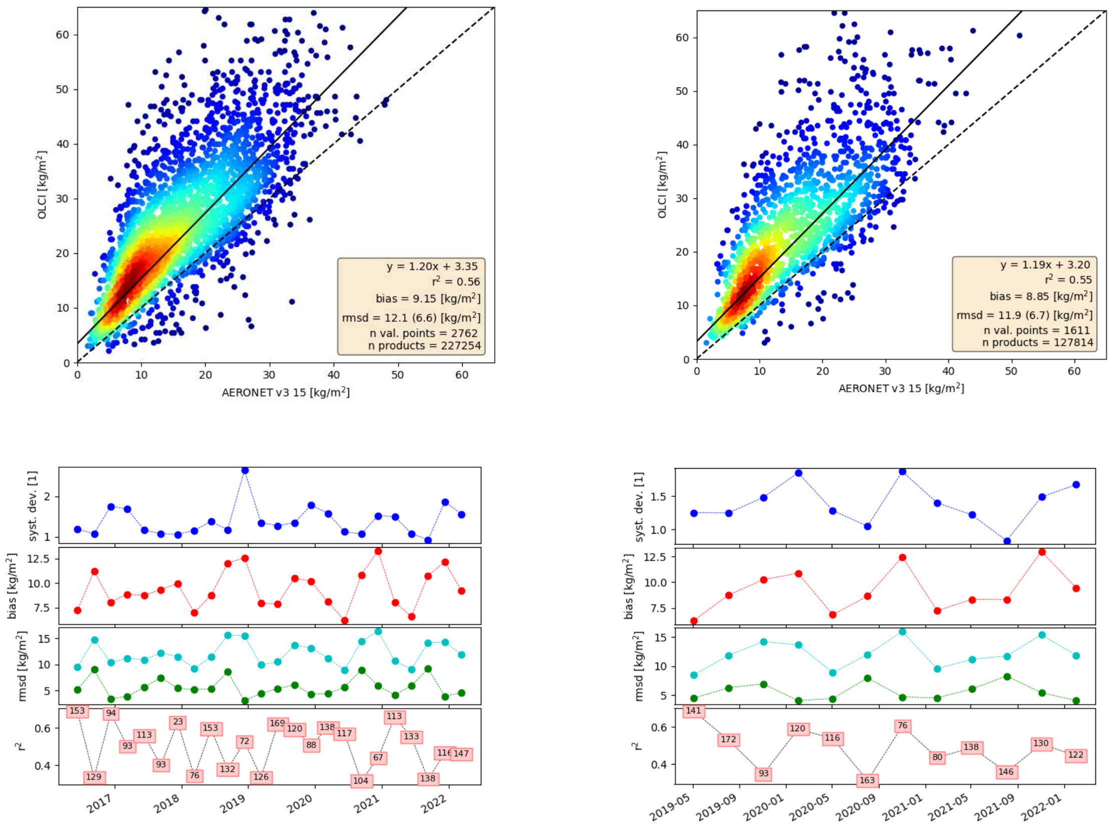

Figure 92: Upper: Scatter plot of the IWV products, derived from OLCI (A left, B right) above sea against AERONET-OC measurements. Lower: Temporal evolution of different quality measures for OLCI A (left) and OLCI B (right) with respect to AERONET-OC. From top to bottom: systematic deviation factor, bias, root mean squared difference (with and without bias correction), explained variance (number in boxes are the numbers of matchups).

6 Level 2 SYN products validation

6.1 SYN L2 SDR products

There has been no new result during the reporting period. Most recent performance figures can be found in the S3MPC OPT Annual Performance Report - Year 2021 (S3MPC.ACR.APR.009, issue 1.0, 08/12/2021), available on-line at:

https://sentinels.copernicus.eu/web/sentinel/user-guides/sentinel-3-olci/document-library.

6.2 SY_2_VGP, SY_2_VG1 and SY_2_V10 products

There has been no new result during the reporting period. Most recent performance figures can be found in the S3MPC OPT Annual Performance Report - Year 2021 (S3MPC.ACR.APR.009, issue 1.0, 08/12/2021), available on-line at:

https://sentinels.copernicus.eu/web/sentinel/user-guides/sentinel-3-olci/document-library.

6.3 SYN L2 AOD NTC products

6.3.1 Extension of 2-years validation period (2020.01-2021.12) with three months (2022.01-2022.03)

Two full years validation period (2020.01-2021.12, 24 months) has been extended with three months (January-March 2022).

Validation results for S3A $syAOD_{550}$ for 24- and 27-months periods with AERONET AOD ($aAOD_{550}$) are shown in Figure 93 as scatter density plots; evaluation statistics (offset and slope from the linear fit, N – number of matchups, r – correlation coefficient, σ- standard deviation, rms – root mean square error, EE – number of pixels in the MODIS error envelope defined as $\pm0.05\pm0.2$*aAOD, GCOS – fraction of matchups which satisfy GCOS requirements of 0.03 or 10% of AOD) are provided.

As it is seen from the validation statistics*, **extension of the two years validation period with three months*** (Jan-Mar, winter in the NH) ***has not changed validation results.*** This allows to make two statements: (i) two years period is sufficient for obtaining stable validation results and (ii) drift of the instrument is not happening.

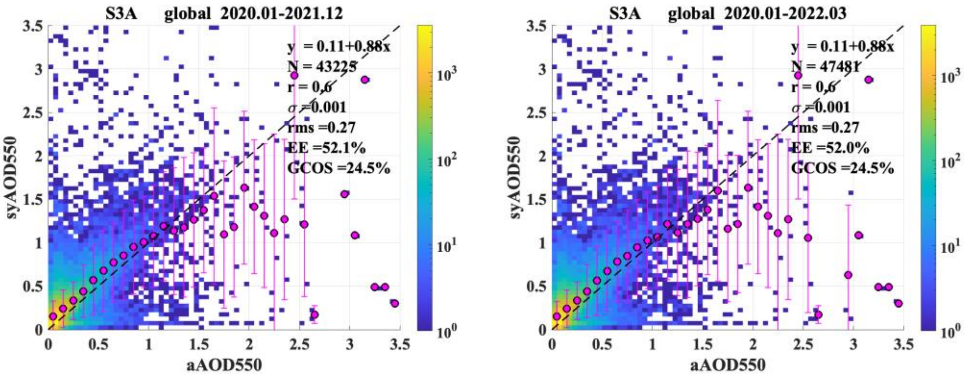

Figure 93: For S3A, Scatter density plot for syAOD$_{550}$ validation with AERONET AOD (aAOD550) for two periods: 2020.01-2021.12 (left) and 2020.01-2022.03 (right). Note that density (number of matchups per bin) is shown in logarithmic scale. Validation statistics are provided (offset and slope from the linear fit, N – number of matchups, r – correlation coefficient, σ- standard deviation, rms – root mean square error, EE – number of pixels in the MODFIS error envelope defined as ±0.05±0.2*AOD, GCOS – fraction of matchups which satisfy GCOS requirements of 0.03 or 10% of AOD).

To study further the statement on possible drift, we inter-compared validation results for three periods, which cover the same months (January-March) from three consecutive years, 2020-2022. Note, that since Sy_2 AOD product is available staring from the 14th of January 2020, validation period for Jan-Mar 2021 and 2022 was shortened to be the same as for year 2020. The results for three periods are shown in Figure 94. Though, validation results for Jan-Mar are slightly different, no clear tendency was revealed on improving or worsening of the validation statistics. Ca. 10% less matchups were provided for 2020. For this year, slope for linear regression is best (0.99/0.78/0.92 for years 2020/2021/2022, respectively), r is highest (0.66/0.60/0.61), while fraction of matchups in EE (49.7/51.2/50.5, %) and fraction of matchups which satisfy GCOS requirements (22.9/25.3/24.2, %) are lowest.

For S3B (Figure 95), ***validation statistics are slightly better for all three periods***.

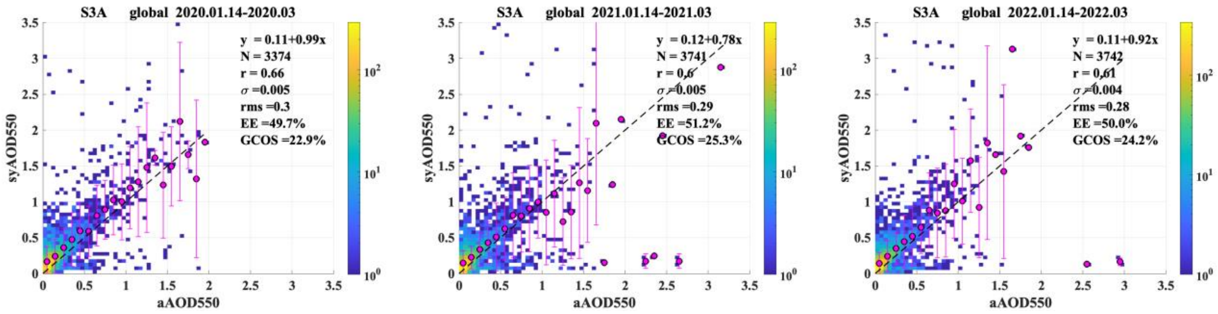

Figure 94: As in Figure 93, for S3A, scatter density plots for the same months (January-March) for three consecutive years, 2022-2022.

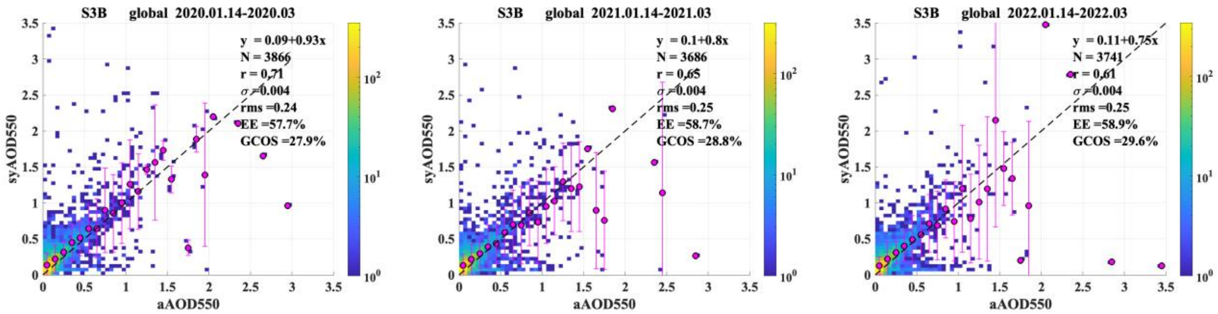

Figure 95: As Figure 94, for S3B.

As it is seen in Figure 93 -Figure 95, several syAOD outliers (both positive, syAOD>>aAOD, and negative, syAOD<<aAOD) may be reasons for worsening of the validation statistics. To reveal the conditions (type of the underlying surface, expected prevailing aerosol type), in which syAOD outliers are observed more frequently, the analysis of the outliers was performed based on their spatial location.

As in the LAW validation report, syAOD outliers have been characterized by applying three different criteria:

- Criteria1: |syAOD-aAOD|>1.5
- Criteria2: syAOD is outside MODIS EE of ±0.05±0.2*aAOD
- Criteria3: syAOD is outside EE of ±0.5±0.2*aAOD

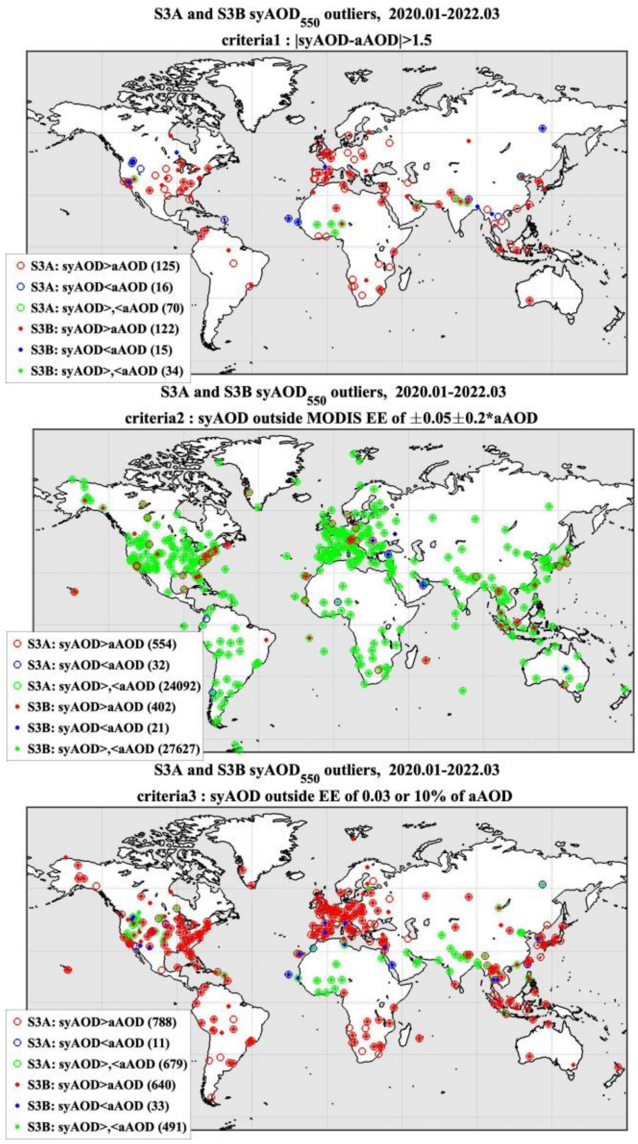

Figure 96: For AERONET stations, presence of syAOD outliers specified with different criteria (in title for each sub-figure): red for only positive, blue for only negative, green for both positive and negative outliers. For both S3A and S3B, global number of outliers is shown in the legend for each criterion.

In Figure 96 we show for each AERONET station the presence of syAOD outliers specified with different criteria. For criteria 1, which recognise outliers with the absolute difference between syAOD and aAOD above 1.5, stations with only positive outliers are located all around the globe; AOD in the West America and in dust outbreak over the Atlantic Ocean is often underestimated. AOD south from Sahara and in Tibet is both under- and over-estimated. For criteria 2, number of stations where matchups are on both sides (positive and negative) of MODIS EE is very high (more than half of the total number of matchups).

For criteria 3, the spatial distribution of positive and negative outliers is similar to criteria 1. However, this criterion, which is based on the GCOS requirements, is more strict and the number of the outlier specified with this criteria is higher.

For criteria 3, we show in Figure 97 the fraction of the outliers per AERONET station (if fraction is above 0.1). The fraction of the outliers is high over the regions mentioned above – Africa, Asia, as well as in Indonesia.

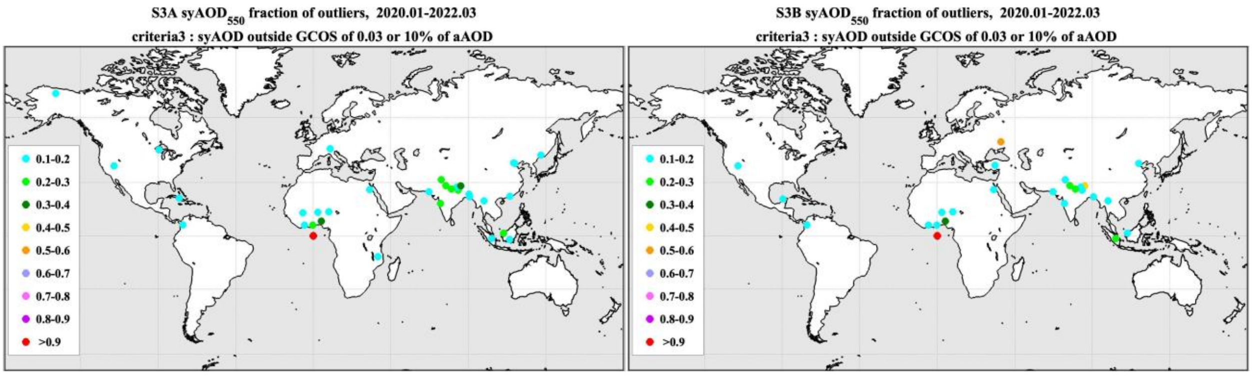

Figure 97: For S3A (left) and S3B (right), fraction of the syAOD outliers from the total number of matchups.

7 Events

For OLCI-A, two Radiometric Calibration sequences have been acquired during the reported period:

- S01 sequence (diffuser 1) on 11/05/2022 23:45 to 23:47 (absolute orbit 32457)
- S01 sequence (diffuser 1) on 27/05/2022 03:17 to 03:19 (absolute orbit 32673)

For OLCI-B, two Radiometric Calibration sequences have been acquired during the reported period:

- S01 sequence (diffuser 1) on 11/05/2022 04:35 to 04:37 (absolute orbit 21052)
- S01 sequence (diffuser 1) on 25/05/2022 06:52 to 06:54 (absolute orbit 21253)

8 Appendix A

Other reports related to the Optical mission are:

- S2 L1C MSI Data Quality Report, May 2022 (ref. OMPC.CS.DQR.001.02-2022 - i75r0)
- S2 L2A MSI Data Quality Report, May 2022 (ref. OMPC.CS.DQR.002.02-2022 - i49r0)
- Data Quality Report – Sentinel-3 SLSTR, May 2022, (ref. OMPC.RAL.DQR.04.05-2022)

All Data Quality Reports, as well as past years Cyclic Performance Reports and Annual Reports, are available on dedicated pages in Sentinel Online website, at:

- https://sentinel.esa.int/web/sentinel/technical-guides/sentinel-3-olci/data-quality-reports
- https://sentinels.copernicus.eu/web/sentinel/technical-guides/sentinel-3-slstr/data-quality-reports
- OPT Annual Performance Report Year 2021 (PDF document)

End of document